Fabrication Optimisation and Applications of PSQ-Ls Polymer Photonic Devices

Fabricatie-optimalisatie en toepassingen van fotonische PSQ-Ls polymeer componenten

Linghua Wang

Promotor: Prof. dr. ir. Geert Morthier and Prof. dr. Mingshan Zhao
Proefschrift ingediend tot het behalen van de graad van
Doctor in de Ingenieurswetenschappen: Fotonica
Vakgroep Informatietechnologie
Voorzitter: Prof. dr. ir. Rik Van de Walle
Faculteit Ingenieurswetenschappen en Architectuur
Academiejaar 2011 – 2012

UNIVERSITEIT GENT

Promoters:

Prof. dr. ir. Geert Morthier	Universiteit Gent, INTEC
Prof. dr. Mingshan Zhao	Dalian University of Technology, School of Physics and Optoelectronic Engineering

Examiners:

Prof. dr. ir. Geert Morthier (Promotor)	Universiteit Gent, INTEC
Prof. dr. Mingshan Zhao (Promotor)	Dalian University of Technology, School of Physics and Optoelectronic Engineering
Prof. dr. ir. Peter Bienstman	Universiteit Gent, INTEC
Dr. ir. Katarzyna Komorowska	Universiteit Gent, INTEC
Prof. dr. ir. Rik Van de Walle	Universiteit Gent, INTEC
Prof. dr. ir. Jan Vanfleteren	Universiteit Gent, ELIS
Prof. dr. ir. Heidi Ottevaere	Vrije Universiteit Brussel, Dept.TOMA

Universiteit Gent
Faculty of Engineering
Department of Information Technology (INTEC)
Sint Pietersnieuwstraat 41
B-9000 Gent
Belgium
Tel: +32-9-264 33 18
Fax: +32-9-264 35 93

Contents

Acknowledgement

Ghent, June 2012
Linghua Wang

Samenvatting

Het grote potentieel van fotonische integratie wordt alsmaar meer erkend door wetenschappers en ingenieurs. Er wordt verwacht dat de kleine chips die zowel fotonische, electronische als fluidische functies integreren een belangrijke rol zullen spelen in optische communicatie en optische biosensoren en dat dit een grote impact zal hebben op het dagelijkse leven. Tot dusver werd fotonische integratie uitgevoerd op verschillende materiaalplatformen. Onder andere het polymeerplatform kreeg veel belangstelling omwille van enkele unieke eigenschappen zoals de lage kost van het materiaal en de gemakkelijke processing. Deze thesis is gewijd aan de ontwikkeling van een ideaal en goedkoop polymeerplatform waarop verschillende geintegreerde fotonische componenten met hoge performantie snel en efficiënt kunnen gefabriceerd worden. In een volgende stap worden dan verschillende toepassingen in optische communicatie en optische sensing onderzocht voor de componenten van dit platform. In wat volgt vatten we ons werk kort samen.

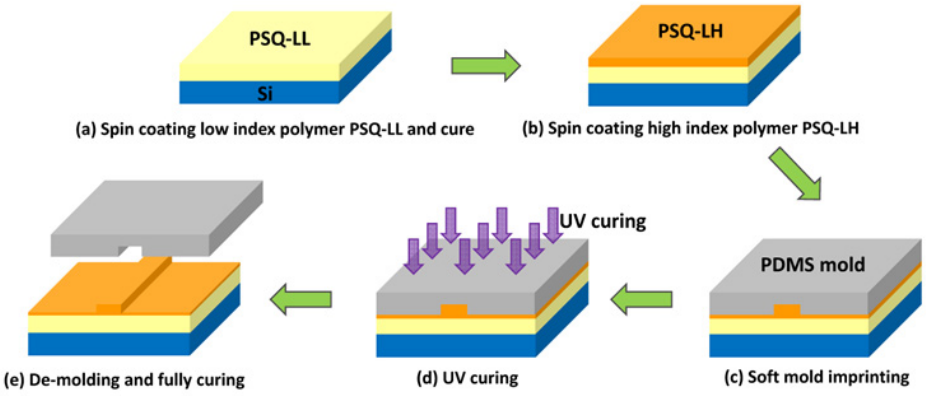

Fig. 1 Het UV-gebaseerde soft imprint proces voor de fabricatie van PSQ-Ls polymeer golfgeleiders en componenten.

Als basis voor het werk wordt een innovatieve polysiloxaan polymeer, PSQ-Ls, geintroduceerd. Een groot voordeel van deze polymeer is de gemakkelijke synthese waardoor geen toevlucht dient genomen te worden tot

dure commerciële producten, terwijl toch de gewenste materiaaleigenschappen bekomen worden. Het ontwikkelde materiaal vertoont goede optische eigenschappen (lage verliezen, lage dubbelbreking, een hoge thermo-optische coefficient enz.) en thermische stabiliteit (bv. hoge degradatietemperatuur). Unieke eigenschappen van het materiaal zijn dat hard wordt onder UV-belichting en solvent-vrij. Deze materiaaleigenschappen maken van de PSQ-Ls polymeren goede kandidaten voor de fabricatie van golfgeleiders en golfgeleidergebaseerde circuiten.

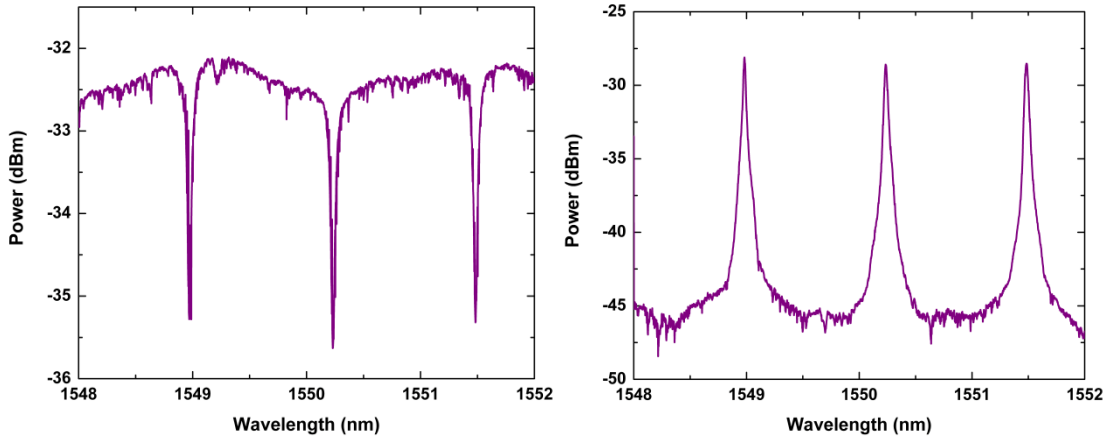

(a) (b)

Fig. 2 Transmissiespectrum van een gefabriceerde polymeer microring resonator voor de TE mode. (a) Through poort. (b) Drop poort.

We exploreren diverse fabricatieprocessen, op zoek naar een geschikte manier om de ontwikkelde PSQ-Ls polymeren te processen tot golfgeleiders en andere fotonische componenten. Conventionele lithografie en droogetsen zijn experimenteel mogelijk, maar worden als te complexe processen beschouwd. Daarom wordt een eenvoudige UV-gebaseerde soft imprint techniek, getoond in Fig. 1, ontwikkeld die compatibel is met de PSQ-Ls polymeer. Kritische aspecten zoals golfgeleiderruwheid en de dikte van de residuele laag worden aangepakt en in detail besproken. Diverse polymeer-gebaseerde optische componenten, zoals rechte golfgeleiders, splitters, microring notch filters, racebaan microring resonatoren en MZI-gebaseerde afstembare ring resonatoren, werden gefabriceerd. De bekomen

componenten vertonen goede optische eigenschappen zoals ze gewenst zijn voor onze toepassingen, bv. de lage verliezen van de golfgeleiders, de hoge extinctieverhouding van het notch filter, de hoge Q waarde van de microring resonator enz.. Een typisch transmissiespectrum van de microring resonator voor de TE mode is te zien in Fig. 2.

De gefabriceerde polymeer fotonische componenten worden in diverse toepassingen gebruikt. Optische single sideband (OSSB) filtering wordt gerealiseerd door het gebruik van een microring notch filter met hoge extinctieverhouding als een smalbandig microgolf-fotonisch filter. Op die manier kan het door de chromatische dispersie veroorzaakte fading effect effectief onderdrukt worden, hetgeen toelaat om een door een microgolf gemoduleerd optisch signaal over een lange vezellink te versturen en met hoge kwaliteit te ontvangen.

Optische label-vrije biosensing wordt gerealizeerd met behulp van een polymeer microring resonator met hoge Q waarde. We bespreken de sensing mechanismen, de bevragingsmethodes en de ontwerpbeschouwingen voor dit soort component. Speciale aandacht werd gewijd aan de performantie van de microring resonator in een waterige omgeving. Een eenvoudig maar efficient oppervlaktefunctionalisatieprotocol werd ontwikkeld voor de polymeer microring resonator. Protein A molecules worden geimmobiliseerd op het oppervlak van de polymer microring resonator, en deze kunnen later gebruikt worden om het affiniteitspaar, menselijk IgG te detecteren. Zowel bulk sensing als oppervlakte sensing kunnen gerealiseerd worden dankzij het fluidisch kanaal dat op de chip is geassembleerd d.m.v. de “stamp-and-stick” methode. Voor bulk sensing wordt met een NaCl oplossing een gevoeligheid bekomen van rond de 50 nm/RIU. Voor oppervlakte sensing wordt een verschuiving van de resonantiegolflengte geobserveerd van 230 pm na de binding van de doelanalyten en de eerder geimmobiliseerde bioreceptors. In dit werk worden de voordelen van het polymeermateriaal zelf, van de ontwikkelde imprint technologie en van het oppervlaktefunctionalisatieprotocol gecombineerd teneinde een goedkope, wegwerpbare polymeer label-vrije biosensor te ontwikkelen.

We onderzoeken ook een nieuwe methode voor de koppeling tussen polymeergolfgeleiders en optische vezels, nl. oppervlaktekoppeling. Alhoewel silicium oppervlakteroosterkoppelaars in de voorbije jaren intensief bestudeerd werden, werd dit slechts in beperkte mate onderzocht voor polymeren. De belangrijkste uitdaging komt van het lage brekingsindexcontrast bij polymeer-golfgeleiders. Om dit probleem te omzeilen stellen we een structuur voor in dewelke een dunne laag Si_3N_4 met hoge brekingsindex ingebed is tussen de golfgeleiderkern en de ondercladding. Aldus is voor het eerst een koppeling tussen polymeergolfgeleider en monomode vezel gedemonstreerd van 12%. In vergelijking met de gebruikelijke butt-koppeling is de koppeling met oppervlakteroosters veel flexibeler en is de alignatietolerantie veel relaxter. Dit is van groot nut voor de verdere ontwikkeling van een gemultiplexeerd biosensing systeem met polymeer-gebaseerde fotonische componenten.

Tenslotte wordt het temperatuursprobleem beschouwd en besproken. Speciale aandacht wordt besteed aan de athermalisatie van een van de meest belangrijke WDM componenten in silicium, de ‘arrayed waveguide grating (AWG)’. Gebruikmakend van een goed ontwerp, een state-of-the-art CMOS fabricatietechniek en een hoge thermo-optische coefficient van de PSQ-Ls polymeer werd de temperatuursafhankelijkheid van de silicium AWG gereduceerd tot -1.5 pm/˚C, terwijl daarbij een goede filterwerking van de component werd behouden. Tot dusver hebben we athermalisatie gerealiseerd van verschillende sleutelcomponenten in silicium, o.a. Mach-Zehnder interferometers, microring resonatoren en AWGs. Deze optische componenten zullen een belangrijke rol spelen in toekomstige elektronisch-fotonisch geïntegreerde systemen. Verder werd ook een athermische polymeer structuur voorgesteld voor een biosensor op basis van een microring resonator. Een dergelijke structuur zou de temperatuurs-geinduceerde ruis tijdens biosensing essentieel kunnen elimineren.

Summary

The great potential of photonic integration has been recognized more and more by scientists and engineers. The small chips that integrate photonic, electronic and possible fluidic functions are expected to play an important role in optical communication and optical biosensing, which will have a deep impact on the life of people. So far, photonic integration is performed on several material platforms. As one of them, polymer receives much attention due to some of its unique features such as low cost and easy processing. This thesis is dedicated to the development of an ideal platform, on which different kinds of integrated photonic devices with high performance can be fabricated in a fast and efficient way with the cheap polymer material. As a further step, several applications in optical communication and optical sensing are found for the devices obtained from this platform. In the following, we briefly summarize our work.

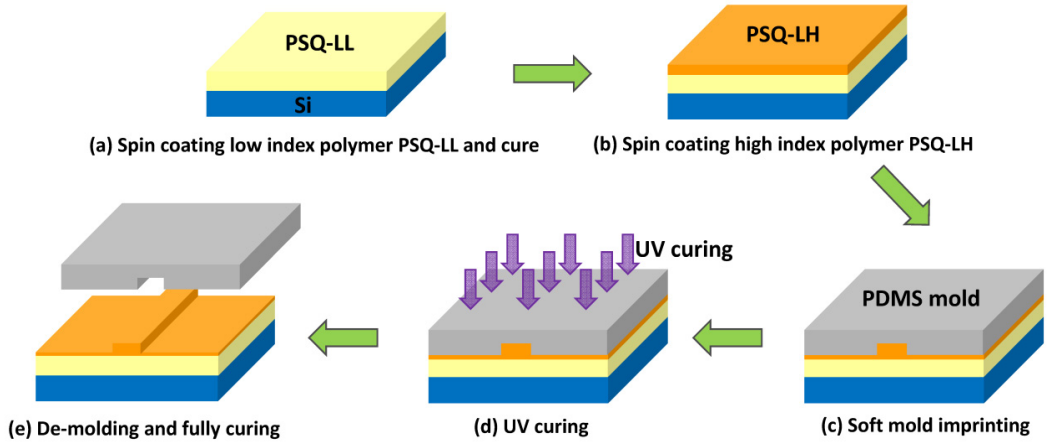

Fig. 1 The UV-based soft imprint process for the fabrication of PSQ-Ls polymer waveguide and devices.

As the foundation for the work, an innovative polysiloxane polymer material named PSQ-Ls is introduced. Easy synthesis is a big advantage for the polymer, for which we don't need to resort to expensive commercial products and can still obtain the desired material properties. The self-developed material exhibits good optical properties (e.g. low optical loss, low

birefringence, high thermo-optical coefficient and so on) and thermal stability (e.g. high degradation temperature). Being UV curable and solvent-free are unique features for this material. These material characteristics enable polymer PSQ-Ls to be a good candidate for the further fabrication of polymer waveguides and devices.

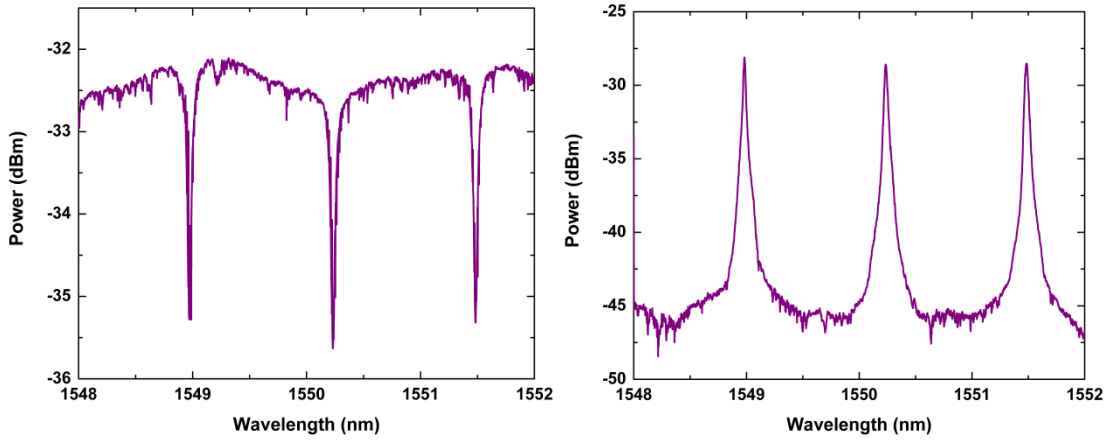

(a) (b)

Fig. 2 Transmission spectrum of the fabricated polymer microring resonator working with TE mode. (a) Through port. (b) Drop port.

We explore different fabrication processes, trying to find an appropriate way to process the developed polymer PSQ-Ls into waveguides and devices. Conventional lithography and dry etching method is experimentally feasible, but is considered to be unsuitable because of the complicated fabrication process. Thus a simple UV-based soft imprint technique compatible with polymer PSQ-Ls is developed, which is shown in Fig. 1. Critical issues such as waveguide roughness and residual layer thickness are solved and discussed in detail. Different kinds of polymer-based optical devices, which include straight waveguides, splitters, microring notch filters, racetrack microring resonators and MZI-based tunable ring resonators, were fabricated in this fast and efficient way. The obtained devices exhibit good optical performances, which are highly desired for our subsequent applications, for example, the low loss of the optical waveguide, the high extinction ratio of the notch filter, the high Q value of the microring resonator, and so on. One typical

transmission spectrum of the microring resonator working with TE mode is shown in Fig. 2

The fabricated polymer photonic devices are used in several applications. Optical single sideband (OSSB) filtering response is realized by using the microring notch filter with high extinction ratio as a narrowband microwave photonic filter. By this, the chromatic dispersion induced fading effect is suppressed effectively, which allows the microwave modulated optical signal to be transmitted over a long distance fiber link while the microwave signal can still be received with high quality.

Optical label-free biosensing is realized with the polymer microring resonator with high Q value. We discuss the sensing mechanisms, the interrogation methods and the design considerations for this kind of device. Special attention was paid to the performance of the microring resonator working in aqueous environment. A simple but efficient surface functionalization protocol is developed for the polymer microring resonator. Protein A molecules are immobilized onto the surfaces of the polymer microring resonator, which later can be used to detect its affinity pair, human-IgG. Both bulk sensing and surface sensing are realized with the solution delivering capability provided by the fluidic channel, which is assembled on the chip of polymer microring resonators with the “stamp-and-stick” method. For bulk sensing, a sensitivity of around 50 nm/RIU is achieved with a NaCl solution. For surface sensing, a resonant wavelength shift of 230 pm is observed when the binding of the targeted analytes and the bioreceptors we immobilized previously happened on the surface of the polymer microring resonator. Within this work, the advantages of the polymer material itself, the developed imprint technology and the surface functionalization protocol are combined together to develop a low-cost, disposable polymer label-free biosensor.

We investigate a new coupling mechanism for polymer waveguides, surface coupling. Although silicon surface grating couplers with different kinds of structures have been intensively studied in the past few years, very limited

works were carried out on polymer. The main challenge comes from the low refractive index contrast of the polymer waveguide. In order to circumvent this problem, we proposed a structure, in which a thin layer of Si_3N_4 with high refractive index is embedded between the waveguide core and the under cladding. By doing this, the coupling between the polymer waveguide and the single-mode fiber is demonstrated for the first time, with a coupling efficiency of around 12%. Compared to the edge coupling route usually adopted for the polymer waveguide, the surface coupling regime is more flexible with relaxed alignment tolerance, which would be of great use for the further development of a multiplexed biosensing system with polymer-based photonic devices.

Finally, the temperature problem is considered and discussed. Special attention is paid to realize the athermalization for one of the most important WDM components, the arrayed waveguide grating (AWG). Taking advantage of a proper design, a state-of-the-art CMOS fabrication technique and a high thermo-optical coefficient of the PSQ-Ls polymer, the temperature dependence of the AWG is reduced to only -1.5 pm/˚C, while maintaining the good filtering property of the device. So far, we have realized athermalization for several key optical components, which include MZI, microring resonator and AWG. These optical components will play an important role in future high-level electrical-photonic integration systems. Besides that, an all-polymer structure is proposed for the biosensor with a ring resonator structure, which, if realized, can essentially remove the temperature induced noise during the biosensing measurement.

List of Acronyms

AWG	Arrayed waveguide grating
BCB	Benzocyclobutene
BSA	Bovine serum albumin
CCD	Charge-coupled device
CMOS	Complementary Metal Oxide Semiconductor
DI water	Deionized water
EDFA	Erbium-doped fiber amplifier
ELISA	Enzyme-linked immunosorbent assay
EOMs	Electro-optical modulators
EVM	Error vector magnitude
FDTD	Finite-difference-time-domain
FFT	Fast Fourier transform
FIB	Focused Ion Beam
FITC	Fluorescein isothiocyanate
FSR	Free Spectral Range
FWHM	Full Bandwidth at Half-Maximum
HF	Hydrofluoric acid
ICP	Inductively Coupled Plasmas
IgG	Immunoglobulin G
LOC	Lab-on-a-chip
MMF	Multimode fiber
MPFs	Microwave photonic filters
MZI	Mach-Zehnder interferometers
NIL	Nanoimprint lithography
ODSB	Optical double sideband
OSA	Optical spectrum analyzer
OSSB	Optical single sideband
PA	Protein A
PBS	Phosphate Buffer Solution
PC	Polycarbonate
PCB	Printed Circuits Board
PDMS	Polydimehysiloxane

PDs	Photo detectors
PECVD	Plasma-enhanced chemical vapor deposition
PML	Perfect matched layer
PMMA	Poly(methylmethacrylate)
PS	Polystyrene
QPSK	Quadrature phase shift keying
RF	Radio-frequency
RIE	Reactive Iron Etching
RoF	Radio over Fiber
SEM	Scanning electron microscope
SLED	Super-luminescent light-emitting diode
SMF	Single-mode fiber
SNR	Signal to noise ratio
SOI	Silicon on insulator
SPR	Surface plasmon resonance
TE	Transverse Electric
TEC	Thermal expansion coefficient
TGA	Thermo-Gravimetric Analysis
TM	Transverse Megetic
TOC	Thermo-optical coefficient
UV	Ultra-Violet
WDM	Wavelength division multiplexing

Chapter 1 Introduction

1.1 Polymer-based photonic integration

In recent years, the great potential of photonic integration in the fields of optical communication and optical sensing has been widely recognized. It is expected that the efforts made on integration can bring forward the benefits of compactness, reduced cost, improved performance, increased yields, etc [1-5]. In order to realize different functions such as multiplexing or de-multiplexing, routing, interleaving, attenuating, photo detecting or even lasing, a variety of passive or active components are needed. Typical passive components in integrated photonics include waveguides, splitters, arrayed waveguide gratings (AWGs), gratings and microring resonators. Important active components include modulators, amplifiers, photo detectors, optical switches and so on. Such a broad range of integrated devices, each with unique requirements imposed, implies that implementing all within one material platform is not realistic. That is also the reason why currently there coexist several material platforms for photonic integration, including silica, SOI (silicon-on-insulator), silicon oxynitride, lithium niobate, indium phosphide, gallium arsenide, magneto-optic materials, birefringent crystals and polymer.

Compared with traditional inorganic optical materials, polymeric optical material and integrated devices fabricated in it have the following unique features [5-9]:

- The polymer has high tailoring freedom. Its optical and mechanical properties can be tuned with a chemical modification method to meet specific applications.
- The polymer is compatible with different kinds of substrates, e.g. silicon, glass, ceramic, PCB board and so on, which is highly desired for hybrid integration.
- The optical polymer now has reached a very low loss. As its refractive index is close to silica, the coupling loss between the fiber and polymer-based photonic devices is low.

- It is an ideal host for rare earth ion dopants to make this material have large electro-optic or amplification effect, which is attractive for the realization of all-optical network.
- The soft characteristic of the polymer implies the processing of this material is not limited to traditional semiconductor methods. Many novel fabrication methods that reduce both the cost and time can be employed.

The purpose of this thesis is to fully exploit the benefits that the polymer-based photonic integration can bring. On one hand, efforts will be paid to build an extremely low-cost polymer platform, on which the integrated photonic devices can be fabricated in a fast and efficient way with cheap polymer material. The devices' cost is thus reduced to a minimum without compromised performances. On the other hand, attempts will be given to expand the applications of these photonic chips obtained from this platform. Some particular applications include:

- Enhance the transmission quality of the RoF (Radio-over-Fiber) signal over a long distance fiber link.
- Develop a disposable label-free biosensor which can be used to detect specific diseases.
- Remove the temperature dependence of the integrated photonic devices.

1.2 **Material and fabrication**

Compared to the less diverse inorganic materials and their fabrication method, in the world of polymer, the properties of the materials can differ a lot from each other. Accordingly, several novel fabrication techniques have emerged in order to process these materials. Thus, the selection of a suitable polymer together with an adapted fabrication methodology is crucial for the purpose of acquiring devices with desired performances. In this section, a brief review will be given to see the progress made in this field.

1.2.1 Polymer materials

In the past, some conventional polymer materials are used for the fabrication of polymer devices, such as as poly(methylmethacrylate) (PMMA), polystyrene (PS), polycarbonate (PC) and so on [7]. Some other kinds of photo resists, typically SU-8 for example, are also often used. However, these polymers or photo resists either have high optical absorption in the key telecommunication windows, or they exhibit rather poor thermal stability. For example, the glass transition temperature for PMMA is only 105 ˚C. Thus, they are not actually very suitable for fabricating photonic devices, especially when high optical performances are required. The high absorption loss is mainly due to the overtones of the molecular vibrations from C-H and O-H bonds. Recently, great efforts have been paid to reduce the material loss and enhance their thermal stability. Halogenation is one of the effective ways. By partially or fully replacing the C-H bonds with C-F or C-Cl bonds, optical loss and thermal stability of the material can be dramatically improved [10, 11]. Another polymer system well established to meet the requirement is the polysiloxane class of materials, usually synthesized by the well-known Sol-Gel method. Some commercial products have passed the stringent Telcordia environmental reliability criteria [12].

1.2.2 Fabrication methods for polymer waveguides

Optimization of the processes for inorganic materials through standard semiconductor methods has already had a long history and so far it is approaching the state-of-the-art. Lots of attempts have been made, trying to implement the same protocol to the fabrication of polymer devices. However, the results prove to be less ideal. The main prohibiting reason is the vast varieties of the polymer materials and their properties. Besides that, the distinct advantage of the polymer devices over their inorganic counterparts, low cost, is sacrificed with this process. Thus it is highly desired that there are alternative innovative fabrication methods which can fully develop the potential advantages of this kind of material.

Direct photon patterning is the most simple and straightforward technique. Photonic devices can be obtained upon single exposure and development without further treatment [13, 14]. The obvious advantages of this method are the greatly reduced fabrication turnaround time and the low-cost processing equipments. The drawback of this technique is that it imposes a high requirement on the polymer material, which has to be photosensitive. The quality of the fabricated waveguides becomes also highly dependent on the properties of the polymer itself as well as exposure condition.

Direct laser writing or laser ablation were also explored to fabricate polymer waveguides in recent years [15-17]. The advantage of this method is that fast and inexpensive prototyping can be finished without using the expensive mask. Writing of structures with high resolution or un-regular shape is also possible. However, the drawback of this fabrication technology is also apparent, which is less efficient for high throughput.

Nanoimprint lithography (NIL) which was first proposed in the mid 1990s is a promising fabrication candidate combining the advantages of low cost, high resolution and high throughput [18-21]. These advantages can be attributed to the simple working principle of NIL. Since it is based on the physical contact of the mold and soft polymer material to pattern the structures, there is not diffraction limit set by the conventional lithography. So the patterned structures can have the same resolution as that on the mold. Accelerated by continued emerging new techniques, roll-to-roll for example, this fabrication method has uncomparable advantages on throughput, resulting in the decreasing cost of the devices. It is noticed that recently this technology has not been only limited as a lithography methodology on the photo resist, but also used more and more to directly fabricate photonic devices. Some state-of-art works have been carried out by the group of L. Jay Guo and the group of A. Yariv. Fig. 1.1 shows the microring resonator fabricated with NIL, with the smallest feature (the gap between channel and ring waveguides) only about 200 nm [22]. Fig. 1.2 shows a multilayer waveguide structure made by soft lithography, a variation of NIL, which is a good strategy to increase the

integration density [23]. Besides that, this technology has also been applied for biological and lab-on-chip applications.

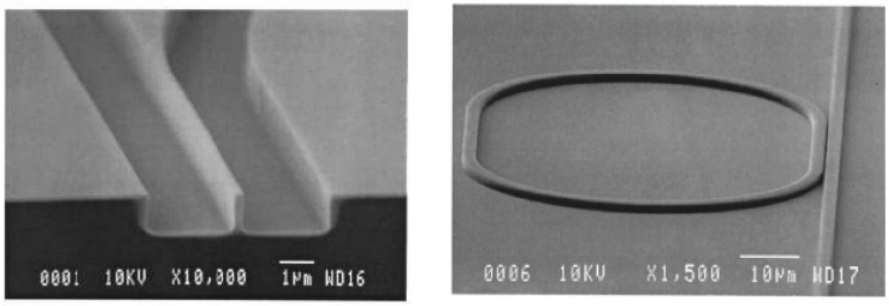

(a) (b)

Fig. 1.1 SEM images of mold and devices. (a) a typical deep SIO_2 mold used to create polymer microrings and (b) the nanoimprinted polystyrene microring.

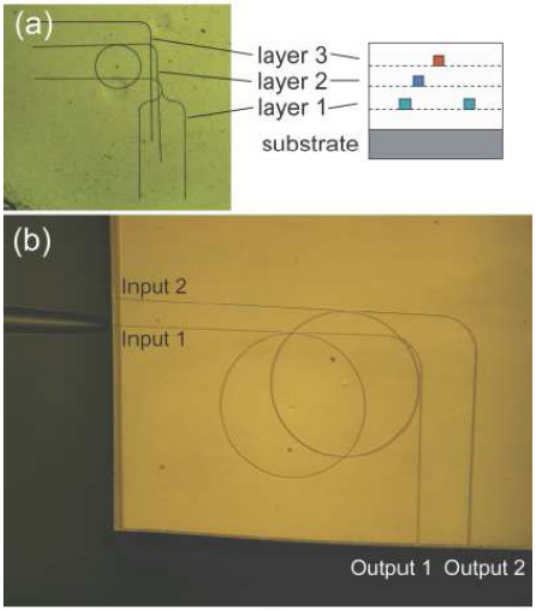

Fig. 1.2 Optical microscope images of multilayer devices. (a) A three-layer microchip and its schematic structure. (b) A two-layer microchip containing a microring resonator optical filter in each layer.

However, despite the many merits it can provide, some problems with this method cannot be neglected and need to be solved well. For example, since it is a replication technique, the quality of the fabricated device depends heavily

on that of the mold. Because of this, mold fabrication becomes extremely important, which could be a bottleneck for NIL. Traditional but mature clean room nanofabrication processing methods are still mainly used to fabricate the mold, which is time and capital cost. Moreover the physical contact property of NIL can easily result in contamination or damage of these original molds, resulting in the greatly reduced lifetime of them [24]. So it is ideal if there is a mold replication technique to make copies of the master mold. Good quality of the devices can still be guaranteed and the expensive master mold can be well protected. The second important issue is the pervasive “residual layer” problem. Although NIL can create a surface corrugation of the polymer, usually the polymer at the location where it is imprinted by the protrusions on the mold cannot completely disappear. A thin residual film would be left. In most cases, this residual layer is detrimental for the behaviour of the waveguides, especially single-mode waveguides. How to mitigate or eliminate its influence on the performance of polymer photonic devices has been studied intensively. Besides the regular means such as dry etching, increasing the imprinting forces or diluting the polymer, several un-regular routes have also been proposed. For example, A. Flores et al use a vacuum-assisted microfluidic technique to fabricated polymer waveguides, which dramatically reduces the residual layer thickness of the waveguides. This is shown in Fig. 1.3 [25]. But without doubt, these methods add complexity to the fabrication system, and the polymer devices’ cost is increasing accordingly. Resorting to dry etching can even induce extra surface roughness for the polymer waveguide. As mentioned before, not all polymers are suitable to be used as waveguide material. On one hand, they have to meet certain requirements on optical and thermal properties. On the other hand, they need to be adapted to specific fabrication methods. For some type of polymers such as PMMA, PS and so on, which don’t have UV curing characteristic, the imprinting is limited to thermal strategy, hot-embossing for example, which increases the time of fabrication. For the materials suitable for UV patterning, either the transparency of the mold or the substrate is required. Thus, a comprehensive consideration must be given to figure out a route with which

the raw polymer material can be fabricated into photonic devices by efficiently taking advantage of the characteristics of the material and NIL method. Based on these discussions, the first part of this thesis will be dedicated to build such a fabrication platform based on polymer.

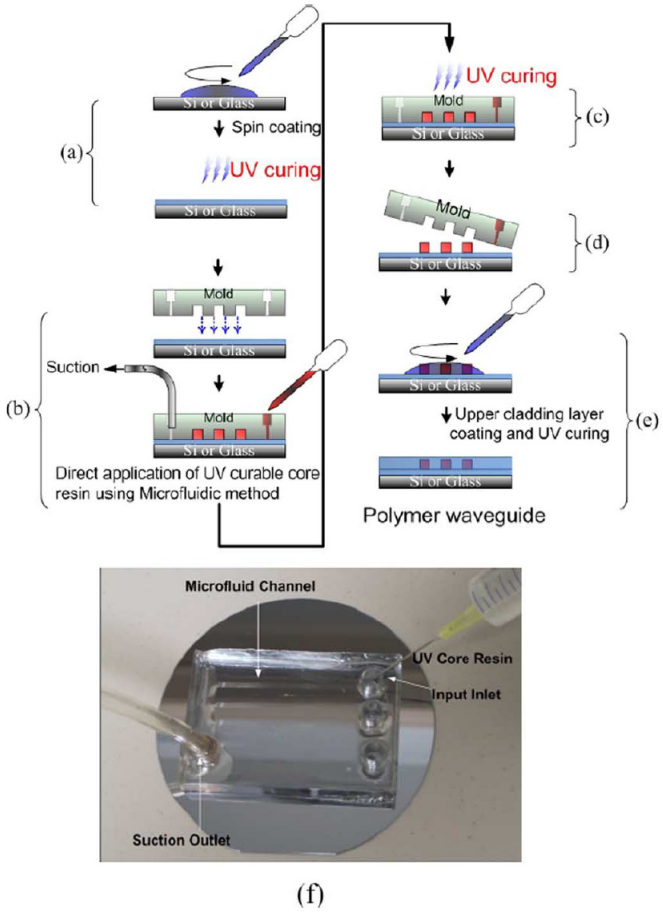

Fig. 1.3 Process flow for device replication via vacuum-assisted microfluidic technique (a) and the top view of the fabrication setup (b).

1.3 **Applications**

The second part of this thesis will be focused on the applications of the fabricated polymer-based photonic devices. In this introduction, we mainly discuss two aspects: optical sensing and athermalization.

1.3.1 Biosensing and Lab-on-a-chip

Biosensing is a technology for detecting a specific substance by converting the recognition from a biological entity (i.e. DNA, antibody, enzyme, etc.) into signals that can be further processed and related to the concentration of the substance under analysis. People show more and more interest in this technology as it can provide selective, sensitive, fast, direct and cost-effective analysis [26]. The main application fields of biosensing can be clinical diagnostics, environmental monitoring, chemical and biological warfare surveillance, food industry, veterinary and industrial process control. The further developing direction for this technology would be Lab-on-a-chip (LOC) [27, 28]. LOC are miniaturized devices which integrate several laboratory functions, which can be very diverse in nature, like cell lysis, sample amplification (e.g. PCR) and dilution, sample cleaning, fluorescent labeling, process monitoring and optical detection, onto a single chip of only millimeters to a few square centimeters in size. LOC can offer lots of merits, such as compactness, low fluid volume consumption, faster analysis and response time, better process control, massive parallelization which allows high-throughput analysis, lower fabrication cost which allows cost-effective disposable chips and so on.

Requiring an extra molecular labeling step is the drawback of traditional sensing detection techniques. While it can provide a high detection limit down to one single molecule through straightforward luminometry, fluorimetry, spectrometry, radiometry or confocal microscopy, the labeling process itself is an expensive, time and labor-consuming procedure [29]. Even worse, labeling may change the reactivity and/or specificity of the labeled biomolecules, reducing both the qualitative (detectability, specificity and selectivity) and quantitative (kinetics and thermodynamic parameters, concentration analysis) information of biological assays [30]. In contrast, the optical label-free biosensors show apparent advantages. In label-free detection, target molecules are not labeled or altered, and are detected in their natural forms. This type of detection is relatively easy and cheap to perform, and allows for quantitative and kinetic measurement of molecular interaction. A unique

feature for those sensors whose working principle is based on evanescent field detection, which is shown in Fig. 1.4, is that the detection signal does not scale down with the sample volume [29]. This characteristic is particularly attractive when an ultrasmall (femtoliter to nanoliter) detection volume is involved.

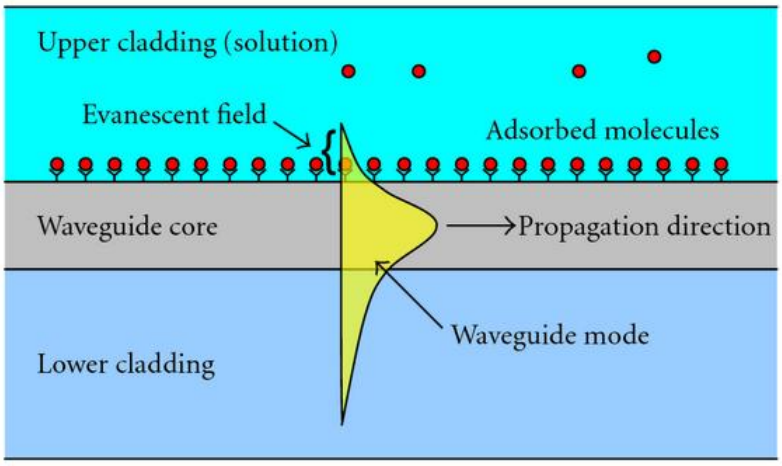

Fig. 1.4 Illustration of a waveguide evanescent field sensor [31].

As will be seen in this thesis, applying polymer-based optical integrated devices onto label-free biosensing is feasible. The cost of the polymer material itself is very low, which makes it attractive where the economic factor needs to be taken into account. The tunable properties of the polymer give the design and fabrication of the photonic devices much more flexibility. Secondly, compared to inorganic materials, biocompatiblity would be another important and unique feature of polymers. By this, the biochemical surface treatment of the polymer photonic devices has the hope to be simplified. Besides the traditional mature semiconductor processing methods, the developed nanoimprint lithography technique can be applied to fabricate the polymer-based optical devices, which offers lots of merits such as high resolution, minimal requirements for complicated equipment, simple fabrication processes involved, and a huge potential for high throughput, as mentioned before. Based on these advantages, this platform provides us an opportunity

to develop an extremely low cost thus disposable label-free optical biosensor. Besides the above practical benefits, some potential benefits can also be promising. Polymer provides an ideal platform for the realization of LOC, in which not only the optical components such as waveguides, light sources and detectors, but also the sensing elements as well as electric functions can be integrated together. Such concept is demonstrated by the group of I. H. White recently [32], which is shown in Fig. 1.5. The cheap laser diode, photodiode, dye-coated waveguide sensing elements and electrical driving and bias circuits are intergrated onto a PCB board. Similar works have also been performed in the European project “SEMOFS” [33].

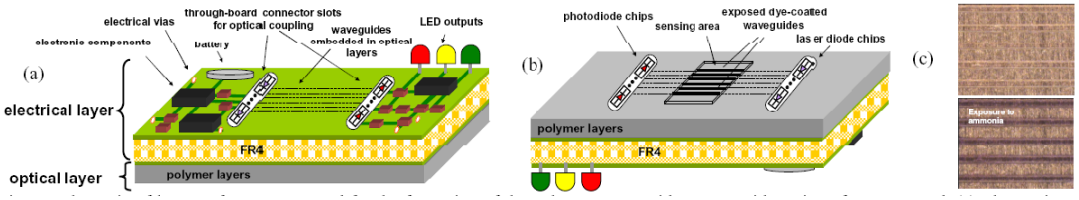

Fig. 1.5 Schematic of layout of EO PCBs used for the formation of the polymer waveguide sensor with various features noted. (a) Planar view of (a) top and (b) bottom board sides. (c) Images of exposed dye-coated (BTB) waveguides before (top) and after (bottom) NH_3 exposure.

1.3.2 Electronic-photonic integration and athermalization

In fact, one important concept has been proposed within the discussion at the end of last section, which is electronic-photonic integration. Not only limited to photonic integration, electronic and photonic components are brought together onto the same chip. The great benefits of this technology would be fast speed, improved performance, improved power efficiency, increased functionality, enhanced reliability, reduced cost and so on [34, 35]. The integration has great meaning to the LOC, as it would enable an ideal smart, multifunctional LOC platfrom that are battery powered and portable, which has been discussed before. Besides that, the other important application of electronic-photonic integration technology is different kinds of optical interconnects. Optical interconnect has been considered to be a good solution to overcome

the bottlenecks set by the electrical interconnect, such as data transmission speed, packaging size of electronic circuits, and power dissipation. From the views of the material and manufacturability, so far silicon and polymer waveguides are two ideal platform candidates for the realization of optical interconnects. For the former, CMOS compatibility and extremely high integration density are its obvious advantages. While for the later, besides the low cost, a variety of fabrication processes can be utilized, such as diamond blade cutting, soft-lithography, laser ablation and so on [36, 37]. Especially, recent developments on the integration of polymer waveguides onto standard printed circuit boards (PCBs) for use in board-level communications have demonstrated the potential of cost-effectively producing electro-optic (EO) PCBs with conventional methods of PCB manufacturing, which is rather attractive for both optical interconnect and LOC. One example of a fully embedded optical interconnect architecture is show in Fig. 1.6.

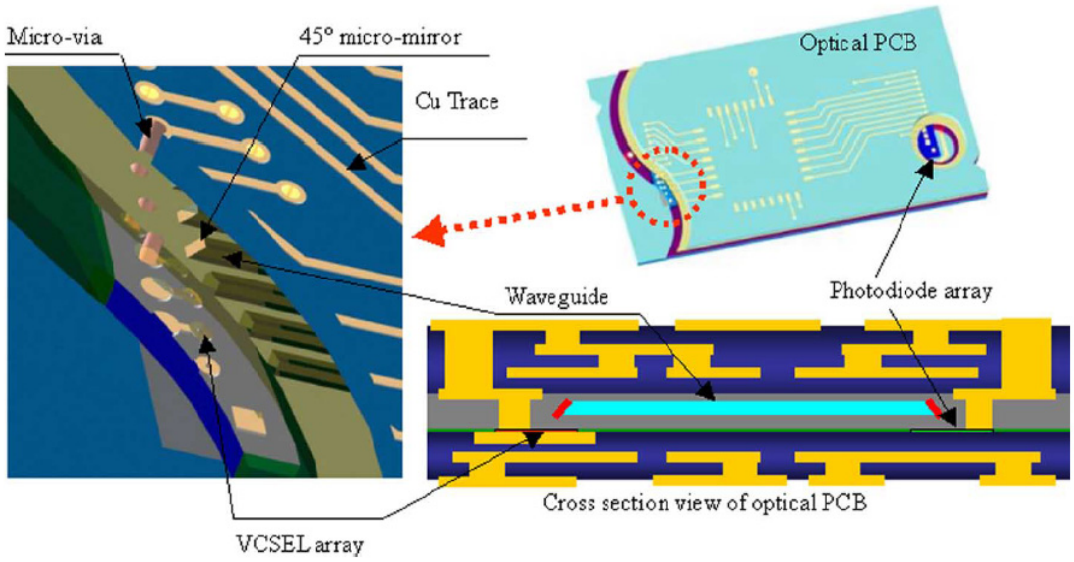

Fig. 1.6 Illustration of the fully embedded optical interconnect architecture [37].

Besides the material and manufacturability issues, however, temperature stability can be a big obstacle that hinders the further development of LOC and electronic-photonic integration. For on-chip electronic-photonic integration, the running electronic components will create significant local or

global temperature rise. Such temperature rise will put the on-chip photonic components at a high risk of unstable performance because of the high thermo-optical (TO) coefficient of the used material, either silicon or polymer [38-40]. It is especially worse if such components are in the structure of cavity such as microring resonator. Although these resonant devices are ideally suited for dense integration of optical networks due to their compact size, high extinction ratio per unit length, low insertion loss and low power consumption, the large temperature induced resonant wavelength shifts will severely limit the wavelength resolution in applications such as wavelength division multiplexing (WDM) and high-resolution spectroscopy. This challenge is faced also by different kinds of optical biosensing systems nowadays, either commercial ones or laboratory-built ones. On one hand, there is a strong desire to enhance the sensitivity of the biosensors, on which a lot of efforts are cost. On the other hand, this higher sensitivity of the biosensors towards biomolecules usually comes at the cost of high sensitivity to the ambient environment change. Thus the requirement on the temperature stability for a biosensing system with good performance is stringent. For example, the temperature stability of ±0.01 ˚C is a must for today's commercial SPR instruments [41].

Currently there exist several approaches to overcome this problem. The most straightforward method is actively controlling and stabilizing the temperature with external cooler or heater, but at the cost of adding complexity to the system, with extra space and higher power consumption. For optical biosensing, the second solution can be using a reference element, which has an identical structure with the sensing element. By differentiating the signals acquired from these two elements, the correct sensing signal can be obtained [42]. But this principle works under the condition that the reference element is well isolated from the sensing analytes with a cladding layer while both the reference and sensing element have the same feeling towards the temperature change. The third method to realize the on-chip temperature independence goes to making the key optical functioning components or transducers themselves athermal. Thermal compensation with

the upper cladding which has an opposite TO coefficient to the core has been considered to be an effective method. For silicon-based electronic-photonic integration, it has been achieved by polymer overlay, where intensive studies can be found [38, 43, 44]. For silicon wire optical biosensing, as it specifically require an aqueous solution as upper cladding, special design and working principle are required, such as that proposed in [45]. For polymer-based integrated components, all-polyemer structure can be an effective and attractive solution [40]. Recent progress has been made on the athermalization of interfence-based devices with special circuit design without resorting to upper cladding compensation [39, 46].

1.4 Thesis outline

The outline of this work is as follows:

In chapter 2, we describe a novel inorganic-organic hybrid polysiloxane polymer material which is called PSQ-Ls. This self-developed optical material is first developed at Dalian University of Technology under the collaboration with its chemical department. It not only has good optical properties and thermal stability, the solvent-free and good UV curing property makes it suitable to be process with novel fabrication technique such as nanoimprint lithography (NIL).

In chapter 3, based on the available material, an UV-based soft imprint technique is developed to fabricate polymer-based integrated photonic devices. Compared with traditional semiconductor method, it is much more fast, efficient and low cost. Two different waveguide structures can be realized by this method, which are ridge shaped waveguide structure and inverted-rib waveguide structure, respectively. Critical technique problems and their solutions will be presented. Different kinds of optical devices are successfully obtained, which include straight waveguides, power splitters, microring notch filters, microring add-drop filters and so on. Detailed characterization of these devices will be given.

In chapter 4, the polymer microring notch filter is applied to solve one of the key issues on radio-over-fiber (ROF) technique, which is fiber dispersion induced fading effect. Optical single sideband (OSSB) modulation is achieved by the filtering function of the polymer microring notch filter, which greatly enhances the microwave signal transmission quality.

In chapter 5, a label-free optical biosensor is developed with the high performance polymer microring resonator. The issues considering the design and characterization of the sensor will be discussed. A surface biological functionalization protocol is built for the polymer-based microring resonator. With the home-built measuring system, two different kinds of sensing mechanism, bulk sensing and surface sensing, are demonstrated.

In chapter 6, we investigate a new coupling mechanism between the optical fiber and polymer waveguide, which is surface coupling. Although it has been intensively researched for high refractive index material platform (e.g. SOI), very limited work is done on polymer. The simulation, fabrication and measurement results will be given.

In chapter 7, athermalization is achieved for a key passive photonic component, Arrayed Waveguide Grating (AWG), with a SOI plus polymer hybrid structure, which would be of great use in all-optical networks as (de-)multiplexers and wavelength routers and as part of more complex photonic switches, sources or receivers. Design consideration, simulation and characterization will be present. At the same time, an all-polymer structure is proposed, aiming to eliminate the temperature induced noise during biosensing. Simulation results will be given and discussed.

1.5 List of publications

International Journals

J. Ren, L. Wang, X. Han, J. Cheng, H. Lv, J. Wang, X. Jian, M. Zhao, L. Jia, "Organic Silicone Sol-gel Polymer as Non-covalent Carrier of Receptor Proteins for Label-free Optical Biosensor Application," (to be submitted).

L. Wang, J. Ren, X. Han, T. Claes, X. Jian, P. Bienstman, R. Baets, M. Zhao, G. Morthier, "A Label-Free Optical Biosensor Built on a Low Cost Polymer Platform," to be published, IEEE Photonics Journal, (2012).

L. Wang, Y. Li, M. Porcel, D. Vermeulen, X. Han, J. Wang, X. Jian, R. Baets, M. Zhao, G. Morthier, "A polymer-based surface grating coupler with an embedded Si3N4 layer," Journal of Applied Physics, 111(11), p. 114507, (2012).

L. Wang, W. Bogaerts, P. Dumon, S. Selvaraja, T. Jie, S. Pathak, X. Han, J. Wang, X. Jian, M. Zhao, R. Baets, G. Morthier, "Athermal AWGs in SOI by overlaying a polymer cladding on narrowed arrayed waveguides," Applied Optics, 51(9), pp. 1251-1256, (2012).

X. Han, J. Zhang, L. Wang, Y. Gu, M. Wang, J. Teng, J. Wang, X. Jian, G. Morthier, and M. Zhao, “Quasi-single-sideband radio over fiber transmission with a polymer-based waveguide microring resonator,” Optical Engineering, 50(12), pp. 124601-1/12406-7, (2011).

H. Yu, L. Wang; Z. Wang; X. Han and M. Zhao, “Alkyl-substituted carboxyl-containing polyaryletherketones and the crosslinking modifications with various bisphenols: preparation and optical properties,” Polymer 51(14), pp. 3269-3276, (2010).

J. Zhang, J. Wang, L. Wang, X. Han, M. Zhao, and X. Jian, “Synthesis of polysilisiquioxane used as core layer material of optical waveguide,” Journal of Sol-Gel Science and Technology, 56(2), pp. 197-202, (2010).

International Conferences

L. Wang, X. Han, Y. Gu, H. Lv, J. Cheng, J. Teng, J. Ren, J. Wang, X. Jian, M. Zhao, "Optical biosensors utilizing polymer-based athermal microring resonators", SPIE Photonics Europe 2012, 8427, pp. 842731, (2012).

L. Wang, Y. Li, M. Porcel, D. Vermeulen, X. Han, J. Wang, X. Jian, M. Zhao, G. Morthier, "Grating couplers in polymer with a thin Si3N4 layer embeded", SPIE Photonics West 2012, 8258, pp. 825817, (2012).

L. Wang, Kodeck, Valerie, Van Vlierberghe, Sandra, Ren, Jun, Teng, Jie, Han, Xiuyou, Jian, Xigao, R. Baets, G. Morthier, M. Zhao, "A low-cost photonic biosensor built on polymer platform", Asia Communications and Photonics Conference (ACP2011), 8311, pp. 831122, (2011).

L. Wang, W. Bogaerts, P. Dumon, S. Selvaraja, G. Morthier, Jie Teng, Xiuyou Han, Xigao Jian, Mingshan Zhao, R. Baets, "Athermal AWGs in SOI by overlaying a Polymer Cladding on Narrowed Arrayed Waveguides," Optical Fiber Communication Conference (OFC), pp. paper OThV6 (2011).

L. Wang, G. Morthier, X. Han, X. Jian, M. Zhao, R. Baets, "All-polymer microring resonator fabricated by UV imprint technique," in Proceedings of the 2010 Annual Symposium of the IEEE Photonics Benelux Chapter, Netherlands, (2010).

1.6 References

[1] S.E. Miller, “Integrated Optics: An Introduction,” Bell Syst. Tech. J. 48, 2059-2068 (1969).

[2] A. Jenkins, “The road to nanophotonics,” Nature Photon. 2, 258-260 (2008).

[3] M. Salib, L. Liao, R. Jones, M. Morse, A. Liu, D. S.-Rubio, D. Alduino, M. Paniccia, "Silicon Photonics," Intel Technol. J. 8, 143-160 (2004).

[4] M. Smit, "Photonic integration," Telektronikk 2.2005, 66-71, (2005).

[5] L. Eldada and L. W. Shacklette, “Advances in Polymer Integrated Optics,” IEEE J. Sel. Top. Quantum Electron. 6, 54-68 (2000).

[6] L. Eldada, "Telecom optical componentry: past, present, future", Proc. SPIE 4604, 1-15 (2001).

[7] H. Ma, A. K.-Y. Jen, and L. R. Dalton, "Polymer-based optical waveguides: Materials, processing, and devices," Adv. Mater. 14, 1339-1365 (2002).

[8] L. Eldada, "Polymer microphotonics", Proc. SPIE 5225, 49-60 (2003).

[9] L. Eldada, "Organics in optoelectronics: advances and roadmap," Proc. SPIE 6124, 260-274 (2006).

[10] Y. Kuwana, K. Takayama, S. Takenobu, and Y. Morizawa, “Perfluoropolymer optical waveguide comparable to silica in optical properties and reliabilities,” in 6th International Conference on Polymers and Adhesives in Microelectronics and Photonics. (Polytronic 2007), pp. 198-201.

[11] G. Li, J. Wang, G. Su, X. Jian, L. Wang, and M. Zhao, “Synthesis and characterization of fluorinated crosslinkable poly(phthalazinone ether)s bearing tetrafluorostyrene groups for optical waveguides,” Polym. J. 42, 880-886 (2010).

[12] T. Han, S. Madden, M. Zhang, R. Charters, and B. L.-Davies, "Low loss high index contrast nanoimprinted polysiloxane waveguides," Opt. Express 17, 2623-2630 (2009).

[13] B. Yang, L. Yang, R. Hu, Z. Sheng, D. Dai, and Q. Liu, and S. He, “Fabrication and Characterization of Small Optical Ridge Waveguides Based on SU-8 Polymer,” J. Lightwave Technol. 27, 4091-4096 (2009).

[14] L. Yang, B. Yang, Z. Sheng, J. Wang, D. Dai, and S. He, “Compact 2×2 tapered multimode interference couplers based on SU-8 polymer rectangular waveguides,” Appl. Phys. Lett. 93, 203304 (2008).

[15] A. K. Das, "Laser Direct Writing Polymeric Single-Mode Waveguide Devices with a Rib Structure," Appl. Opt. 42, 1236-1243 (2003).

[16] Z. Liu et al., “An azobenzene functionalized polymer for laser direct writing waveguide fabrication,” Opt. Commun. 273, 94-98 (2007).

[17] Q. Liu, K. S. Chiang, L. Reekie, and Y. T. Chow, "CO_2 laser induced refractive index changes in optical polymers," Opt. Express **20**, 576-582 (2012).

[18] S.Y. Chou, P.R. Krauss, P.J. Renstrom, “Imprint Lithography with 25-Nanometer Resolution,” Science 272, 85–87 (1996).

[19] S.Y. Chou, C. Keimel, J. Gu, “Ultrafast and Direct Imprint of Nanostructures in Silicon,” Nature 417, 835–837 (2002).

[20] L. J. Guo, “Topical Review: Recent progress in nanoimprint technology and its applications,” J. Phys. D: Appl. Phys. 37, R123-R141 (2004).

[21] L. J. Guo, "Nanoimprint Lithography: Methods and Material Requirement," Adv. Mater 19, 495-513 (2007).

[22] C. Y. Chao and L. J. Guo, “Polymer microring resonators fabricated by nanoimprint technique,” J. Vac. Sci. Technol., B 20, 2862-2866 (2002).

[23] Y. Y. Huang, G. T. Paloczi, J. K. S. Poon, and A. Yariv, “Bottom-up soft-lithographic fabrication of three-dimensional multilayer polymer integrated optical microdevices,” Appl. Phys. Lett. 85, 3005-3007 (2004).

[24] T. Haatainen, "Stamp fabrication by step and stamp nanoimprinting," PhD thesis, VTT, Espoo, Finland (2011).

[25] A. Flores, S. Song, S. Baig, and M. R. Wang, "Vacuum-assisted microfluidic technique for fabrication of guided wave devices," IEEE Photonics Technol. Lett. 20, 1246-1248 (2008).

[26] M. C. Estevez, M. Alvarez, and L. M. Lechuga, “Integrated optical devices for lab-on-a-chip biosensing applications,” Laser Photonics Rev. 25 (2011).

[27] S. Balslev, AM. Jorgensen, B. Bilenberg, KB. Mogensen, D. Snakenborg, O. Geschke, JP. Kutter, A. Kristensen, “Lab-on-a-chip with integrated optical transducers” Lab Chip 6, 213-217 (2006).

[28] P. S. Dittrich and A. Manz, “Lab-on-a-chip: microfluidics in drug discovery,” Nat. Rev. Drug Discovery 5, 210-218 (2006).

[29] X. Fan, I. M. White, S. I. Shopova, H. Zhu, J. D. Suter, and Y. Sun, “Sensitive optical biosensors for unlabeled targets: a review,” Anal. Chim. Acta 620 8-26 (2008).

[30] P. Debackere, “Nanophotonic Biosensor based on Surface Plasmon Interference,” PhD thesis, Ghent University, Ghent, Belgium (2010).

[31] A. Densmore, D.-X. Xu, S. Janz, P.Waldron, J. Lapointe, T.Mischki, G. Lopinski, A. Delage, J. H. Schmid, and P. Cheben, “Sensitive Label-Free Biomolecular Detection Using Thin Silicon Waveguides,” Adv. Opti. Technol. 2008, 1-9 (2008).

[32] N. Bamiedakis, T. Hutter, R. V. Penty, I. H. White, and S. R. Elliott, "Low-cost PCB-integrated Polymer Waveguide Sensor for Gas Detection," in CLEO:2011 - Laser Applications to Photonic Applications, OSA Technical Digest (CD) (Optical Society of America, 2011), paper CThC5.

[33] http://www.semofs.com/index.php?id=28

[34] R. Kirchain and L. Kimerling, “A roadmap for nanophotonics,” Nat. Photonics 1, 303-305 (2007).

[35] L. C. Kimerling, D. Ahn, A. B. Apsel, M. Beals, D. Carothers, Y.-K. Chen, T. Conway, D. M. Gill, M. Grove, C.-Y. Hong, M. Lipson, J. Liu, J. Michel, D. Pan, S. S. Patel, A. T. Pomerene, M. Rasras, D. K. Sparacin, K.-Y. Tu, A. E.

White and C. W. Wong, “Electronic-photonic integrated circuits on the CMOS platform,” Proc. SPIE 6125, 612502, 612502-10 (2006).

[36] G. Van Steenberge, N. Hendrickx, E. Bosman, J. Van Erps, H. Thienpont, and P. Van Daele, "Laser ablation of parallel optical interconnect waveguides," IEEE Photonics Technol. Lett. 18, 1106-1108 (2006).

[37] X. Wang, W. Jiang, L. Wang, H. Bi, and R. T. Chen, “Fully Embedded Board-Level Optical Interconnects From Waveguide Fabrication to Device Integration,” Opt. Express 26, 243-250 (2008).

[38] V. Raghunathan, W. N. Ye, J. Hu, T. Izuhara, J. Michel, and L. Kimerling, "Athermal operation of Silicon waveguides: spectral, second order and footprint dependencies," Opt. Express 18, 17631-17639 (2010).

[39] B. Guha, A. Gondarenko, and M. Lipson, "Minimizing temperature sensitivity of silicon Mach-Zehnder interferometers," Opt. Express 18, 1879-1887 (2010).

[40] N. Keil, H. H. Yao, and C. Zawadzki, "Athermal polarisation-independent arrayed-waveguide grating (AWG) multiplexer using an all-polymer approach," Appl. Phys. B 73, 619-622 (2001).

[41] K. B. Gylfason, “Integrated Optical Slot-Waveguide Ring Resonator Sensor Arrays for Lab-on-Chip Applications,” PhD thesis, KTH-Royal Institute of Technology, Stockholm, Sweden (2010).

[42] D.-X. Xu, M. Vachon, A. Densmore, R. Ma, S. Janz, A. Delâge, J. Lapointe, P. Cheben, J. H. Schmid, E. Post, Sonia Messaoudène, and Jean-Marc Fédéli, "Real-time cancellation of temperature induced resonance shifts in SOI wire waveguide ring resonator label-free biosensor arrays," Opt. Express 18, 22867-22879 (2010).

[43] J. Teng, P. Dumon, W. Bogaerts, H. Zhang, X. Jian, X. Han, M. Zhao, G. Morthier, and R. Baets, "Athermal Silicon-on-insulator ring resonators by overlaying a polymer cladding on narrowed waveguides," Opt. Express 17, 14627-14633 (2009).

[44] M. M. Milošević, N. G. Emerson, F. Y. Gardes, X. Chen, A. A. D. T. Adikaari, and G. Z. Mashanovich, "Athermal waveguides for optical communication wavelengths," Opt. Lett. 36, 4659-4661 (2011).

[45] K. Kim; R. M. Pafchek, T. L Koch, ” Athermal silicon waveguides for aqueous evanescent biosensor applications,” in IEEE Photonics Conference (IPC 2011), p. 419-420.

[46] B. Guha, B. B. C. Kyotoku, and M. Lipson, "CMOS-compatible athermal silicon microring resonators," Opt. Express 18, 3487-3493 (2010).

Chapter 2 Inorganic-organic hybrid polymer waveguide material PSQ-Ls

2.1 Introduction

Integrated optics plays an increasingly important role in optical communication networks and optical sensor systems. Up to now, many different optical materials have been used for integrated optical waveguide device fabrication. Compared to other materials such as silica, lithium niobate and III–V compound semiconductors, polymer materials offer many unique advantages, for example, low cost, large thermal index changes, low thermal conductivities, compatibility with Si and GaAs fabrication technologies, and high-volume production. Tailored polymer materials offer high structural flexibility through combination of the monomers, and accurate control of the materials' refractive indices and properties can be obtained.

A lot of effort has been devoted to improve the performance of optical polymers [1-3]. Although different kinds of polymers such as acrylates, polyamides, polycarbonates, polyesters, siloxanes, epoxy resins, sol-gels and so on, have been used for integrated optics, some properties of these materials are still unsatisfactory, especially in terms of optical loss and thermal stability [4-7]. While some commercial ones have good performances, the high prices prohibit their wide use. Besides that, fabrication technique adapted to the properties of the used polymer should be developed.

In this study, we used a group of liquid photopatternable inorganic-organic hybrid polymer material polysiloxanes (named as PSQ-Ls) obtained by a sol-gel process at room temperature. First, the process to synthesize PSQ-Ls materials is presented. Then the optical properties of waveguide films, including refractive index, optical loss, thermo-optical coefficient and thermal stability, are measured and characterized in detail. Finally, typical waveguide structures based on PSQ-Ls are fabricated preliminarily by UV imprint technology.

2.2 **Materials synthesis and waveguide film preparation**

PSQ-Ls are synthesized by a sol-gel process from phenyl trimethoxysilane (PhTMS), methyl trimethoxysilane (MTMS) and 3-(methacryloxy)propyl trimethoxysilane (MAPTMS). The chemical reaction process is illustrated in Fig. 2.1. The mixture of the above-mentioned starting materials combined with 0.1 M aqueous hydrogen chloride (pH=1.0) in a sealed container, was stirred for 2 hours at 25 °C. The resulting solvent was dissolved in an equal volume of ether and then washed by deionized water until the pH was 6~7. The solvent was removed under vacuum at 40°C and then transparent liquid PSQ-Ls were obtained.

For the hydrolytic sol-gel process, the chemical structure and viscosity of the product are determined mainly by the molar ratio of water to silica precursors when the reaction temperature, time and pH value of the solution are fixed. Here, two kinds of PSQ-Ls with high refractive index (PSQ-LH) and low refractive index (PSQ-LL) are prepared from different feed ratios of PhTMS, MTMS and MAPTMS and a proper ratio of water to methoxysilane (represented by R). Table 2.1 gives the characteristics of the two kinds of liquid hybrid material PSQ-Ls. It can be seen that PSQ-LH with higher PhTMS feed possesses higher viscosity (η=813 mPa·s) and the resulting waveguide film possesses higher refractive index (n_{TE}=1.5212 @1310 nm) compared with PSQ-LL with lower PhTMS feed.

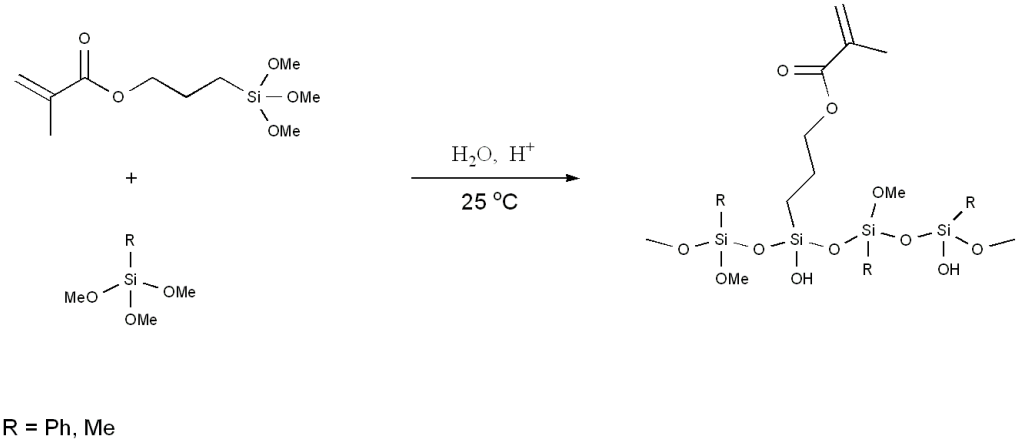

Fig. 2.1 Synthetic route of PSQ-Ls by a sol-gel process.

Table 2.1 Characteristics of two kinds of liquid hybrid material PSQ-Ls.

	MAPTMS:MTMS:PhTMS (Molar ratio)	R	η* (mPa•s@25°C)	n_{TE} @1310nm	n_{TE} @1550nm
PSQ-LH	15:5:80	1.2	813	1.5212	1.5198
PSQ-LL	10:75:15	1.3	658	1.4482	1.4478
*Measured by rotational viscometer.					

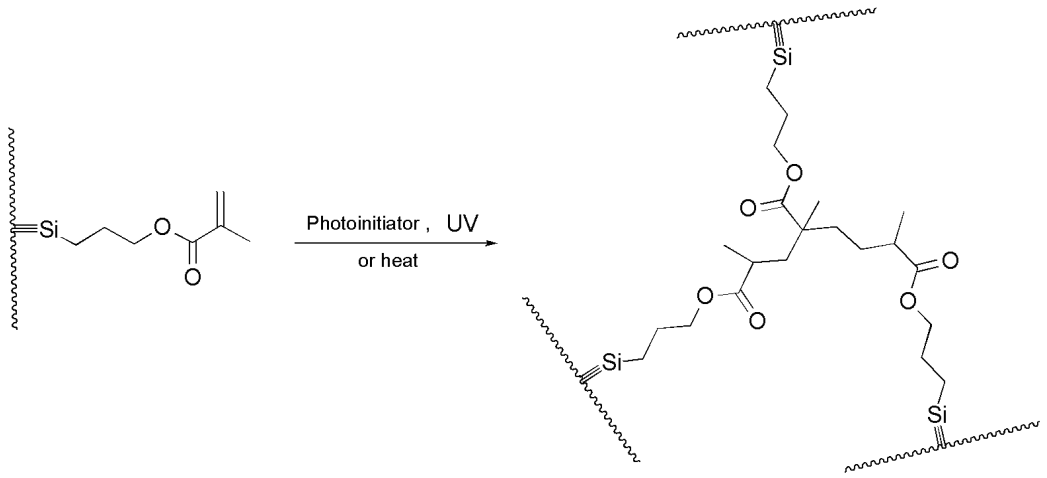

Fig. 2.2 Curing process of methacrylic groups by UV exposure or heat treatment.

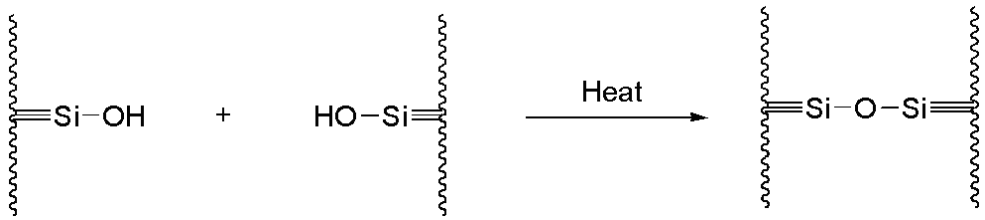

Fig. 2.3 Curing process of Si–OH by heat treatment.

The preparation process for waveguide films is as follows: a 0.8 wt% photoinitiator PI-184 (1-hydroxycyclo-hexylphenylketone, IGM) was mixed with PSQ-Ls, which could make PSQ-Ls photopatternable for the photocuring

process and UV imprint technology. The resulting liquid was filtered through a 0.22 μm microfilter to remove the dust. The transparent lacquer was spin-coated on a Si or quartz substrate. The layer was then exposed to UV light (λ=365 nm, power density approximately 25 mW/cm^2) for 120 seconds in nitrogen gas. After the UV illumination, the sample was baked in the convection oven at 180 °C for 2 hours, and at 200 °C for 2 hours. During the photocuring process, C=C double bonds in the sol-gel product (See Fig. 2.1) were cross-linked by UV irradiation as illustrated in Fig. 2.2. And then in the heat treatment step, the residue of Si-OH (See Fig. 2.1) in the films further carried out condensation at high temperature (as shown in Fig. 2.3) to form good waveguide films.

2.3 **Waveguide film characteristics**

2.3.1 Refractive index: tuning and birefringence

Exact tuning of the refractive index of PSQ-Ls can be achieved by simple blending of PSQ-LH and PSQ-LL. The similar structure between PSQ-LH and PSQ-LL and their little residual Si-OH groups allows to blend the two liquids in any ratio without phase separation. The refractive indices of PSQ-Ls with variation of PSQ-LL content from 0 wt% to 100 wt% were measured using a Prism Coupler SPA-4000 at a wavelength of 1310 nm and 1550 nm, respectively. Fig. 2.4(a) and Fig. 2.4(b) give the measurement results. The refractive index can be tuned from 1.4482 to 1.5212 at 1310 nm and from 1.4478 to 1.5198 at 1550 nm by varying the PSQ-LL content. It can be seen that the relationship between the refractive index of the waveguide films and the weight contents of PSQ-LL are perfectly linearly fitted as follows:

$$n_{TE}(x) = 1.5212 - 0.00073x \qquad @1310nm \tag{2.1}$$

$$n_{TE}(x) = 1.5198 - 0.00072x \qquad @1550nm \tag{2.2}$$

So the refractive index of the waveguide material can be obtained accurately according to equation 2.1 and 2.2 by blending PSQ-LL and PSQ-LH. Moreover, all of the waveguide films exhibited reasonably small birefringences which were below 0.0005 as shown in Fig. 2.5.

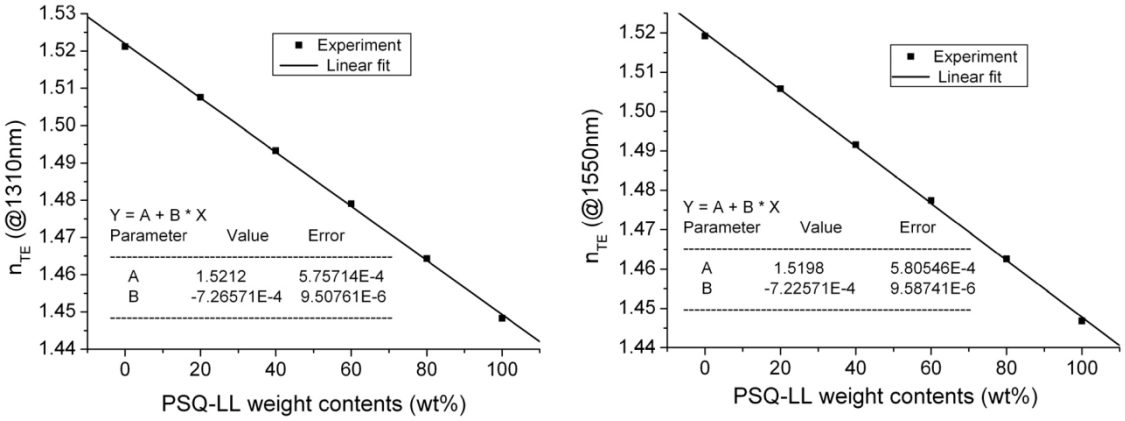

Fig. 2.4 Refractive index of the films versus the weight content of PSQ-LL. (a) The refractive index n_{TE} at 1310 nm. (b) The refractive index n_{TE} at 1550nm.

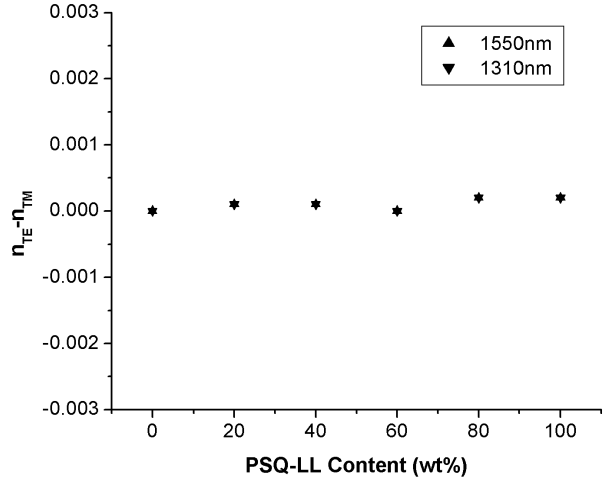

Fig. 2.5 Birefringences (n_{TE}-n_{TM}) of the waveguide films versus the weight content of PSQ-LL.

2.3.2 Optical loss

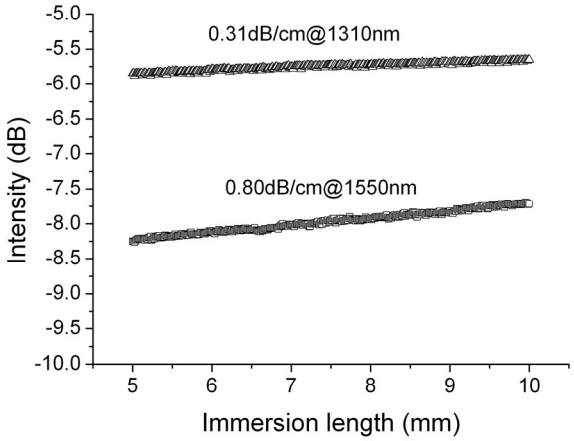

Fig. 2.6 Optical losses of a PSQ-LH waveguide film.

The optical losses of slab waveguides (17×75 mm) prepared on quartz wafers were measured at 1310 nm and 1550 nm by the liquid immersion technique (Prism Coupler SPA-4000). Fig. 2.6 describes the optical losses of a PSQ-LH film at 1310 nm and 1550 nm with a waveguide film thickness of 6.2 μm. The optical losses of the waveguide film are 0.31 dB/cm at 1310 nm and 0.80 dB/cm at 1550nm, respectively. For the PSQ-Ls, absorption losses arise from vibration overtones of the aliphatic and hydroxyl groups present in the material. Absorption effects in general are more prominent at the higher wavelengths, with hydroxyl groups having an especially strong effect at the 1550nm wavelength [8].

2.3.3 Thermo-optical coefficient (TOC) of PSQ-Ls

The thermo-optical coefficient is another important parameter of an optical material. Whereas inorganic materials (e.g. Si, SiO_2, etc.) usually have positive TOC value, owing a negative TOC is the unique feather of polymer material. The large TOC of polymer material is very helpful in designing and realizing athermal (temperature-independent) optical devices [9], which will be illustrated in detail in Chapter 7. The characterization of the TOC of PSQ-Ls series material is achieved by measuring the refractive index of the prepared

film under different temperatures followed by linear fitting. The results are shown in Fig. 2.7. As can be seen, PSQ-LH has a TOC of -2.4×10^{-4} /˚C at both 1310 nm and 1550 nm wavelength, while that for PSQ-LL at these two wavelengths is -2.2×10^{-4} /˚C.

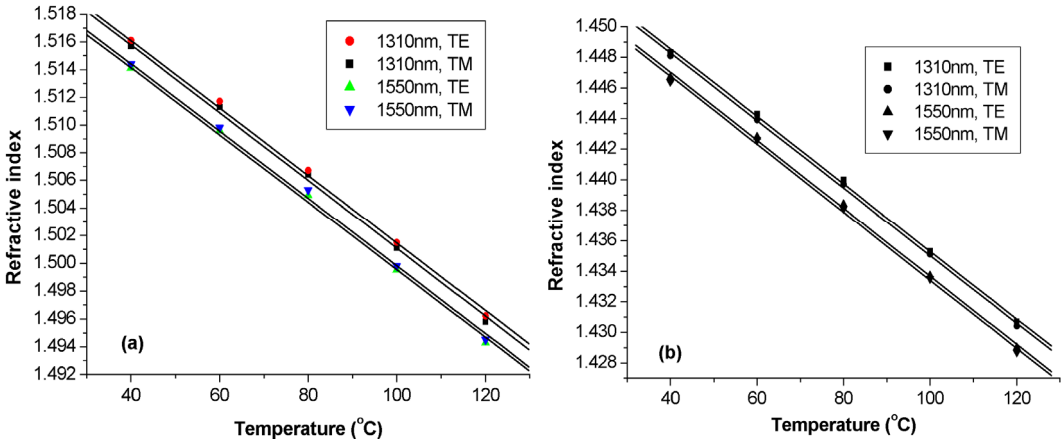

(a) (b)

Fig. 2.7 The measurement results of the refractive index of PSQ-Ls series material under different temperatures and their linear fitting. (a) PSQ-LH and (b) PSQ-LL.

2.3.4 Thermal stability

Thermogravimetric analysis (TGA) was performed on the Perkin-Elmer 7 Series Thermal Analysis System in air and N_2 conditions, respectively. Decomposition temperatures (Td) were recorded when the weight loss of the sample reached 1% in TGA. Fig. 2.8 (a) and (b) indicate that the thermal decomposition represented by a 1% weight loss did not occur below 297 °C (in air) and 340 °C (in N_2) for the PSQ-LH waveguide film and below 313 °C (in air) and 370 °C (in N_2) for the PSQ-LL waveguide film at a heating rate of 20 °C/min. These results reveal excellent thermal stability of the prepared materials and meet the thermal stability requirement for waveguide fabrication.

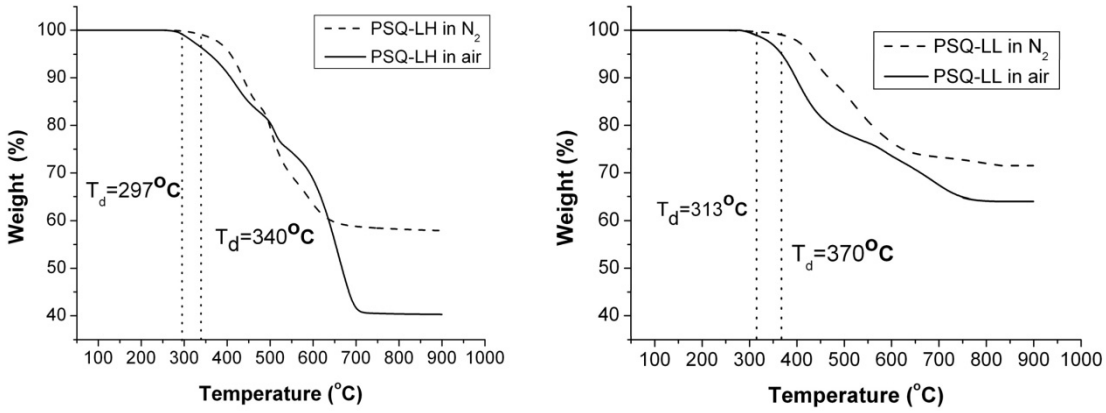

(a) (b)

Fig. 2.8 TGA data of PSQ-Ls cured films in (a) air and (b) N_2 conditions. (a) PSQ-LH. (b) PSQ-LL.

2.4 **Preliminary waveguide imprint experiment**

PSQ-Ls can have good photopatternable function after addition of the photoinitiator PI-184. UV imprint lithography [10, 11] was preliminarily investigated to fabricate some polymer waveguide structures. In the UV imprint process, quartz flakes were used as substrates. After the polymer film was spin-coated on the quartz substrates, the silicon mold was pressed onto the waveguide film. Then UV light was illuminated through the quartz substrates onto the polymer film for 120 seconds. After the silicon mold was removed, the waveguide structures were post-baked at 200 °C for 2 hours. Fig. 2.9 shows the waveguide structure patterns obtained by scanning electron microscopy. The waveguide surface and edge are smooth and no deformation is found. This novel fabrication technique will be discussed in detail in Chapter 3.

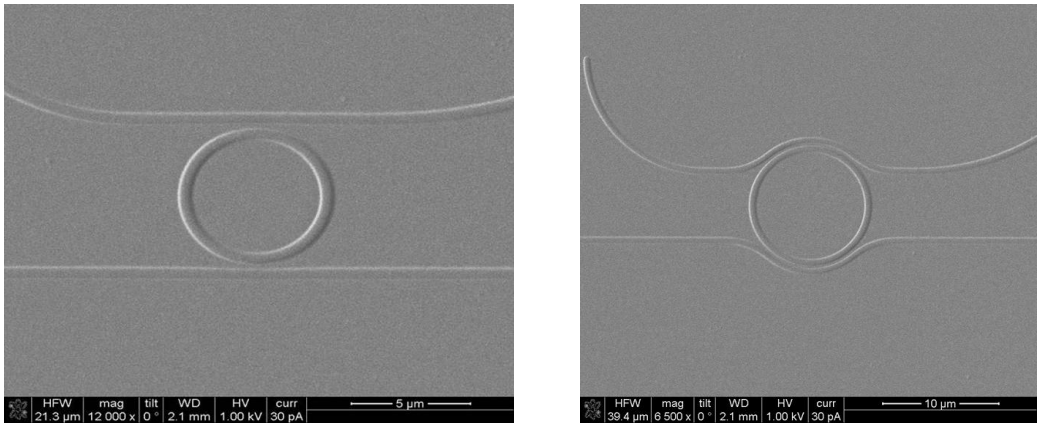

(a) Waveguide ring resonators

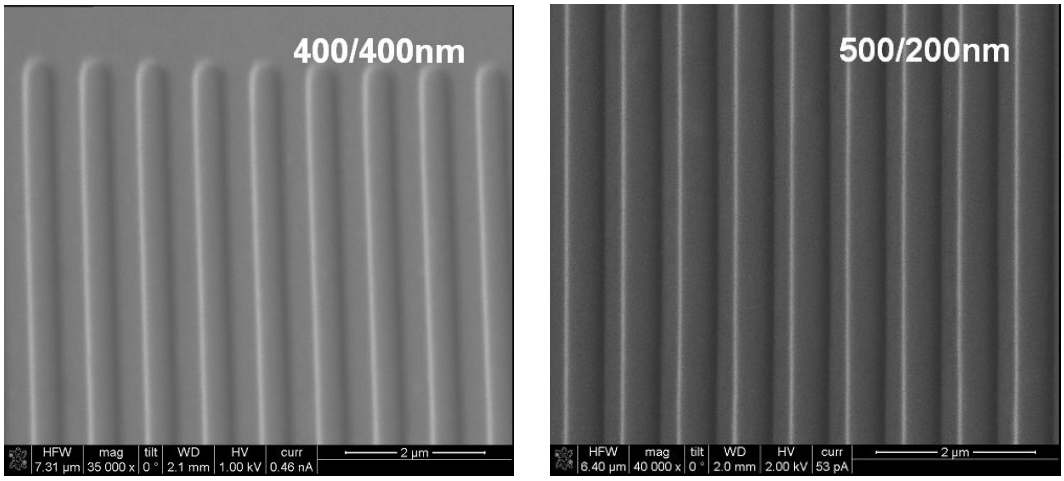

(b) Waveguide gratings

Fig. 2.9 SEM pictures of PSQ-Ls based waveguide structures obtained by UV imprint technology. (a) Waveguide ring resonators. (b) Waveguide gratings.

2.5 **Conclusions**

A new group of liquid inorganic-organic hybrid polymer materials (PSQ-Ls) have been synthesized by sol-gel process at room temperature. The properties including refractive index tuning, birefringence, optical loss, thermal-optical coefficient and thermal stability have been measured and analyzed, and are listed in Table. 2.2. The results prove that self-developed PSQ-Ls materials can be good candidates for waveguide fabrication, with uncompromised performances compared to commercial polymers but at a

very lost cost. Prototypes of polymer waveguide structures were fabricated by UV imprint technology. Preliminary tests of UV imprint lithography were made on this material. The results show that the inorganic-organic hybrid polymers are promising materials for optical waveguides.

Table 2.2 Detailed properties of the PSQ-Ls series material.

	PSQ-LL	*PSQ-LH*
Refractive index @1310 nm	1.4503	1.5219
Refractive index @1550 nm	1.4485	1.5199
Birefringence ($\Delta n = n_{TE}-n_{TM}$)	-0.0005<Δn<0.0005	-0.0005<Δn<0.0005
Thermo-optical coefficient (dn/dT)	~ -2.2×10^{-4}/℃	~ -2.4×10^{-4}/℃
Slab waveguide loss	Not measured	0.7~0.8dB/cm@1550 nm
	Not measured	0.2~0.3dB/cm@1310 nm
Degradation Temp (1wt%)	322 ±10 ℃	303 ±10 ℃

2.6 **References**

[1] H. Ma, A. K. Y. Jen, and L. R. Dalton, "Polymer-based optical waveguides: Materials, processing, and devices," Adv. Mater. 14, 1339-1365 (2002).

[2] A. Norris, J. DeGroot, T. Ogawa, T. Watanabe, T. Kowalczyk, A. Baugher, and R. Blum, “High reliability of silicone materials for use as polymer waveguides,” Proc. SPIE 5212, 76-82 (2003).

[3] G. Li, J. Wang, G. Su, X. Jian, L. Wang, and M. Zhao, "Synthesis and characterization of fluorinated crosslinkable poly(phthalazinone ether)s bearing tetrafluorostyrene groups for optical waveguides," Polym. J. 42, 880-886 (2010).

[4] L. W. Shacklette, R. Blomquist, J. M. Deng, P. M. Ferm, M. Maxfield, J. Mato, and H. Zou, "Ultra-low-loss acrylate polymers for planar light circuits," Adv. Funct. Mater. 13, 453-462 (2003).

[5] M. Usui, M. Hikita, T. Watanabe, M. Amano, S. Sugawara, S. Hayashida, and S. Imamura, "Low-loss passive polymer optical waveguides with high environmental stability," J. Lightwave Technol. 14, 2338-2343 (1996).

[6] D.-W. Kim, S. H. Ahn, I.-K. Cho, D.-M. Im, S. M. S. Muslim, and H.-H. Park, “Fabrication of thermally stable and cost-effective polymeric waveguide for optical printed-circuit board,” Opt. Express 16, 16798-16805 (2008).

[7] S. Takenobu and T. Okazoe, "Heat Resistant and Low-Loss Fluorinated Polymer Optical Waveguides at 1310/1550 nm for Optical Interconnects," in 37th European Conference and Exposition on Optical Communications, OSA Technical Digest (CD) (Optical Society of America, 2011), paper We.10.P1.31.

[8] O. Soppera, P. J. Moreira, A. P. Leite, P. V. S. Marques, “Low-loss photopatternable hybrid sol-gel materials,” J. Sol-Gel Sci. Technol. 35, 27-39 (2005).

[9] L. Wang, W. Bogaerts, P. Dumon, S. K. Selvaraja, J. Teng, S. Pathak, X. Han, J. Wang, X. Jian, M. Zhao, R. Baets, and G. Morthier, "Athermal arrayed

waveguide gratings in silicon-on-insulator by overlaying a polymer cladding on narrowed arrayed waveguides," Appl. Opt. 51, 1251-1256 (2012).

[10] S.Y. Chou, P.R. Krauss, P.J. Renstrom, “Imprint Lithography with 25-Nanometer Resolution,” Science 272, 85–87 (1996).

[11] L. J. Guo, “Nanoimprint Lithography: Methods and Material Requirement,” Adv. Mater 19, 495-513 (2007).

Chapter 3 Polymer-based photonic devices: fabrication and characterization

3.1 Introduction

In the previous chapter, polymer material PSQ-Ls with good optical properties and thermal stability was obtained. Its tunable refractive index property provides a certain flexibility for the waveguide design and fabrication. For example, its high refractive index component PSQ-LH can be used for the waveguide core while the low refractive index component PSQ-LL can be used for waveguide cladding. We don't need to resort to and incorporate another material where the compatibility of two different types of materials may become a severe problem during fabrication. Thus the next aim is to find a suitable fabrication process for this kind of material.

As mentioned in the introduction, so far there are several methods and techniques available for the fabrication of polymer based photonic devices. The most adopted one is still the standard semiconductor fabrication process, with which the inorganic material is dealt with. The detailed scheme of this process is shown in Fig. 3.1. In fact, most of our early works were also based on this process to fabricate PSQ-Ls polymer waveguides [1]. As can be seen from it, the whole process is rather complicated, and normally includes photo resist patterning, metal mask formation, dry etching and so on [2, 3]. These are steps that have great chances to introduce extra edge roughness on the patterns, thus the final problem would fall into the same cycle of repeated fabrication and optimization as for inorganic material. Even worse is that many works have proven that such optimization differs from one material to another. It means that the optimized processing parameters for one material cannot be simply applied to the other. Considering the varieties of polymer material, the problems mentioned above would meet great obstacles thus preventing this method to be a good choice to process the polymer waveguide material. Besides the standard semiconductor method, recently direct laser writing also appears as an approach for polymer material. It is a microfabrication and

micropatterning method that encompasses modification, subtraction, and addition processes capable of creating patterns of materials directly on substrates without the need for lithography or masks. It has been found to be very useful for unconventional structures hardly achieved by standard planar lithography techniques. The tilted micro-mirror widely adopted for optical interconnects on printed circuit boards (PCB) is such an example [4, 5]. Unfortunately, the fundamental weakness of this method is the low throughput. The fabrication cost for the polymer based photonic devices will inevitably be increased.

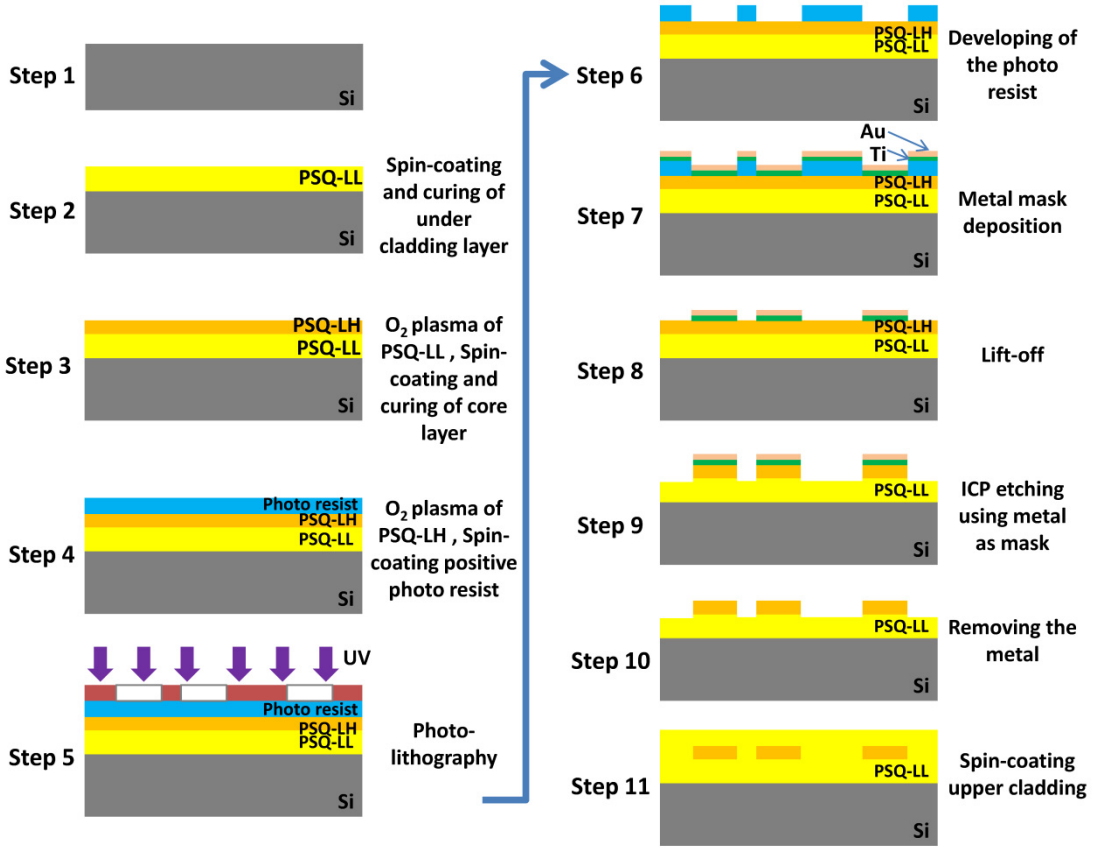

Fig. 3.1 The fabrication of PSQ-Ls polymer waveguides using conventional lithography and dry etching process.

In this chapter, a UV-based soft imprint technique will be demonstrated as an alternative to process the waveguide polymer. First, early work related to hard mold imprinting and the obstacles that were met will be shortly reviewed.

Then the detailed fabrication process will be described together with the characteristic difficulties of this method. Ideally, micro/nanoimprinting should use dedicated and expensive imprint equipment. How to circumvent these difficulties when no such equipment is accessible will be shown. Efficacy of this replication method is demonstrated by characterization of the fabricated devices. Finally, efforts are paid to add heaters onto the devices and related problems will be discussed.

3.2 **Hard mold imprint**

3.2.1 Imprinting procedures

At the early stage of this thesis, the hard mold imprinting was tried on our developed polymer waveguide material. The fabrication process is shown in Fig. 3.2. Considering the polymerization mechanism of the polymer PSQ-Ls, either the mold or the substrate needs to be transparent to enable the UV light to penetrate through to cure the polymer before demolding. The attempt to imprint by silicon mold on silicon substrate, and to depend solely on thermal curing failed during our experiments. Thus in our case, we chose a quartz substrate and a silicon mold. The procedures are described below: first, both the quartz substrate and the silicon mold are treated with piranha ($3\,H_2SO_4 : 1H_2O_2$) to make the surfaces enough clean. The surface energy increases dramatically after cleaning, resulting in a hydrophilic property. Then the silicon mold is treated with 1H,1H,2H,2H-Perfluorooctyltrichlorosilane, which greatly reduces the surface energy of the silicon mold, making it rather hydrophobic [6, 7]. The importance of this distinct surface energy difference is that it decides whether or not the mold patterns can be transferred successfully from mold to substrate. Secondly, the silicon mold is brought into close contact and then pressed against the quartz substrate after the spin-coating of a layer of high index PSQ-LH. UV curing was realized from the side of the quartz substrate with an intensity of 30 mW/cm^2 and a duration of 2 minutes. Demolding was realized without specific equipment but with a tweezer. Finally, two steps of thermal curing (2 hours of 160 ˚C and 2 hours of 180 ˚C) were used to fully cure the PSQ-LH film.

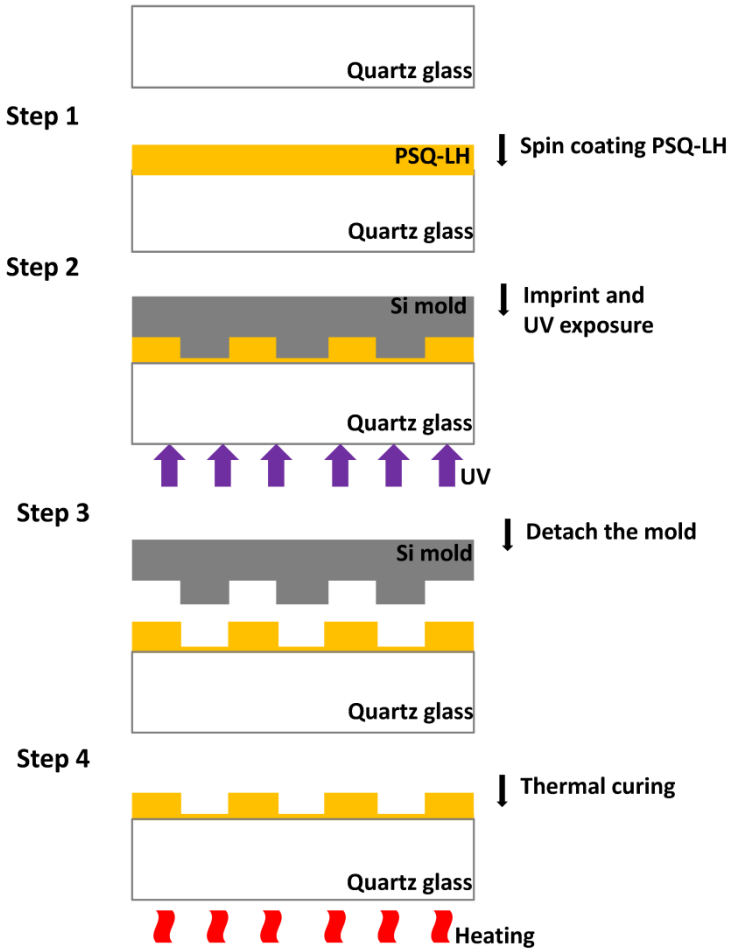

Fig. 3.2 Hard mold imprinting process by using silicon molds and quartz glass substrates.

3.2.2 Existing problems

Although hard mold imprinting and replication has been used to fabricate polymer based photonic devices, currently it still presents several difficulties for us, which will be discussed below.

- *Shallow mold imprinting versus deep mold imprinting*

During experiments, the hard mold imprinting was done and compared with different pattern depths. The results show that shallow mold imprinting and deep mold imprinting exhibit different behaviors. When using a shallow silicon mold with a pattern depth less than 1 μm, the mold can be easily

detached from the substrate in the demolding step. Thus we can achieve good quality pattern transfer. The results are shown in Fig. 3.3. This has also been proved at the end of the previous chapter, where the structures have only 220 nm height. Unfortunately, waveguide modes cannot be supported by structures with such a small height value because of the relatively low refractive index contrast between the quartz substrate (n=1.45) and PSQ-LH (n=1.52). For actual functional devices, the deep mold imprinting with a pattern depth up to 2 μm was carried out. However, the demolding process becomes very difficult because of the strong capillary forces between the mold and the substrate with increasing depth. Even worse is that the waveguide patterns start tending to break, especially for some rounded structures, which is shown in Fig. 3.4. After confirming that our surface energy treatment has no problems, we found that the following explanation is much more reasonable, which is shown in Fig. 3.5. Although the surface treatment of the mold has given rise to a sufficient low surface energy, the polymer PSQ-LH after UV curing still tends to stay in the trench regions of the mold because of the large feature depth. With the not so ideal demolding where the parallelism is poor, such parts can be torn apart from the quartz substrate, making the intact pattern transfer impossible. This problem can only be conquered by improving the parallelism between the mold and the substrate during demolding [8]. The brittle property of the PSQ-Ls material itself is also another reason.

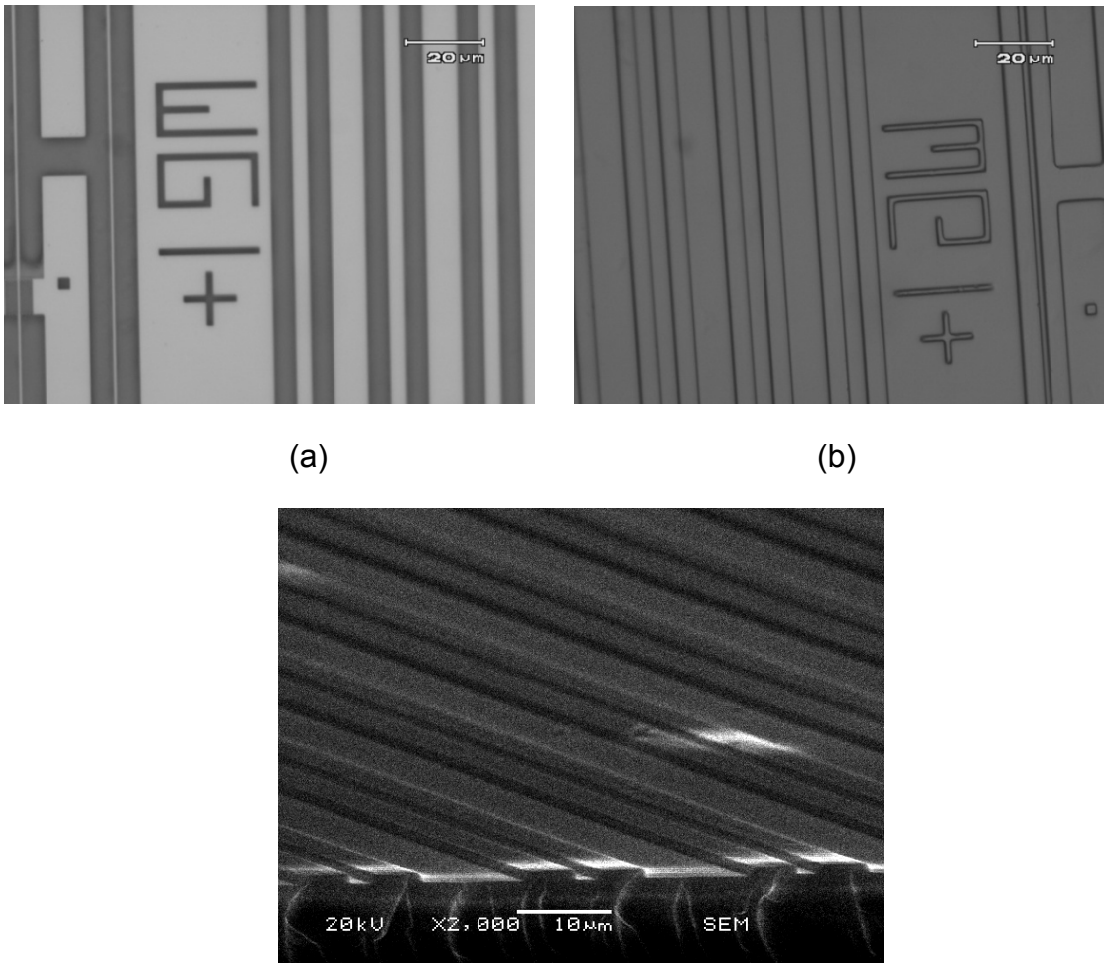

(a) (b)

(c)

Fig. 3.3 The polymer waveguide patterns imprinted by silicon molds with feature depths less than 1 μm. (a) The microscope image of the silicon mold. (b) The microscope image of the replicated polymer patterns. (c) The SEM image of the replicated polymer patterns.

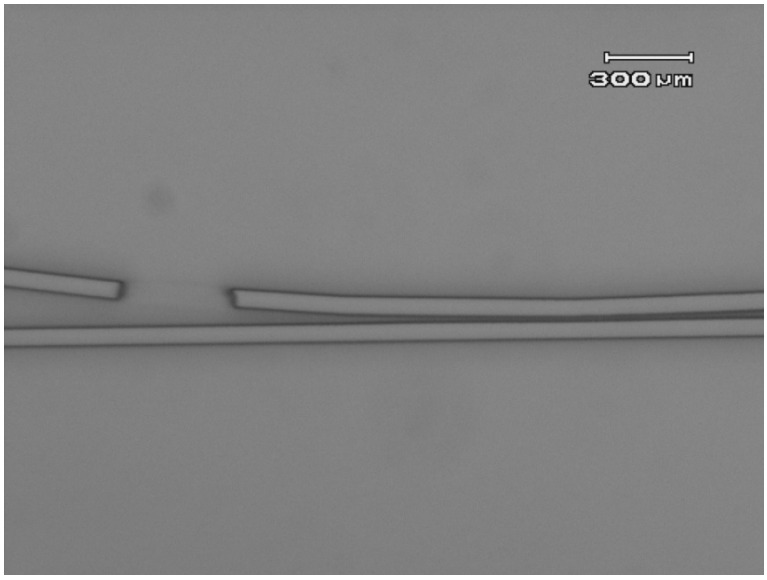

Fig. 3.4 The microscope image of the broken structure caused by the detaching of the silicon mold from the substrate.

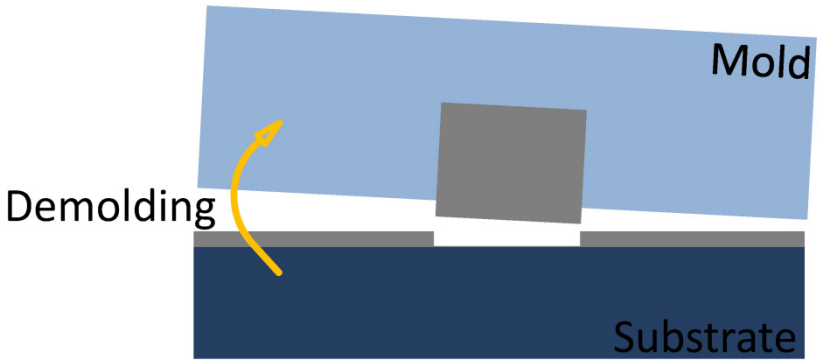

Fig. 3.5 The defects caused by the polymer being torn apart during the demolding process.

- *Deep silicon mold etching with good quality and other issues*

To obtain a mold with high quality is important for hard mold imprinting. Because one of the unique features of micro/nanoimprint is high fidelity, any defect on the mold would result in the defect on the patterned waveguide structures. In our case, we used a silicon mold and a quartz substrate. Alternatively, the quartz mold can be used to imprint on the silicon substrate.

However, neither the silicon mold nor the quartz mold is easy for fabrication, especially when the strict condition of defects-free must be met. The deep etching depth required for replication of polymer waveguides poses another difficulty. Although we paid a lot of effort trying to improve the quality of the silicon mold, within this thesis its quality is still not good enough to satisfy our needs and is still under investigation. Compared with the sidewall roughness, the toughest issue is the always appearing defects here or there. One typical SEM picture is shown in Fig. 3.6. The defects are suspected to be introduced during photo resist patterning, protection mask fabrication or silicon dry etching itself.

Moreover, since the hard mold imprinting is based on physical contact between the mold and the substrate, it is inevitable to induce extra defects during imprinting, because of the reason shown in Fig. 3.5 for example, thus limiting its repeated usage. Besides that, compared with a quartz substrate, a silicon substrate is preferred. The brittle characteristic and lattice orientation of a silicon substrate help to obtain waveguide facets during dicing, while it is difficult to dice a quartz substrate to obtain debris-free facets due to the lack of such lattice orientation.

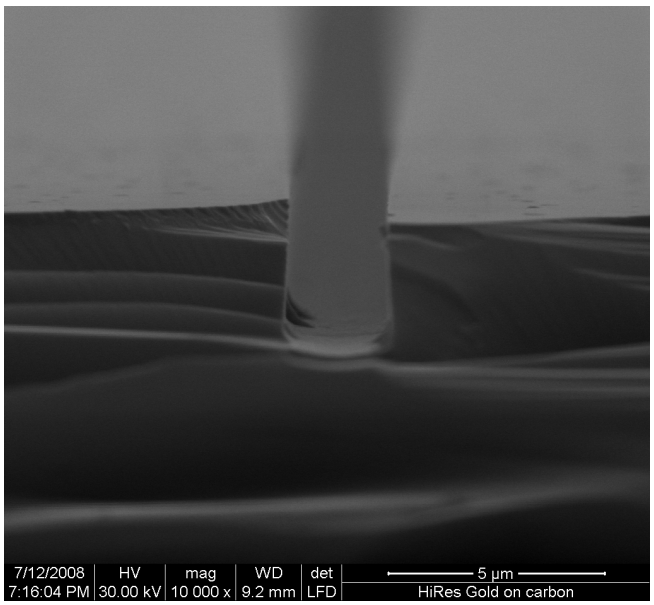

Fig. 3.6 The defects on the silicon master mold which is fabricated by the dry etching.

3.3 **UV-based soft imprint techinique**

From the previous section, it can be seen that the conditions enabling us to implement hard mold imprinting are stringent. Therefore we need to resort to other fabrication methods. Among them, the UV-based soft imprint technique, which utilizes a PDMS (polydimethylsiloxane) soft mold, has been proven to be an effective way to fast process the optical polymer material at low cost [9, 10]. Compared with hard mold imprinting, the advantages of this method can be summed up as:

- There is a wide variety of sources for acquiring the master mold. Some photo resist can play this role very well, thus resorting to fantastic semiconductor crafts is eliminated.
- The mold used directly for polymer imprinting can be repeatedly replicated from a master mold, effectively preventing the master mold from contamination.
- The extremely low surface energy of cured PDMS mold results in low adhesion of it to most optical polymer material, avoiding the sticking induced defects.
- The whole imprint process is simple, with high fidelity, fast and low cost without resorting to expensive imprint equipments. Its soft property allows the imprinting on non-flat substrates.

The UV-based soft imprint technique has been used to fabricate integrated optical devices such as optical couplers, distributed feedback structures, micro-lenses and so on. But there are still some issues that concern us. They are:

- Our polymer PSQ-Ls has the advantage of environmental stability compared with other material, such as acrylate or epoxy based polymer, but its viscosity is high. Whether or not UV-based soft imprinting is compatible with PSQ-Ls needs to be tested.
- Compared with ICP or RIE dry etching which has great chance to cause waveguide surface roughness, this technique has certain

advantage. But to what extent, the surface roughness can be improved remains to be seen.

- Imprinting straight waveguides can be easy. But is it suitable to imprint relatively complicated devices such as microring resonator, which has a very fine coupling structure as well as bent waveguide?

These issues are going to be discussed in the following sections, where three fabrication steps are involved. They are master mold fabrication, PDMS mold replication and UV imprinting.

3.3.1 Master mold fabrication and PDMS mold replication

As mentioned before, the first merit of this technique is a wide variety of mold sources. In our case, negative photo resist SU-8 2 purchased from “MicroChem” company can already perform well. Since it is a kind of photo resist, structure patterns for polymer waveguide devices can be directly obtained by conventional photolithography. For extremely fine structures, e-beam lithography can be used. Any dry etching process is avoided. Besides that, this material is rigid enough, which promises that the defined structures will remain intact during detachment of the replicated mold and master mold. The fabrication details shown in Fig. 3.7 are described below. First, SU-8 2 is spin-coated on the silicon substrate, which has been carefully cleaned, at the speed of 1600 rpm for 40 minutes. This is determined by the experimental film thickness versus spin coating speed curve. Then it is pre-exposure baked on a hotplate to evaporate the solvent at a temperature of 65 ˚C and 95 ˚C consecutively, each for 2 minutes. The exposure is carried out with the contact mask aligner under 400 nm UV light. After that, the same condition as for the pre-exposure bake is used to post-exposure bake the resist film. The exposed part of it is hardened. The photo-defined structures can be acquired by developing the sample in SU-8 developer. Finally, a temperature up to 180 ˚C can be used to fully cure and harden the resist patterns.

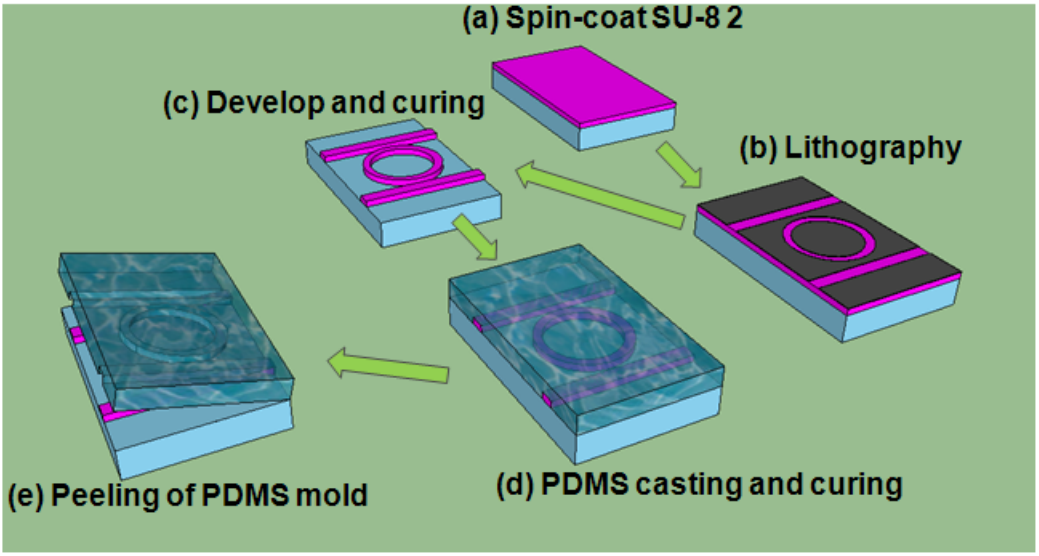

Fig. 3.7 The fabrication process for the SU-8 2 master mold and that for the soft PDMS replicated mold.

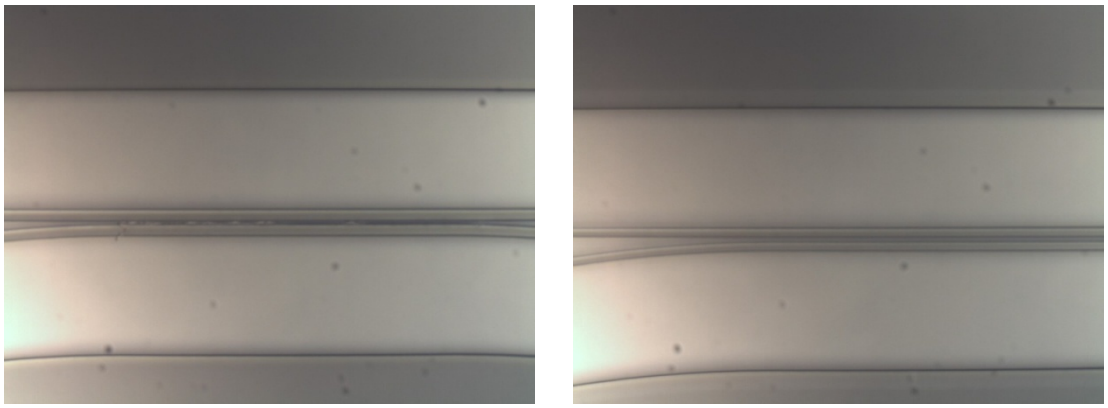

(a) (b)

Fig. 3.8 The resolution comparison of the SU-8 master mold with different exposure times during fabrication. (a) Exposure time of 3 seconds. (b) Exposure time of 2.5 seconds.

Several issues related to the quality of the master mold need to be paid attention to during this process, since they determine the performance of the final devices. The first is the adhesion problem. Vacuum mode on the contact mask aligner is required to ensure the close physical contact between the chrome mask and the SU-8 sample. This is in order to achieve higher

resolution. In theory, the better the contact, the higher the resolution. But also for this reason, part of the SU-8 film easily gets stuck to the chrome mask when the mask holder and the substrate holder separate from each other after the UV exposure, resulting in a defective master mold. The anti-adhesion treatment to the chrome mask can be the solution. The method is similar to that introduced in the hard mold imprint section, but a vapor gaseous treatment is preferred. The second issue is about the resolution. We require a resolution down to 0.8 μm for our finest structure, which is almost at the limit of SU-8 2 photo resist for regular contact lithography. Thus the whole process needs to be strictly controlled, especially the exposure time and development time, which are also close to the extreme. The typical comparison is shown in Fig. 3.8. The only difference between these two samples during processing is the 0.5 seconds exposure time difference. The structure in Fig. 3.8(a) was exposed for 3 seconds and that in Fig. 3.8(b) was 2.5 seconds. Both of the samples were developed for 15 seconds. From this example, the critical dependence of the resolution on the processing can be clearly seen.

For master mold fabrication, another important result is that the molds fabricated in this way provide large flexibility for surface morphology improvement. As we know, cured photo resist has a certain softening point. When it is heated up to this point, the viscosity of the surface becomes reduced and the fluidity is enhanced. As a result the structures can undergo reflow under its surface tensile force. This merit is taken advantage of by us to improve the surface roughness of the master mold, which helps to reduce the surface scattering loss of the final imprinted photonic devices. Fig. 3.9 shows an example of such improvement before and after the thermal reflow. The optimal parameters were found to be 180 ˚C with a duration of 3 minutes on a hotplate, with which the structures' surface roughness is improved but their good rectangular shape is kept. The corner was not rounded obviously. The devices fabricated with these master molds with improved surface quality exhibit good optical performance, which is shown in Section 3.4 of this chapter.

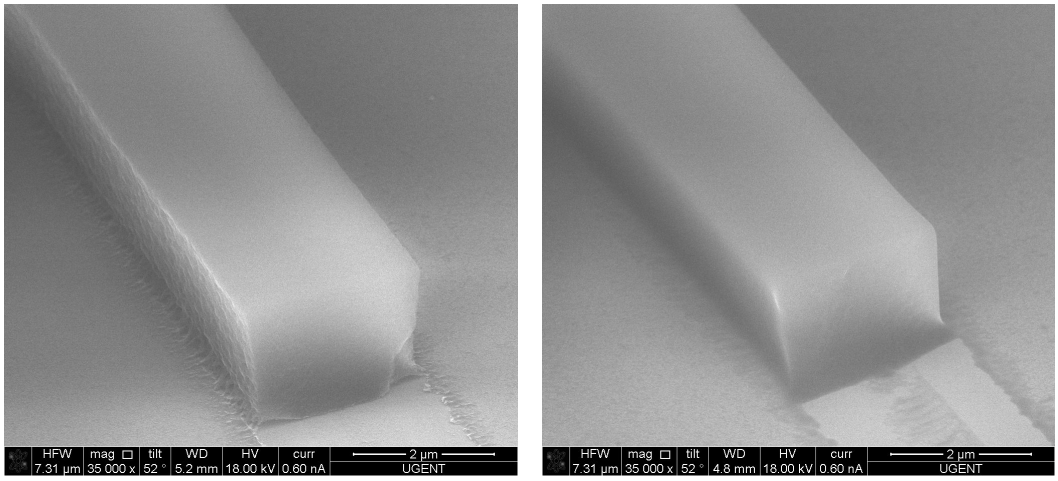

(a) (b)

Fig. 3.9 The reduction of the surface roughness of the master mold (a) before and (b) after the thermal flow treatment.

PDMS (Sylgard 184 purchased from Dow Corning) is used to fabricate soft molds with good transparency of UV light, which we use later to cure PSQ-Ls. Thus in this way PSQ-Ls based photonic devices can be fabricated directly on a silicon substrate. The procedures start with mixing the two liquid components of PDMS, base agent and curing agent, at a ratio of 10:1. After this, the mixture is full of air bubbles and degassing in the dessicator is needed to eliminate them. The mixed PDMS then is poured on top the SU-8 master mold fabricated previously, which is put in a petri dish. Again, after the PDMS covers the whole surface of the master mold, enough time of degassing is required before thermal curing. The curing is performed at 65 ˚C for 2 hours. Although higher temperature can shorten this time, lower temperature is preferred to effectively prevent the shrinkage of the replicated mold. Air bubbles are an important source of extra mold defects within this process thus special attention needs to be paid to them. The thickness of the soft mold is controlled to be 1-2 mm. This process can be repeated to produce several soft molds from one single master mold without causing any apparent degradation of the master mold.

3.3.2 UV-based soft imprint: problem and strategy

- *Normal route of imprinting and meeting obstacle*

After obtaining a good quality mold, we can move on to do the imprinting work. The scheme shown in Fig. 3.10 is briefly described below. First, a layer of PSQ-LL (n=1.45) is spin coated on the cleaned silicon substrate and fully cured with UV light and heating in an oven. It acts as under cladding of the waveguide. After 2 minutes of O_2 plasma treatment, the core layer PSQ-LH (n=1.52) is spin coated on top of the under cladding layer. Then the PDMS soft mold is placed on top to imprint this core layer. During this process, special attention has to be paid to prevent trapping of air bubbles between the mold and the substrate. Because of the softness of the mold, it is easy to make the center area of the mold bow outwards to contact with the core layer first, and then to slowly lower down the remaining part of the imprinting mold. In this way, the trapped air bubbles can be squeezed out along the waveguide pattern, making the waveguide patterns voids free. Around 3 minutes of UV illumination with an intensity of 30 mW/cm^2 in nitrogen atmosphere is used to UV cure the waveguide core layer. The waveguide patterns can be shaped with good conformity to those on the mold, which can be easily detached from the substrate because of the surface hydrophobic property of the mold. Finally, post baking at 180 ˚C for 2 hours and 200 ˚C for another 2 hours allows full polymerization of the waveguide core layer.

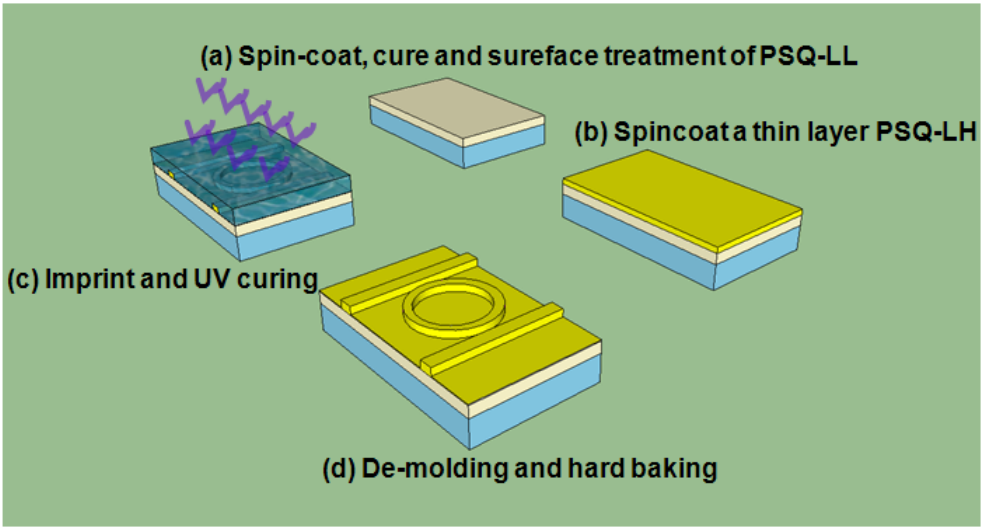

Fig. 3.10 The process of UV-based soft imprint lithography technique to fabricate PSQ-Ls polymer waveguide structures.

The method described above is comparable to the other similar works where UV-NIL is performed with the PDMS transparent mold. One universal but very tough problem in this technique is the residual layer left on the sides of the waveguide after imprinting [11, 12]. Several critical issues such as extra bending loss, waveguide crosstalk and so on would result from this layer, which have a high risk of degrading the total performance of the integrated chips. Some numerical analysis will be given below to illustrate this problem. For our case, this problem is even worse due to the high viscosity of the PSQ-Ls material. One typical imprinting result is shown in Fig. 3.11. The imprinting of the PSQ-LH core layer was carried out on the cured PSQ-LL under cladding layer. The bottom substrate is silicon. It can be seen that besides the desired ridge shaped structure, there is also a thick residual layer underneath it. The thickness of the residual layer has even exceeded the desired ridge height. Such a waveguide structure would encounter many limitations when it is used for designing more complicated devices.

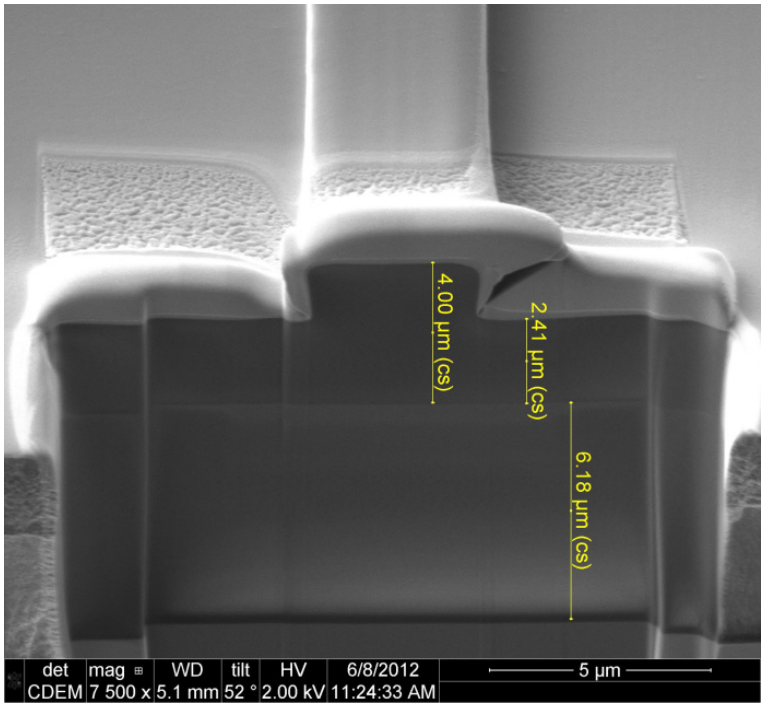

Fig. 3.11 Ridge shaped polymer waveguide structure with thick residual layer fabricated by normal route of soft imprinting.

- Some numeric considerations

Here we consider the influence of the residual layer on two kinds of structures: waveguide bends and waveguide directional couplers. They are also two important elements for the construction of the microring resonators, which are intensively used in this study. The waveguide cross section is defined as the same as that in Fig. 5.3(b) in section 5.2.4, where the waveguide width is 2.3 μm and the waveguide height is 2.1 μm. As water is chosen as the upper cladding, its refractive index is 1.3105. Assuming the bend radius is 250 μm, the relationship between the bend loss and the thickness of the residual layer is plotted in Fig. 3.12. As can been seen, the bend loss stays below 0.04 dB/round when the residual layer is less than 400 nm. However, as a consequence of the weakened lateral confinement, the bend loss would increase dramatically with the further increasing of the thickness of this layer. Too large extra loss can degrade the performance of the microring resonators which are of high loss dependence. Two different

types of waveguide directional couplers, of which the designed coupling ratio are 50:50 and 10:90, are considered. The calculation results are shown in Fig. 3.13. For the waveguide directional couplers with the designed coupling ratio of 50:50, the output coupling ratio would differ significantly from 50:50 with the presence of the residual layer. For 0.1 μm thick residual layer, the output coupling ratio has already changed to 45:55. Compared with that, the waveguide directional couplers with the designed coupling ratio of 10:90 has relatively large tolerance on the variation of residual layer thickness. 0.2 μm thickness change would result in the output coupling ratio of 13:87. Such small coupling ratio change would only have limited influence on the performance of the fabricated microring resonator. More important, 0.2 μm residual layer thickness is well within the control during the fabrication, see below.

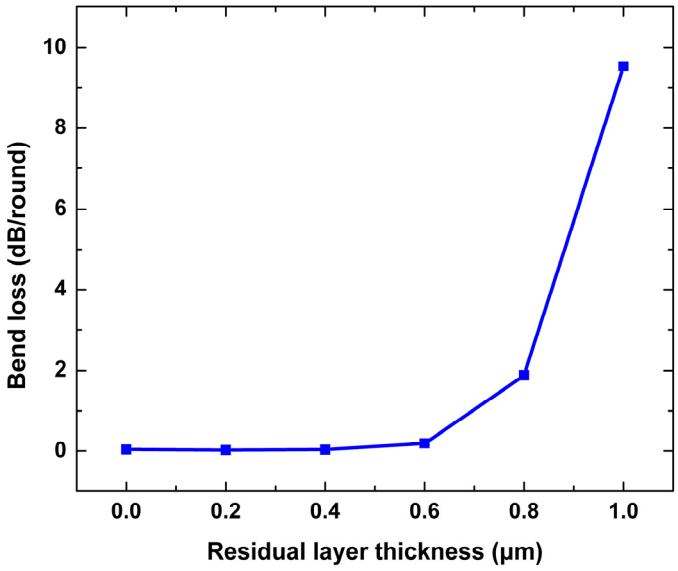

Fig. 3.12 The relationship between the bend loss per round trip and the residual layer thickness.

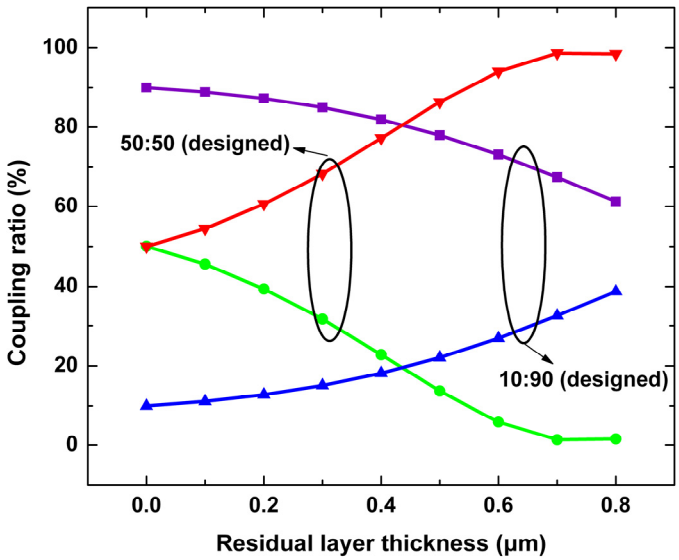

Fig. 3.13 The deviation of the coupling ratio of the directional coupler with the thickness of the residual layer.

- *Unconventional route of imprinting*

Since this UV-based soft imprint technique exhibits great potential for fast prototyping the polymer photonic devices at low cost, a lot of effort was put into solving this residual layer problem. RIE etching to remove it is the most straightforward method. But since such etching is non-selective, the already imprinted structures would also be thinned during this process, causing loss of dimension accuracy. The schematic picture is shown in Fig. 3.14. Moreover, not mentioning the added fabrication cost, the surface roughness problem that has been solved for the master mold fabrication would rise again here. The second approach we tried is adding acetone as a solvent to dilute the imprinted material PSQ-LH. It was proven that after this, PSQ-LH cannot be cured with UV light effectively. Thus both structure imprinting and later demolding became a problem. Even worse, we observed that the PDMS mold swelled to some extent in this solvent during imprint. The pattern transfer fidelity cannot be guaranteed. Being solvent-free is one of the unique advantages of PSQ-Ls series material and should not be abandoned. The other method used extensively in other works such as exerting high pressure

and prolonging the imprinting time was not tried because we lack dedicated imprinting equipment in our lab, which was also rather tedious [13, 14].

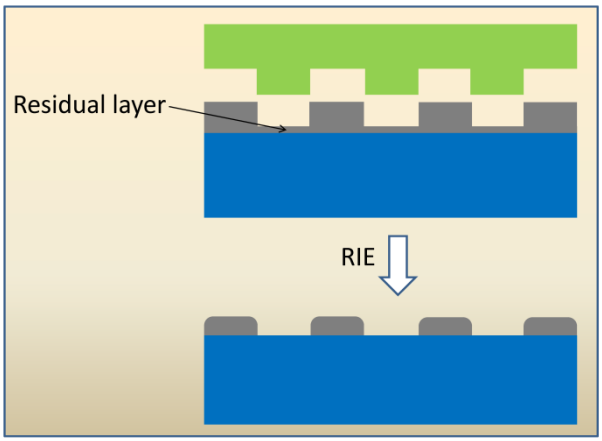

Fig. 3.14 The loss of the polymer waveguide dimension accuracy because of the dry etching carried out after the imprinting process.

- Ridge shaped waveguide imprinting

Polymer-based photonic devices based on ridge shaped waveguides are highly desired in this thesis, especially for the application on label-free biosensing (see chapter 5). Under the current experimental condition, in order to circumvent the residual layer problem, we adopt an innovative “minimum polymer squeezing” method. The ridge shaped waveguide is obtained by imprinting two trenches on both sides of the waveguide, instead of using the single trench pattern on the mold to directly imprint the waveguide in the core layer. A schematic picture is shown in Fig. 3.15. The advantage of this method is that the resistance of the polymer against the mold is low because only a small amount of the polymer needs to be squeezed by the mold. Thus the requirement for the strength of the forces exerted on the mold is greatly minimized. No additional imprinting tool is used during the whole imprinting process, in which the polymer waveguide is patterned only by the capillary forces between the PDMS soft mold and the substrate. A polymer waveguide with good rectangular shape as well as negligible residual layer thickness (below 100 nm) fabricated with this method is shown in Fig. 3.16. A similar

strategy was used by T. Han etc. in [15] to obtain a low loss straight waveguide. Nevertheless, through experiments we found that this technique is not only limited to fabricating straight waveguide, the other devices such as coupler, splitter, ring resonator and so on can also be fabricated in the same way. Essentially, this method shifts the complexity during imprinting to the design of the mask which is used to fabricate the master mold. Considering both the ease of polymer material synthesis and the simple fabrication process, this technique holds the promise for fabricating different kinds of polymer based photonic devices at a very low cost.

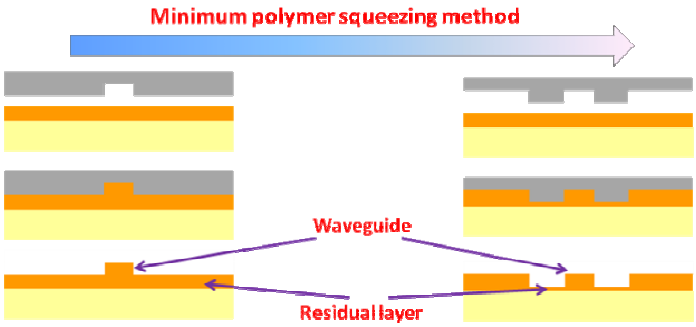

Fig. 3.15 The schematic picture of the “minimum polymer squeezing” method for the reduction of the residual layer on the sides of the ridge shaped waveguide.

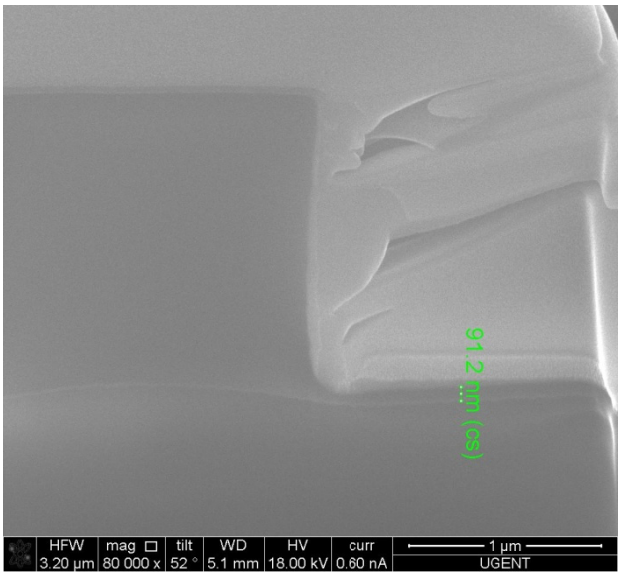

Fig. 3.16 The SEM picture of the fabricated ridge shaped waveguide with negligible residual layer thickness.

- Inverted-rib waveguide imprinting

The fabrication of the passive photonic devices based on polymer benefits from another structure obtained with this technique: the inverted-rib waveguide. The fabrication process is shown in Fig. 3.17. Rather than directly imprinting on the waveguide core layer, the PDMS soft mold with protrusion structures can be imprinted on the uncured under cladding layer. With 3 minutes UV curing of the sample in the nitrogen atmosphere, trench structures can be formed in this layer after the mold is detached. Such trench structures can already be good optical waveguides if another core layer with higher refractive index is spin coated on top to fill them. This method also smartly avoids the residual layer problem because its thickness can be controlled by the spin coating speed of the core layer. High spin coating speed can result in residual layer thickness down to 0.8 μm, which is small enough to prevent its influence on the performances of the devices. From simulation, we can also see this is a buried waveguide structure. The small horizontal refractive index difference helps reduce the waveguide loss effectively. A trench waveguide structure before the spin coating of the core layer is shown in Fig. 3.18.

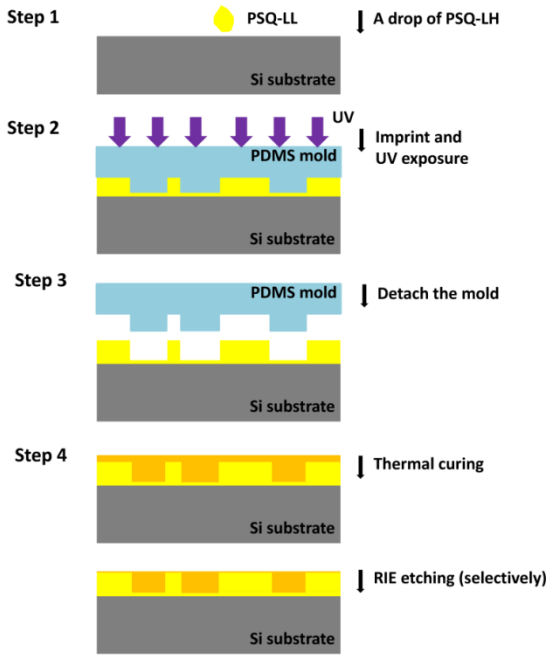

Fig. 3.17 The fabrication process of the inverted-rib polymer waveguide using UV-based soft imprint technique.

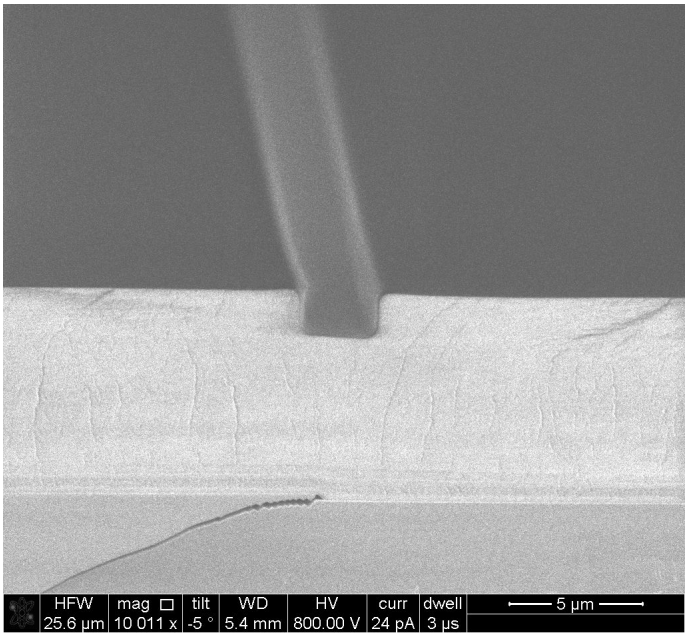

Fig. 3.18 The imprinted trench waveguide structure before the spin coating of the waveguide core layer.

3.4 **Characterization of the fabricated devices**

Several fabricated devices are measured and characterized, which include straight waveguides, Y splitters, notch filters, microring resonators. The measurement results will be presented and discussed.

3.4.1 Measurement setup

For the characterization of polymer based photonic devices, normally the horizontal setup is used. The schematic picture is shown in Fig. 3.19. Light from a tunable laser source is launched into the device under test through a lensed fiber. In order to adjust the polarization state, a polarization rotator is inserted between the tunable laser and the lensed fiber. The output light of the device is collected by an objective and then detected by a photo detector. A polarizer inserted between the objective and the detector is necessary in order to tell the polarization state. For practical applications, some changes should be made to this layout. For example, the tunable laser and power meter can be replaced by an SLED (super-luminescent light-emitting diode), and an OSA

(optical spectrum analyser) respectively for investigating the broad band properties of the device. However, when the studied device has a narrow spectrum, a tunable laser with step resolution down to 2 pm is needed. A power meter with microwatt, picowatt or femtowatt sensitivity is chosen depending on the output power value.

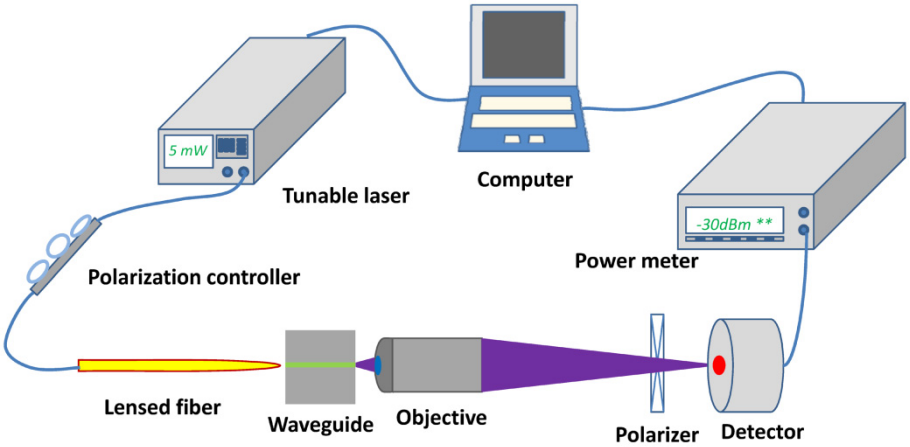

Fig. 3.19 The scheme picture of the measurement setup.

3.4.2 Straight waveguides

The propagation loss of the fabricated straight waveguide is characterized for the TE mode using the so called “cut-back” method. The straight waveguide has a ridge shaped structure, with air as the upper cladding. The waveguide width and height are 2.5 μm and 2.1 μm respectively. First, the input light is carefully tuned to the TE mode using the polarization controller and polarizer. Then the straight waveguides of different lengths are inserted between the lensed fiber and the objective. The obtained insertion loss values for each waveguide length are fitted with a linear function, of which the slope can represent the waveguide propagation loss. Keeping the coupling condition the same for each waveguide measurement is critical for this experiment. The result is shown in Fig. 3.20, from which the propagation loss is estimated to be 2.589 dB/cm. Good linearity also indicates the validity of the measurement. Assuming the substrate leakage loss is negligible, a scattering loss of around 1.6dB/cm is obtained by subtracting the 0.9 dB/cm material absorption loss.

Compared with the 0.8 dB/cm scattering loss measured by J. Teng with the Fabry-Perot resonance method [16], our loss is reasonably higher because the waveguide of J. Teng is with buried structure. Small horizontal refractive index difference results in lower surface roughness loss.

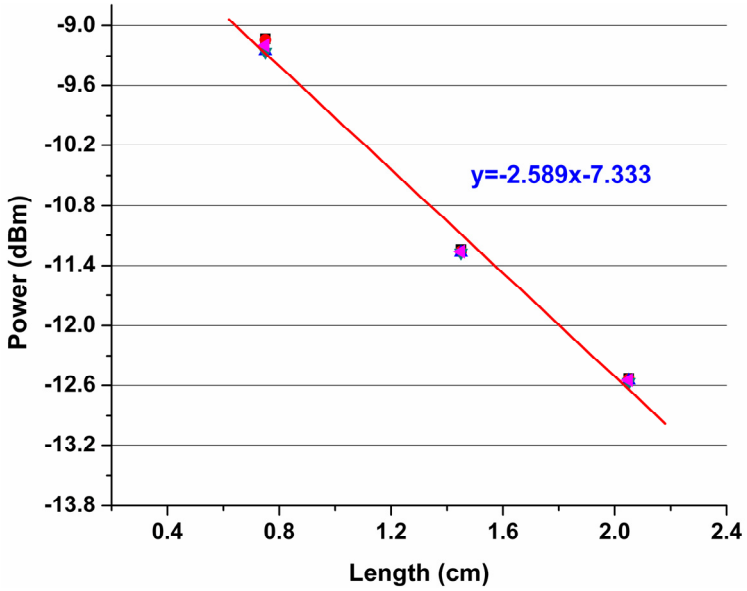

Fig. 3.20 The measurement result for ridge shaped PSQ-Ls polymer waveguide using the cut-back method.

3.4.3 Optical power splitter

Optical power splitters are basic but very important components for splitting and combining the optical signals. Recently, there is a strong demand for these components, especially for fiber-to-the-home (FTTH) [17, 18]. The developed UV-based soft imprint technique was also used to fabricate these devices, which is shown in Fig. 3.21. The inverted-rib structure was adopted due to its low waveguide loss and easy fabrication. The power splitter consists of four parts, which are input waveguide, tapered region, two S-bend waveguides and output waveguides. The distance of the output waveguides is designed to be 250 μm. The measured spectral responses of two output ports are shown in Fig. 3.22. They are normalized by a next reference waveguide which also has S-bend structure. The measurement range is between 1530 nm and 1570 nm, limited by the bandwidth of the SLED source. As can be

seen, the uniformity of the fabricated power splitter is good. Around 4 dB insertion loss is estimated to be mainly caused by the scattering losses at the junction. Improvements can also be made on further reducing the polymer material loss and shortening the length of the device.

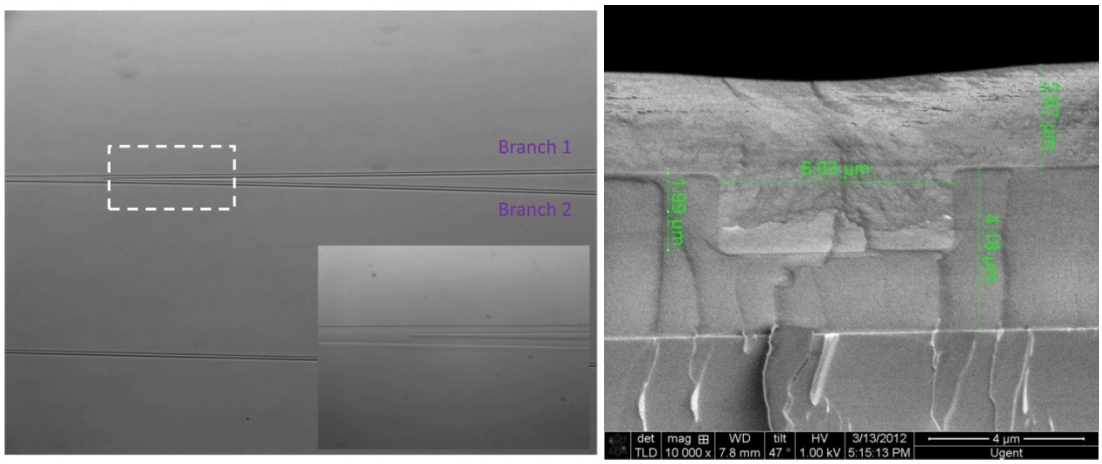

Fig. 3.21 The image of the fabricated power spltter. (a) Top image. (b) Waveguide cross section.

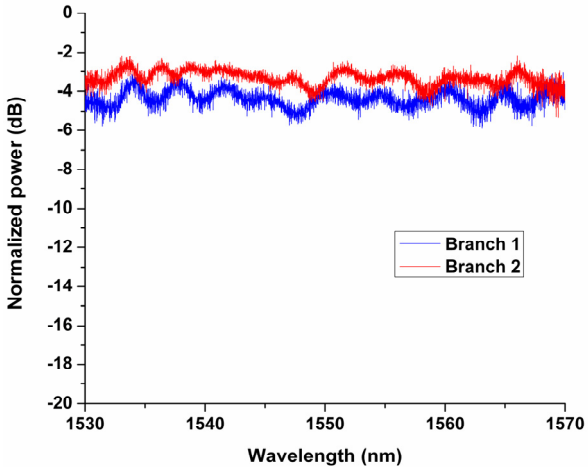

Fig. 3.22 The measured spectral responses of two output ports of the power splitter, which is normalized to a reference waveguide.

3.4.4 Microring notch filter

When a ring structure is placed closely and is evanescently coupled with one straight waveguide, they together constitute an important kind of device called

"microring notch filter" [19, 20]. Its comb-shaped transmission spectrum can be used to remove an undesired signal, of which the application will be discussed in Chapter 4. However, in order to obtain a good performance of this device, a strict condition named "critical coupling condition" has to be satisfied. From the coupled mode theory, it can be deduced as $\alpha^2 = t^2$, where t^2 represents the power transmission coefficient, α^2 represents the total loss per round trip in percentage, which is determined by the waveguide material loss, the bend loss and the surface scattering loss. If α^2 is assumed to be

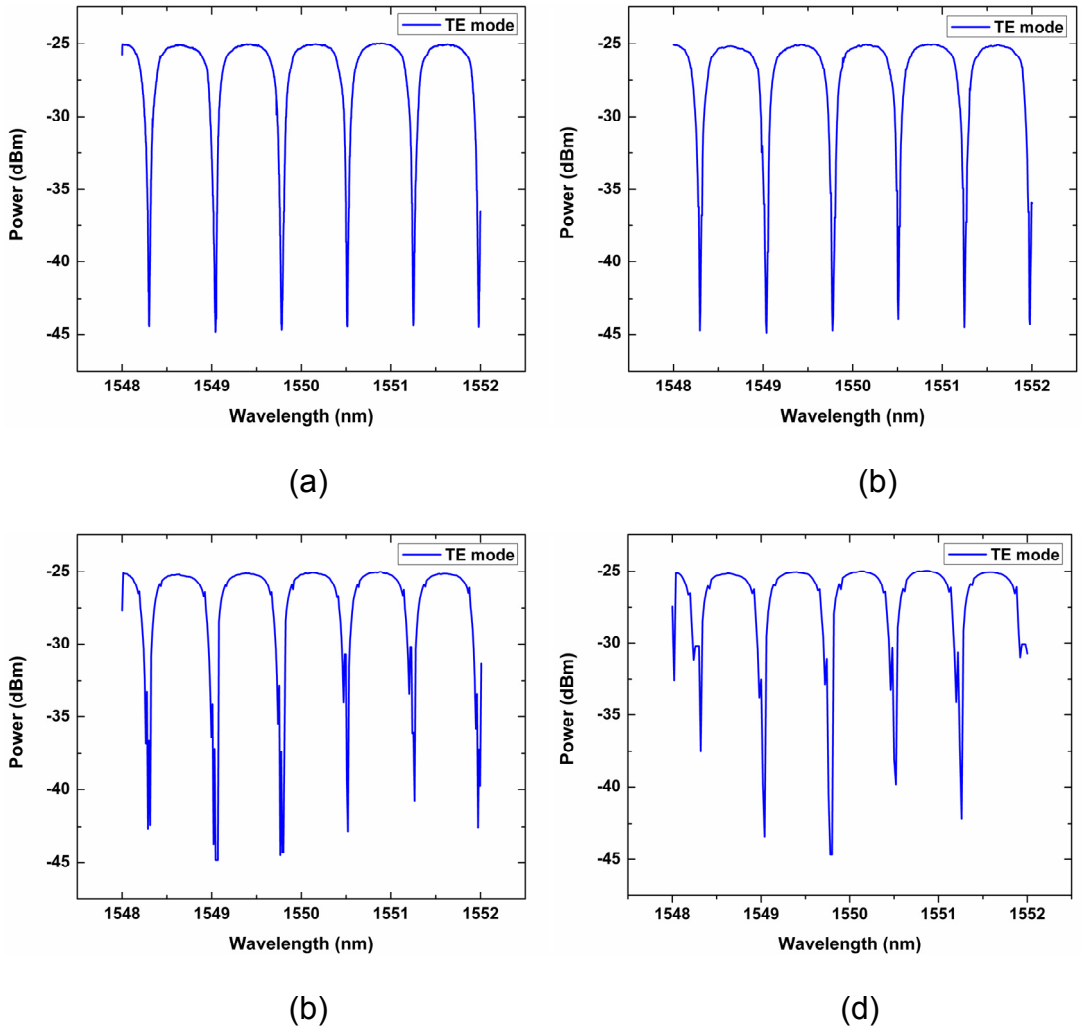

Fig. 3.23 Measurement results for PSQ-Ls polymer microring notch filter with different wavelength resolutions. (a) 2 pm. (b) 6 pm. (c) 12 pm. (d) 20 pm.

constant, there are two ways to achieve that condition. One is changing the gap between the ring and the straight waveguide. The other is by tuning the

coupling length between these two using racetrack structures. We adopted the latter. For the TE mode, with a ring radius of 300 μm, the optimal coupling length was found to be 120 μm for a gap of 0.8 μm. Up to 20 dB extinction ratio was achieved (See Fig. 3.23(a)), indicating that the critical coupling condition is essentially satisfied. This example also reflects the capability of strict dimension control of our UV based soft imprint technique.

Because this device has a very fine spectrum, in order to resolve it, special attention needs to be paid on the sweeping step of the tunable laser. This comparison is shown in Fig. 3.23, where the sweeping steps are 2 pm, 6 pm, 12 pm, 20 pm respectively. It can be seen that 2 pm resolution gives the most uniform spectrum over the measurement range. With the decrease of the measurement resolution, the obtained filtering spectrum becomes more non-uniform and deteriorated.

3.4.5 Racetrack microring resonator

Based on the notch filter introduced in the previous section, another straight waveguide which is side coupled to the ring can be added. Such a so-called “add-drop filter” allows adding, combing and routing of signals, and is not only limited to filtering. Due to this, it has found many applications in switching, (de-)multiplexing, sensing and so on. We also fabricated this device with our proposed imprinting method. Because all the consisted waveguides are with air cladding, a small transformation of the ring structure into a racetrack is made as well in order to increase the coupling. The SEM images are shown in Fig. 3.24. Referring to the characterization, two important results that depend critically on the fabrication will be discussed below.

The first important result we obtained is the obvious improvement of the Q value (quality factor) of the microring resonator. There have been many similar works on fabricating a polymer-based microring resonator. However, efforts of increasing the Q-value easily met a bottleneck due to either the high intrinsic material absorption loss (e.g. SU-8 [21], BCB [22], PMMA [23]), or the not so perfect fabrication method (e.g. ICP or RIE). Thus the achieved Q value is always limited to several thousands or a little bit more than ten

thousands. For our work, taking advantage of the UV based soft imprint technique and the low loss of PSQ series material, we can easily achieve a Q-value around 3×10^4. This is further improved by the thermal reflow technique used in Section 3.3.1 to improve the quality of the master mold. With the reduction of surface scattering loss of the ring, a Q-value as high as 5×10^4 is achieved. The measurement results are shown in Fig. 3.25.

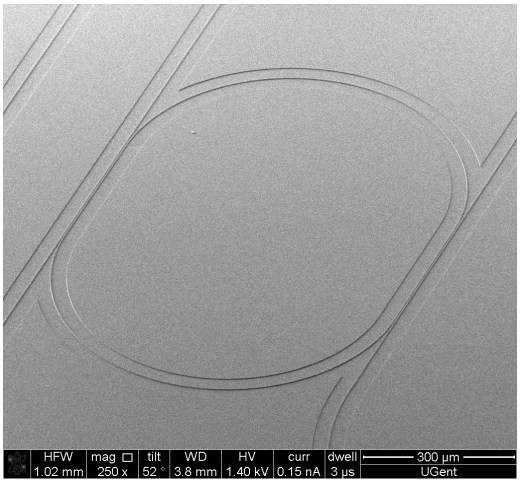

(a)

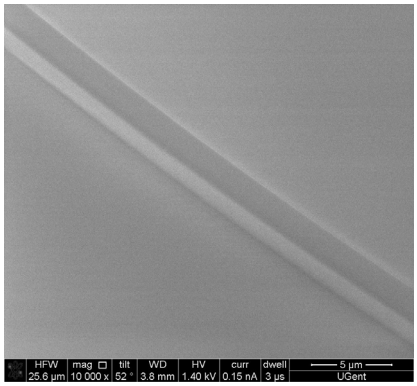

(b)

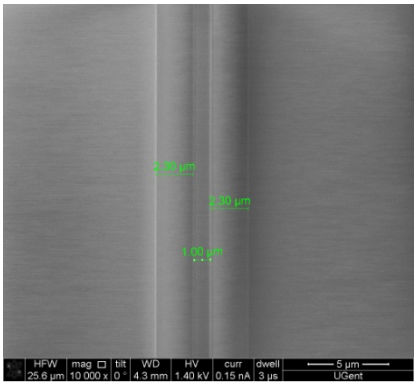

(c)

Fig. 3.24 SEM pictures of the ring resonator fabricated by UV based soft imprint lithography technique. (a) Image of the entire structure (b) Port waveguide (c) Detail of the coupling region.

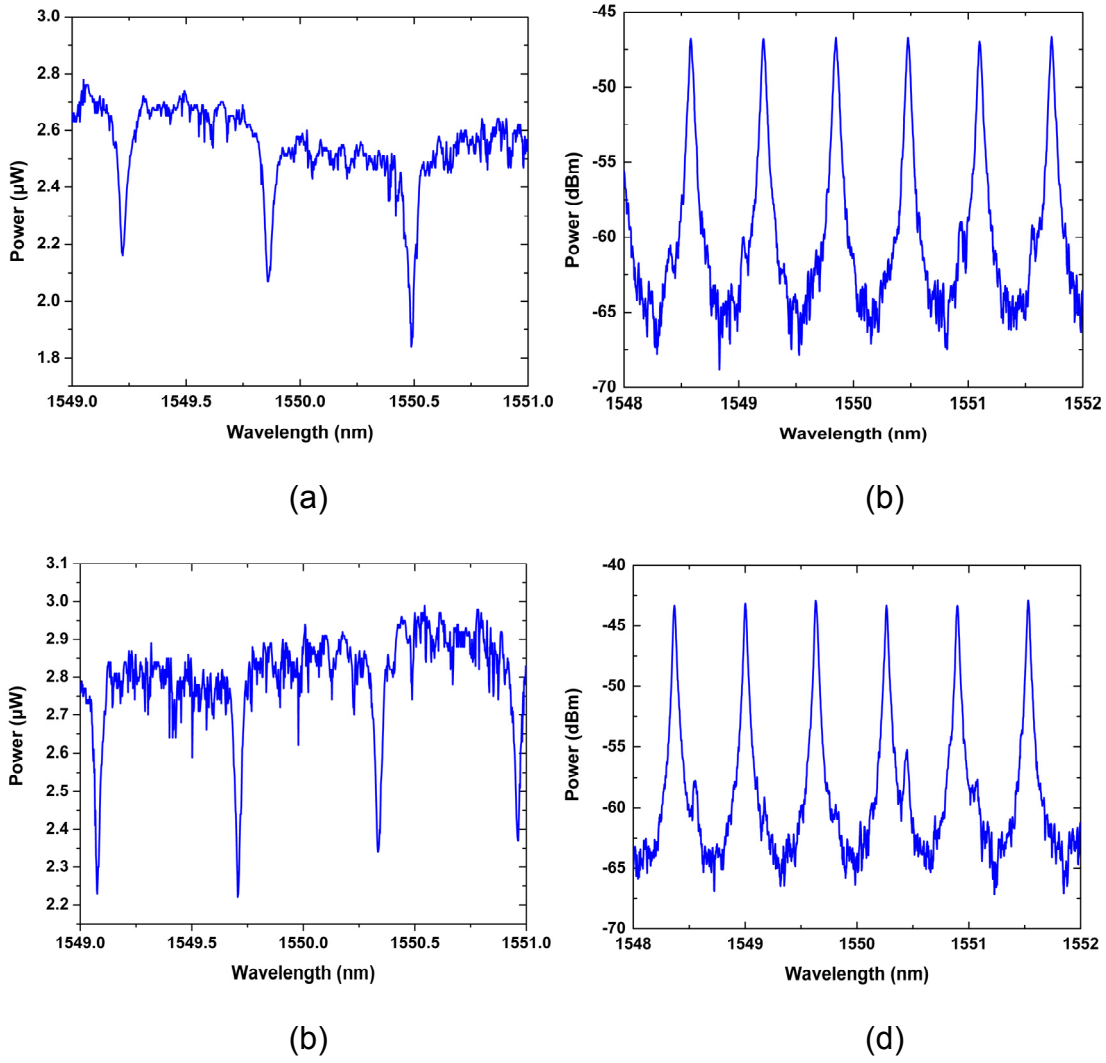

Fig. 3.25 Measurement results for PSQ-Ls polymer microring resonator with different polarization states. (a) TE mode at through port. (b) TE mode at drop port. (c) TM mode at through port. (d) TM mode at drop port.

Sometimes reducing the size of the microring resonator appropriately according to its application is required. By doing this, the FSR (free-spectrum-range) can be enlarged properly, making it more convenient to be used. At the beginning of our work, this task was difficult because we could only realize microring resonators with inverted-rib structure. Although it also had good filtering property, the weak lateral confinement resulting from relatively low refractive index contrast between the waveguide core (PSQ-LH, n=1.52) and cladding (PSQ-LL, n=1.45) prevented us from further reducing its size, where

the radius of the ring is limited to around 400 μm. Since the fabrication of ridge shaped waveguide with an air cladding was achieved, the lateral

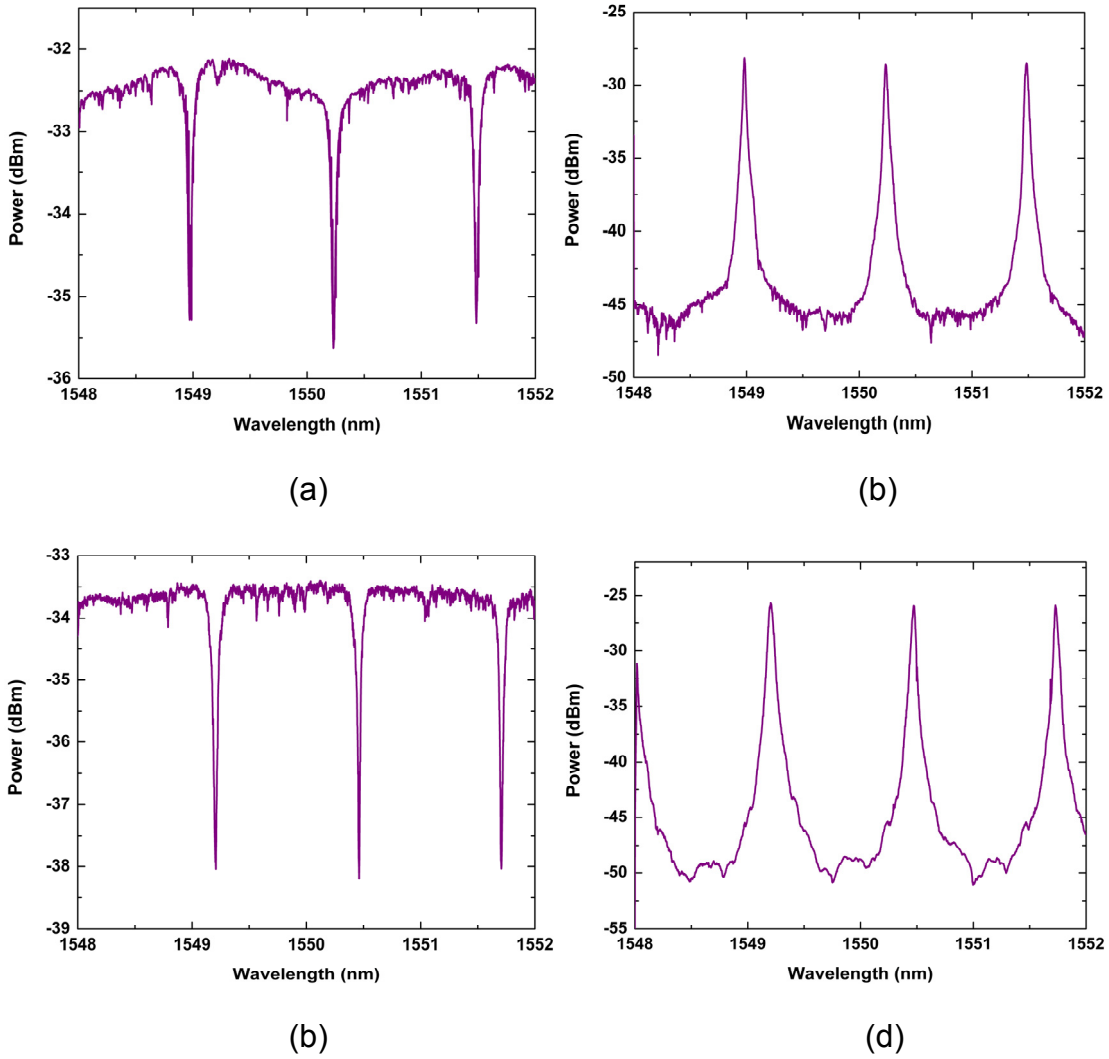

Fig. 3.26 Measurement results for PSQ-Ls polymer microring resonator with small radius under different polarization states. (a) TE mode at through port. (b) TE mode at drop port. (c) TM mode at through port. (d) TM mode at drop port.

refractive index contrast has increased to 0.52 between waveguide core and air. So it would be interesting to see to what extent we can reduce the size of the ring. The result would also prove the usefulness of the efforts we pay for reducing the residual layer. Fig. 3.26 gives the measurement results for the PSQ-Ls based microring resonator with a radius of 150 μm. The FSR is

increased to 1.252 nm compared with our previous work while no degradation of the performances is observed. From this result, it can be concluded that no significant bending loss can arise from the residual layer, which has been reduced to a very thin level during the imprinting process. Further efforts can be made on the under cladding to realize a waveguide structure with nearly all-air cladding. In that case, the size of the ring can even be reduced to the same scale as that in semiconductor (e.g. SOI).

3.5 Mach-Zencher interferometer (MZI) based tunable ring resonator

Several passive devices have been successfully obtained with the UV-based soft imprint technique. However, in some applications, certain tunability of the device is desired [24, 25]. For example, in Local Area Networks (LAN) and home networks, a tunable filter can give services management of the network much more flexibility. Although the microring notch filter introduced before is a kind of good filter, it has no tunability. Moreover, the critical coupling condition is hardly to be met, which imposes extra difficulties on fabrication. In this section, a tunable coupler with a Mach-Zencher interferometer (MZI) is introduced into the ring resonator. Micro thermal heaters are used to tune the equivalent MZI coupler with low power consumption, taking advantage of the high thermal-optical coefficient of polymer. Three coupling states, over-, critical- and under-coupling, of the ring resonator are realized. The tunability of notched resonant wavelengths is also realized with the thermo-optical phase shifter on the waveguide ring.

3.5.1 Layout design and waveguide structure

The layout design for the tunable ring resonator is shown in Fig. 3.27, with electrode loaded polymer waveguide cross section in Fig. 3.28. An MZI consisting of two 3 dB directional couplers is used as tunable coupler for the ring resonator, while the ring resonator itself is constructed by connecting one input port and one output port of the MZI. The lengths of the two arms of the MZI are equal. One micro heater is placed on one of them. The change of the

phase relationship between the two arms through the thermal effect can result in a difference of the light coupling into the ring resonator, thus achieving the tunability of the coupling efficiency. Another micro heater is placed on the ring waveguide. The resonant wavelength position control can be realized with this phase shifter.

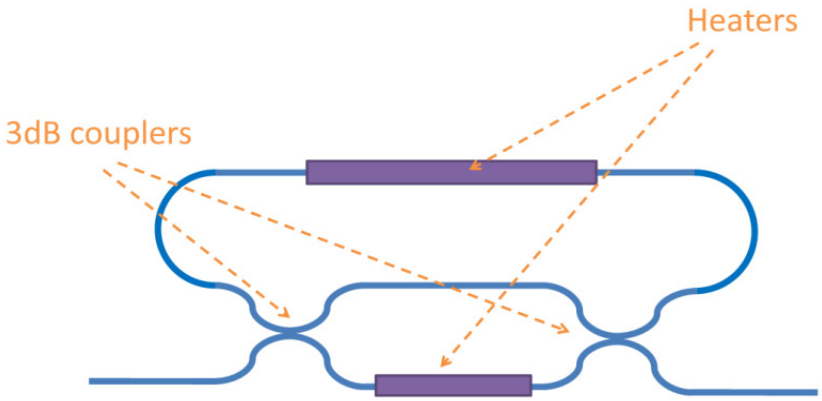

Fig. 3.27 The design layout for the tunable ring resonator.

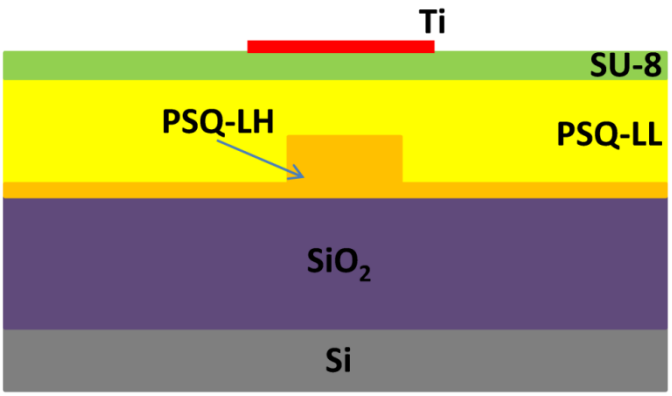

Fig. 3.28 The cross section of the electrode loaded polymer waveguide.

Unlike previous structures with air cladding, an upper cladding is required for the waveguide, on which the micro-heaters can be fabricated. The heat generated by the micro-heater can be efficiently utilized without causing extra loss for the waveguide under the condition that the thickness of the upper cladding is appropriately controlled.

3.5.2 Fabrication of the device

As this is the first attempt of fabricating micro-heaters on optical waveguides with the self-developed polymer material PSQ-Ls, several technical problems had come across during experiments, which are mainly due to the thermal and chemical stability of the material, rather than its optical properties. These problems made the work of loading the micro-heaters complicated.

The device fabrication process is shown in Fig. 3.29. The waveguide fabrication processes are the same as introduced before. Briefly, a SiO_2 layer with a thickness of 6 μm is deposited on top of the silicon substrate by PECVD, which acts as the under cladding of the waveguide. MZI and ring waveguide structures are obtained with one step imprinting of the PDMS soft mold on the thin layer of PSQ-LH. The sample is then baked for 2 hours at a temperature of 180 ˚C to fully cure the waveguide core layer. 4.5 μm PSQ-LL layer is spin coated on top and cured as upper cladding.

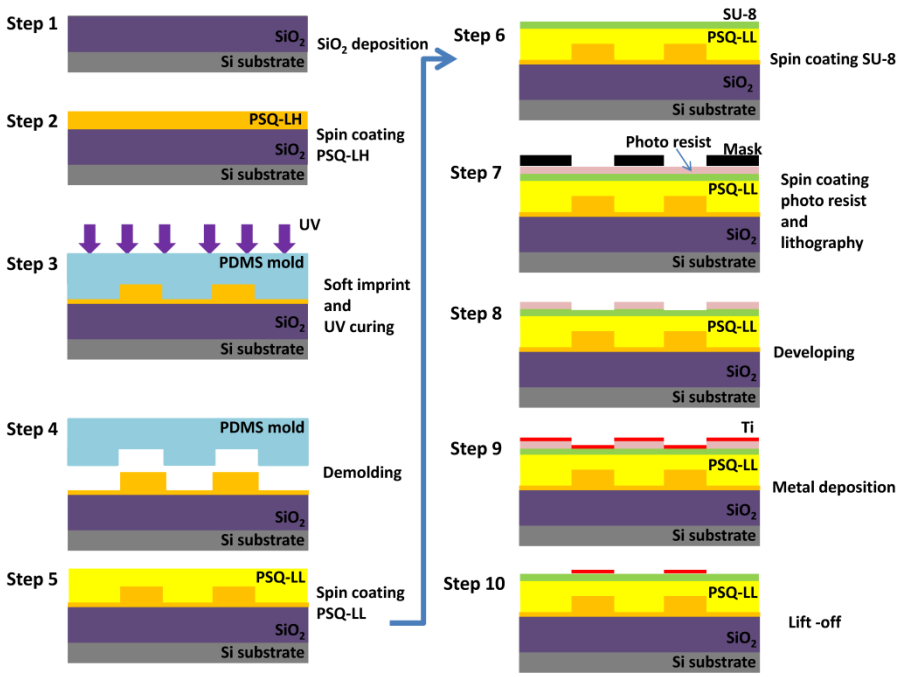

Fig. 3.29 The fabrication process for the MZI tunable ring resonator.

In most cases, polymer PSQ-LL under cladding is preferred as it dramatically reduces the cost of the device. However, here it has to be

replaced with deposited SiO_2, whose refractive index is close to that of PSQ-LL. The reason is that the three layers of PSQ-Ls, which include PSQ-LL under cladding, PSQ-LH core layer and PSQ-LL upper cladding, always tend to crack during the curing process. This is shown in Fig. 3.30. As can be seen, the PSQ-LL under cladding layer would undergo three cycles of long time thermal curing, which is up to 200 ˚C. Strong internal stress between layers will be built during this process. The under cladding layer cracks when such stress accumulates to a certain degree. The effort of extending annealing time to as long as three hours, which is the limit of our thermal curing equipment, also failed to prevent such crack happening.

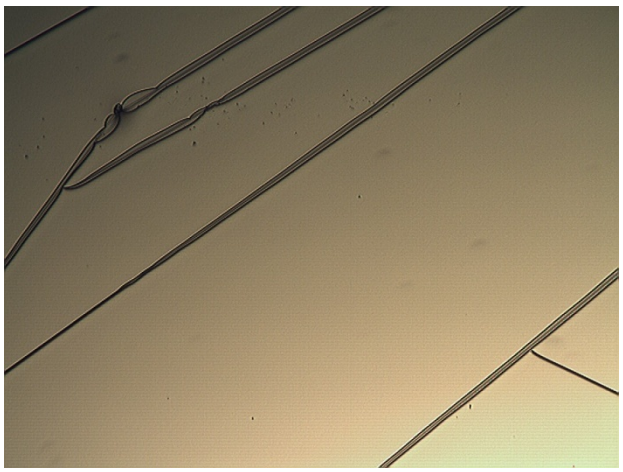

Fig. 3.30 The cracking of three layers of PSQ-Ls polymer during the curing process.

Lift-off process has been proved to be an ideal candidate for the fabrication of the micro heaters. However, currently it is still difficult for PSQ series material to undergo lift-off process. The main problem is that it has a weak resistance to the attack of many solvents used during this process. Photo lithography and dry etching can be used to define the micro heaters, but this will counteract the benefit of the UV imprinting process, which is rather simple and of low cost. In order to circumvent this problem, a thin SU-8 protecting layer with thickness of 1 μm is added on top of the upper cladding of PSQ-LL. By experiment, it was found not only to have very good adhesion

with the deposited mental, but more important, it is quite stable during the whole process of lift-off, protecting well the already fabricated waveguides structures underneath. The lift-off process is shown from step 6 to step 10 in Fig. 3.29. Pattern definition of heaters was achieved with positive photo resist AZ5214, after which titanium with a thickness of 110 nm was deposited. The metal lift-off process was finally realized by immerging the sample into acetone for 1 hour. The microscope images of the fabricated devices are show in Fig. 3.31.

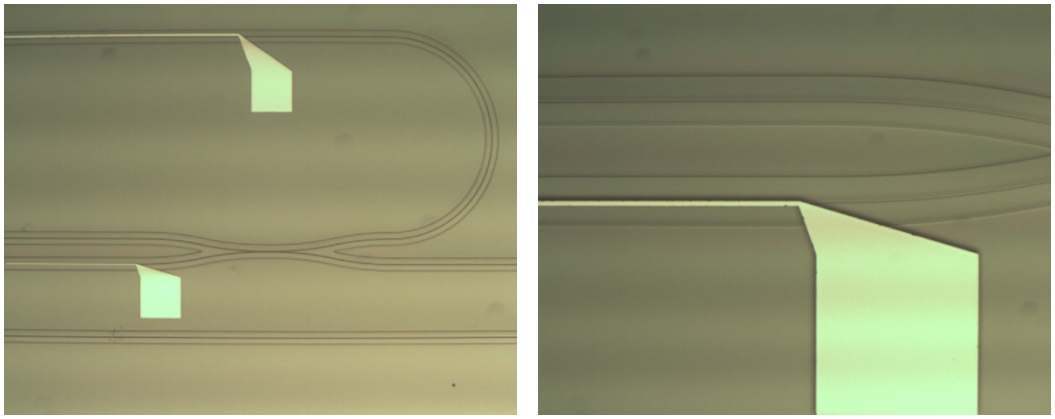

(a) (b)

Fig. 3.31 The microscope images of the fabricated tunable ring resonator. (a) Two heaters with part of the ring and M-Z structures. (b) Alignment detail between the heater and the waveguide.

3.5.3 Measurement results

Electrical power is loaded onto the fabricated device through four micro-needles, the head size of which are 12 μm. In order to measure the transmission of the device, the light from a tunable laser is launched into the input waveguide via a lensed fiber. Its polarization state was tuned to TE with a polarization controller to prevent extra loss. The output light is received by a cleaved single-mode fiber, which is connected to a power meter.

The resistance of two heaters, one on the arm of the MZI and the other on the ring resonator, are first obtained by measuring their voltage-current

relationship. The result is shown in Fig. 3.32. With linear fitting, a resistance value of 2.4471 kΩ for the MZI micro-heater and of 2.5674 kΩ for the micro-heater of the ring resonator, can be concluded respectively. Due to the length, the latter is a little bit larger than the former, although it has a large width.

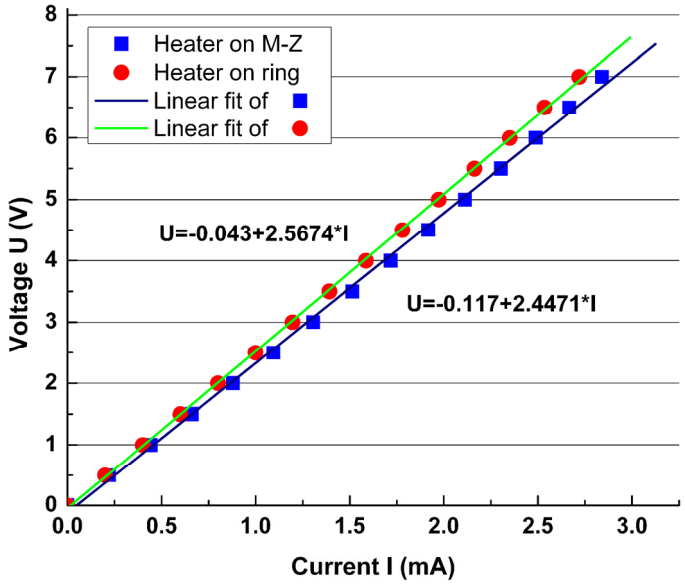

Fig. 3.32 The voltage-current curves of the two heaters and the fitting results for their resistances.

Different coupling states are realized by applying the power only to the micro-heater on the MZI arm. The result is shown in Fig. 3.33. As can be seen, not only the bandwidth, but also the extinction ratio of the filter can be changed according to the applied voltages. At first, the ring resonator is working under the regime of over-coupling as most of the light in the input waveguide is coupled into the ring resonator after passing the MZI. Although in theory there should be no resonance under zero voltage, a shallow dip around 1 dB is observed. This is because the two fabricated directional couplers constituting the MZI are not strictly 3 dB. The light coupled into the ring resonator is decreased with the increasing of the applied voltage. When this coupled energy equals with the roundtrip loss of the ring, e.g. critical coupling condition is met, the highest extinction ratio and narrowest bandwidth

of the filter can be obtained. The continued increasing voltage will make the ring working under under-coupling regime. It is noted that such effective coupling efficiency tuning during this process generates an additional phase shift to the ring resonator, which result in small resonant wavelength shift. This has been analyzed in detail in [26].

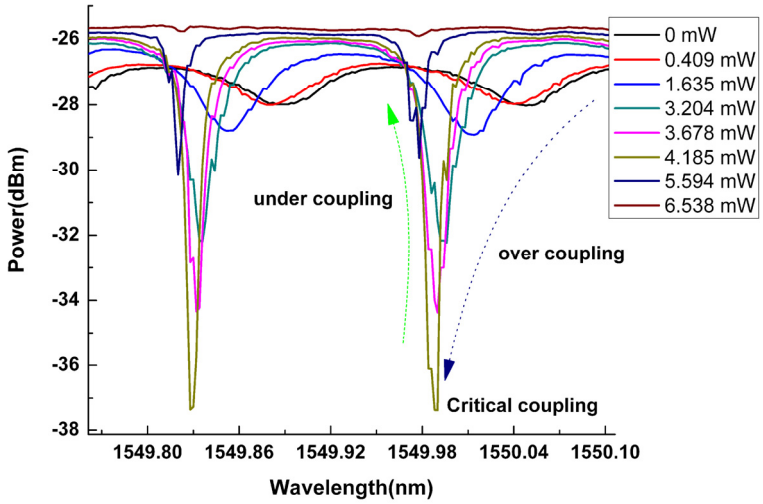

Fig. 3.33 The measurement results of the tunable ring resonator when the power is applied only onto the micro-heater loaded on the MZI arm.

The resonant frequency of the fabricated tunable filter can also be tuned. This is realized by applying the voltage to the micro-heater on the ring waveguide. The voltage applied on the micro-heater of the arm of MZI should be kept at the value where desired bandwidth and extinction ratio are achieved. Here it is demonstrated with the one that critical coupling condition is met, which is 3.2 V. The measurement result is shown in Fig. 3.34. As can be seen, the resonant frequency can be tuned freely within the FSR (free-spectrum-range) of the ring resonator, which is around 0.16 nm (~ 20 GHz).

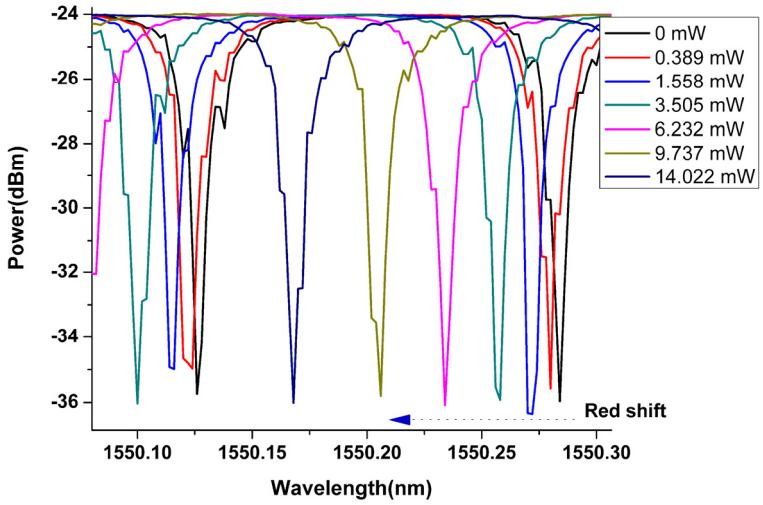

Fig. 3.34 The measurement results of the tunable ring resonator when the power is applied onto both the micro-heaters, which are loaded on the MZI arm and ring, respectively.

3.6 **Conclusion**

In this chapter, the advantages of nanoimprint technology on fabricating polymer waveguides devices are discussed. Compared with traditional semiconductor method, this technique can be used to fabricate polymer waveguides and devices with high quality and performance in a much more fast and efficient way. The details of the fabrication process as well as the strategies to overcome some critical problems during this process are presented and discussed. Different kind of the devices, which include straight waveguide, splitter, microring notch filter, racetrack microring resonator and MZI-based tunable ring resonator, are measured and characterized. With their good performance, they have the potential to find the applications on optical communication and sensing, which will be discussed in the following chapters.

3.7 **Reference**

[1] Jie Teng, “Fabrication of PSQ-L polymer photonic devices,” Ghent University, PhD thesis, Ghent, Belgium (2010).

[2] S. K. Pani, C. C. Wong, K. Sudharsanam, C. S. Premachandran, and M. K. Iyer, “Evolution of sidewall roughness during reactive-ion etching of polymer waveguides,” J. Vac. Sci. Technol. B 24, 163-169 (2006).

[3] S. W. Kwon, D. H. Yoon, W. S. Yang, H. M. Lee, W. K. Kim, and H-Y. Lee, and G. S. Son, "Surface Etching Properties of a Thermally Curable Polymer Based on Fluorinated Polyether for Polymer Waveguide Biosensor Applications," J. Korean Phys. Soc. 55, 1808-1812 (2009).

[4] Erwin Bosman, “Integration of Optical Interconnections and Optoelectronic Components in Flexible Substrates,” PhD thesis, Ghent University, Ghent, Belgium (2010).

[5] Shefiu Zakariyah, “Laser ablation for polymer waveguide fabrication,” PhD thesis, Loughborough University, Leicestershire, UK (2012).

[6] X. D. Huang, X. Cheng, L. J. Guo, S. W. Pang, and A. F. Yee, “Reversal imprinting by transferring polymer from mold to substrate,” J. Vac. Sci. Technol. B 20, 2872-2876 (2002).

[7] N. Kehagias, M. Zelsmann, and C. M. S. Torres, “Three-dimensional polymer structures fabricated by reversal ultraviolet-curing imprint lithography,” J. Vac. Sci. Technol. B 23, 2954-2957 (2005).

[8] C.-Y. Chao and L. Jay Guo, "Polymer microring resonators fabricated by nanoimprint technique," J. Vac. Sci. Technol. B 20, 2862-2866 (2002).

[9] W. C. Chuang, C. T. Ho, and W. C. Chang, "Fabrication of polymer waveguides by a replication method," Appl. Opt. 45, 8304-8307 (2006).

[10] Y. Y. Huang, G. T. Paloczi, A. Yariv, C. Zhang, and L. R. Dalton, "Fabrication and replication of polymer integrated optical devices using electron-beam lithography and soft lithography," J. Phys. Chem. B 108, 8606-8613 (2004).

[11] H. Schmitt, L. Frey, H. Ryssel, M. Rommel, and C. Lehrer, "UV nanoimprint materials: Surface energies, residual layers, and imprint quality," J. Vac. Sci. Technol. B 25, 785-790 (2007).

[12] W.-S. Kim, J.-H. Lee, S.-Y. Shin, B.-S. Bae, and Y.-C. Kim, “Fabrication of Ridge Waveguides by UV Embossing and Stamping of Sol-Gel Hybrid Materials,” IEEE Photonics Technol. Lett. 16, 1888-1890 (2004).

[13] G. T. Paloczi, Y. Huang, J. Scheuer, and A. Yariv, "Soft lithography molding of polymer integrated optical devices: Reduction of the background residue," J. Vac. Sci. Technol. B 22, 1764-1769 (2004).

[14] H. Lee, " Effect of imprinting pressure on residual layer thickness in UV nano-imprint lithography (vol 23, pg 1102, 2005),” J. Vac. Sci. Technol. B 23, 2176-2176 (2005).

[15] T. Han, S. Madden, M. Zhang, R. Charters, and B. Luther-Davies, “Low loss high index contrast nanoimprinted polysiloxane waveguides,” Opt. Express 17, 2623–2630 (2009).

[16] J. Teng, H. Yan, L. Li, M. Zhao, H. Zhang, and G. Morthier, “Simple ultraviolet-based soft-lithography process for fabrication of low-loss polymer polysiloxanes-based waveguides,” IET Optoelectron. 5, 265-269 (2011).

[17] X. Tang, J. Liao, H. Li, L. Zhang, R. Lu, and Y. Liu, “A novel scheme for 1×N optical power splitter,” Opt. Express 18, 21697-21704 (2010).

[18] S. H. Tao, Q. Fang, J. F. Song, M. B. Yu, G. Q. Lo, and D. L. Kwong, "Cascade wide-angle Y-junction 1 × 16 optical power splitter based on silicon wire waveguides on silicon-on-insulator," Opt. Express 16, 21456-21461 (2008).

[19] A. Yariv, “Universal relations for coupling of optical power between microresonators and dielectric waveguides,” Electron. Lett. 36, 321-322 (2000).

[20] A. Yariv, “Critical coupling and its control in optical waveguide-ring resonator systems,” IEEE Photonics Technol. Lett. 14, 483-485 (2002).

[21] D. Dai, B. Yang, L. Yang, Z. Sheng, and S. He, “Compact Microracetrack Resonator Devices Based on Small SU-8 Polymer Strip Waveguides,” IEEE Photonics Technol. Lett. 21, 254-256 (2009).

[22] W.-Y. Chen, R. Grover, T. A. Ibrahim, V. Van, W. N. Herman, and P.-T. Ho, “High-Finesse Laterally-Coupled Single-Mode Benzocyclobutene Micro-Ring Resonators,” IEEE Photonics Technol. Lett. 16, 470-472 (2004).

[23] J. K. S. Poon, L. Zhu, G. A. DeRose, and A. Yariv, “Polymer Microring Coupled-Resonator Optical Waveguides,” J. Lightwave Technol. 24, 1843-1849 (2006).

[24] N. Xie, S. Member, T. Hashimoto, and K. Utaka, “Very Low Power Operation of Compact MMI Polymer Thermooptic Switch,” IEEE Photonics Technol. Lett. 21, 1335-1337 (2009).

[25] S. Yamagata, Y. Yanagase, and Y. Kokubun, “Wide-Range Tunable Microring Resonator Filter by Thermo-Optic Effect in Polymer Waveguide,” Jpn. J. Appl. Phys. 43, 5766-5770 (2004).

[26] J. Zhang, X. Han, H. Song, J. Teng, P. Wu, L.Wang, and M. Zhao, “Study on Time Delay Characteristics of Integrated Waveguide Microring Resonator with Tunable Coupler,” Acta Optica Si. 30, 2098-2103 (2010).

Chapter 4 Optical single sideband radio over fiber transmission

4.1 Introduction

Various microwave photonic filters have been extensively studied in view of their promising applications to broadband wireless access networks, radio over fiber systems, radars for moving target identification, satellite communication systems, and so forth [1]. These filters leverage the advantages of photonic signal processing by moving the filtering operation to the optical domain, which offers the benefits of wide bandwidth, low loss, and natural immunity to electromagnetic interference [2, 3].

Generally speaking, most of microwave photonic filters (MPFs) have been implemented with commercially available discrete components such as single mode fibers (SMFs), couplers, fiber Bragg gratings, and one or more optical sources [1, 2]. In contrast to these discrete components, integrated waveguide MPFs have the potential to bring down volume, weight and power consumption of signal processing equipments [4], which is essentially important in aircraft and space satellite communication systems [5-7], especially if integration with electro-optical modulators (EOMs) and photo detectors (PDs) is possible.

Polymer-based integrated waveguide devices for microwave photonic signal processing, such as the compact optical true time delay lines [8, 9], high bandwidth EOMs [10], reconfigurable bandpass filters [11] and so on, have been demonstrated. In this chapter, the PSQ-Ls polymer-based microring notch filter fabricated by UV-based soft-imprint technology was used to realize optical single sideband (OSSB) filtering response. The chromatic dispersion induced fading effect was suppressed effectively. 20 Msps quadrature phase shift keying (QPSK) signal carried by a 19.61 GHz microwave was transmitted successfully over 6.15 km SMF.

4.2 **Fiber dispersion induced fading effect**

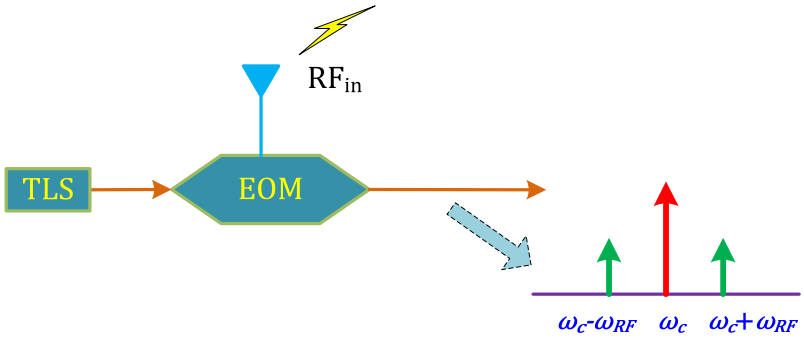

Fig. 4.1 Schematic picture for the generation of ODSB.

As shown in Fig. 4.1, under the condition that the modulator is working in the linear zone, when a microwave signal with a frequency of f_{RF} is modulated onto the optical carrier λ_c generated by a single-mode laser, an optical double sideband (ODSB) signal will be created. Two sideband signals with frequency of $\omega_c + \omega_{RF}$ and $\omega_c - \omega_{RF}$ are located symmetrically on both sides of the optical carrier. At the end of the optical receiver, each sideband beats with the optical carrier to produce two beat signals. If these two beat signals interfere constructively, the microwave signal can be resumed. However, due to the inevitable fiber chromatic dispersion, such ideal phase relationship tends to be broken down, resulting in the power degradation of the obtained RF (radio-frequency) signal. Theoretically, the obtained RF power can be expressed as:

$$P_{RF} \propto \cos^2\left(\frac{\varphi_1+\varphi_2}{2}\right) = \cos^2\left(\frac{\pi LD\lambda_c^2 f_{RF}^2}{c}\right) \tag{4.1}$$

where φ_1 and φ_2 represent the phase delays of the spectral component for the two sidebands, *D* is the dispersion parameter of the fiber, *L* is the length of the fiber and *c* is the light speed in vacuum. It can be seen that due to the fiber dispersion, the detected RF power will attenuate to zero with increasing transmission distance for the ODSB signal. The so called “fiber dispersion induced fading effect” [12-14] happens when the following condition is met:

$$\frac{\pi LD\lambda_c^2 f_{RF}^2}{c} = N \cdot \frac{\pi}{2} \ (N = 1, 3, 5 \cdots) \tag{4.2}$$

Fig. 4.2 shows the relation between the received RF power and the length of the transmission fiber link. As can be seen, the RF power exhibits periodic attenuation with the fiber length. Moreover, the higher the RF frequency, the more pronounced the dispersion effect. Because of the fading effect on the fiber link, the distance that the RF signal can be transmitted is severely limited.

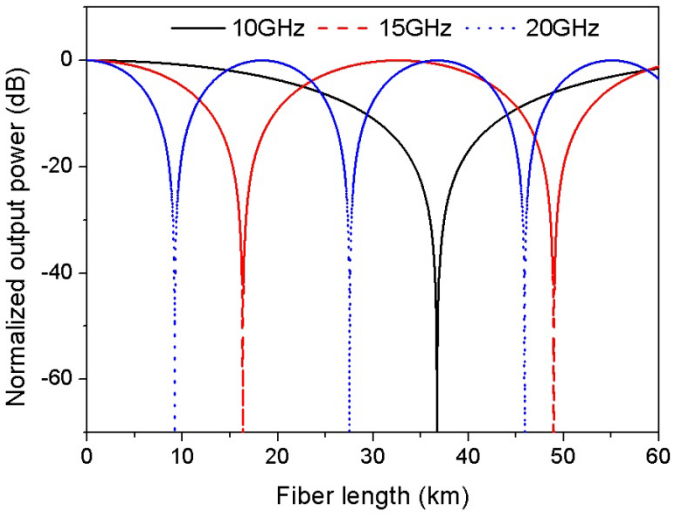

Fig. 4.2 The relation between the received RF power and the length of the transmission fiber link.

4.3 System setup for realizing quasi optical single sideband (OSSB) signal

The power fading effect can be alleviated by the use of OSSB signals, in which one of the sidebands of the RF modulated optical signal is suppressed. Besides the benefit of increasing the transmission length, OSSB signals also take up less bandwidth resource than ODSB signals. However, it should be noted that this method sacrifices half of the RF power, which is its drawback.

There already exist many methods to generate OSSB signals. In this work, it is realized through the fabricated PSQ-Ls polymer-based microring notch filter. Fig. 4.3 shows the schematic diagram of the experimental setup. An optical wave from the tunable laser source is intensity-modulated by a radio-

frequency signal generated from a RF source. The output field is then applied to the polymer-based microring notch filter. The erbium-doped fiber amplifier (EDFA) is used to compensate the coupling loss between the lensed fibers and the waveguides, as well as the insertion loss of the polarization controller. After transmitting over SMF, the optical property is measured by the optical spectrum analyzer (OSA) and the RF signal property from PD is measured by the RF spectrum analyzer, respectively. A discrete EOM is used in this proof-of-principle demonstration, but it can eventually be integrated on the chip in the ultimate design. The polymer-based microring notch filter is used to suppress one of the double sidebands of the microwave modulated optical wave. Then the OSSB transmission over the SMF can be realized.

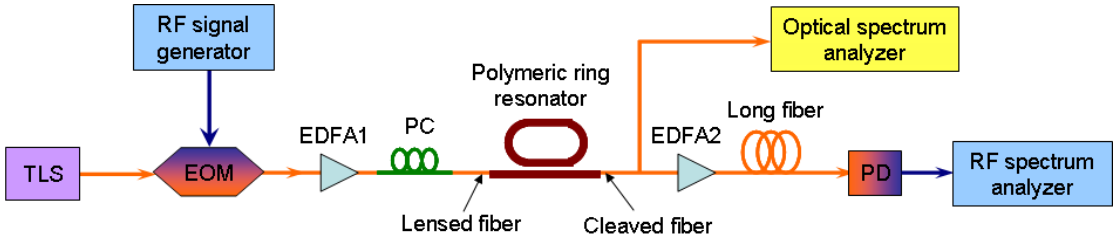

Fig. 4.3 Schematic diagram of the experiment setup for RoF signal transmission over long fiber link.

The complete measurement procedures are as follows:

- Characterize the performance of the polymer microring notch filter and extract its critical parameters such as resonant wavelength λ_r, free spectral range, extinction ratio and so on.
- According to the length of the optical fiber in our lab ($L = 6.15\,\mathrm{km}$), figure out the microwave frequency ($f_{RF} = 19.61\,\mathrm{GHz}$) at which the detected power will attenuate to zero after transmission. Related calculations are based on equation. 4.2 that describes the fading effect.
- Based on the resonant wavelength λ_r of the microring notch filter and microwave frequency f_{RF}, realize the OSSB filtering through tuning of

the working wavelength of the TLS λ_c. The relation between λ_c and λ_r is $\lambda_c = \lambda_r - \delta\lambda_{RF}$, in which $\delta\lambda_{RF} = \frac{\lambda_r^2}{c} f_{RF}$.

- Measure the optical spectrum of the microwave modulated optical wave without and with OSSB filtering.
- Compare and analyze the signal quality without and with OSSB filtering after a long transmission distance.

4.4 Measurement results and discussion

The transmission of the polymer microring notch filter, the microwave modulated ODSB signal before entering the filter and the microwave modulated OSSB signal passing through the filter are shown in Fig. 4.4, Fig. 4.5 and Fig. 4.6, respectively. The FSR of the polymer microring notch filter is around 0.7nm. One resonant dip appears at the wavelength of 1550.284 nm with an extinction ratio of around 12.5 dB. By comparing Fig. 4.5 and Fig. 4.6, it can be seen that the right sideband of the ODSB signal can be suppressed by about 12.5 dB. It is important to main the temperature stability during the measurement process, as severe drift of the notch filtering response can be caused by the temperature fluctuation due to the high temperature dependence of the polymer ring. Detailed characterization of this temperature dependence of the polymer microring resonator can be seen in section 5.2.6 of chapter 5. Further suppressing of the remaining sideband signal would require higher performance of the filtering device. It can also be seen that the powers of the optical carrier are 11.9 dBm and -17.4 dBm respectively before and after the insertion of the polymer microring notch filter. The large insertion loss comes from the butt coupling loss between the fiber and the waveguide, as well as the waveguide loss itself. This is a useful reference value for us to compare the ODSB and OSSB signal transmission quality over the fiber link, as the ODSB optical signal is attenuated to the same level with a tunable optical attenuator.

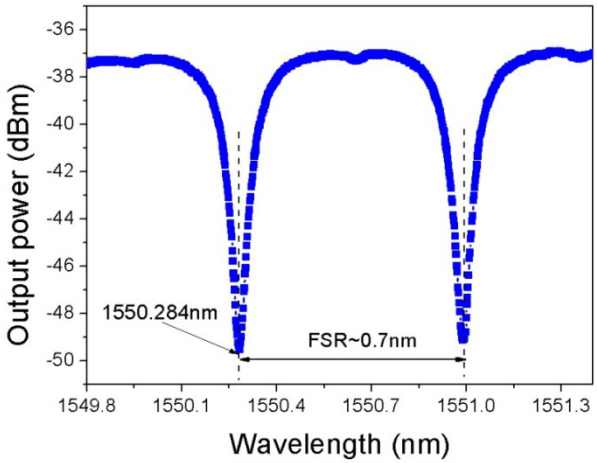

Fig. 4.4 The transmission of the fabricated PSQ-Ls microring notch filter.

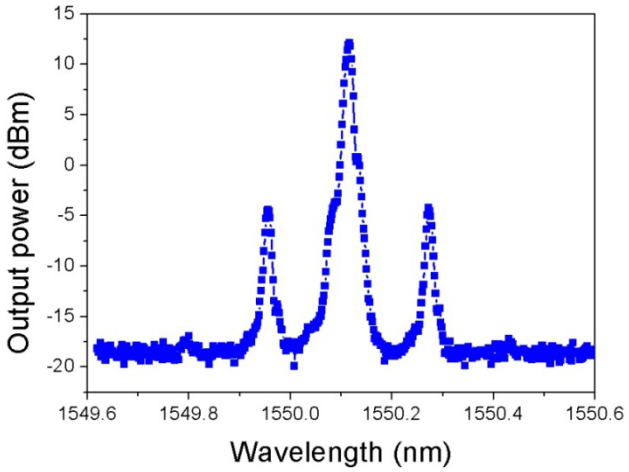

Fig. 4.5 The microwave modulated ODSB signal before entering the filter.

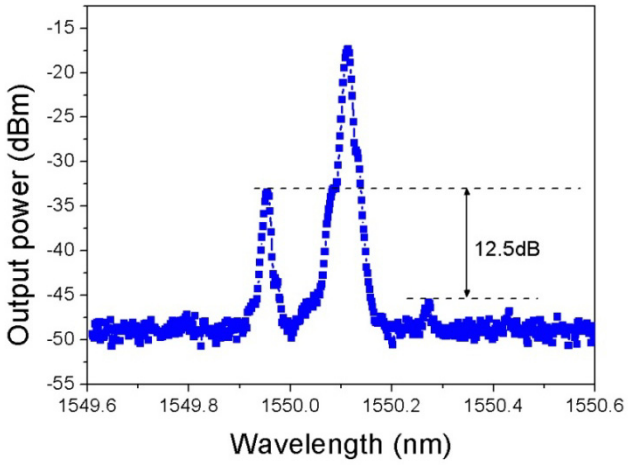

Fig. 4.6 The microwave modulated OSSB signal after passing through the filter.

To demonstrate the validity of the OSSB filtering response of the polymer-based microring notch filter, different rates of QPSK signal carried by a 19.61 GHz microwave were transmitted over the single-mode fiber link. For comparison, the ODSB signal transmission was also tested, with the equal insertion loss as the integrated waveguide chip provided by a tunable optical attenuator. The measurement results are shown in Fig. 4.7.

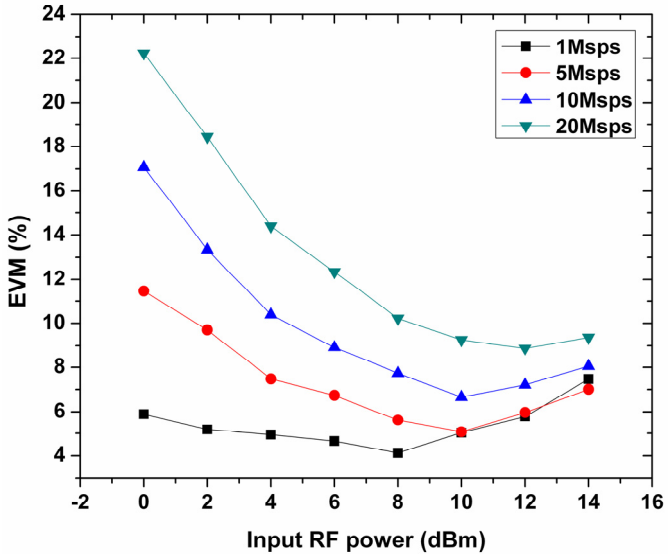

Fig. 4.7 The relationship between the EVM and input RF power with different modulation rate of the QPSK signal.

As can be seen, for each modulation rate of the QPSK signal, the error vector magnitude (EVM) value varies with the input RF power. A lower EVM value is an indication of a higher received signal quality. There exists an optimal input RF power, at which the minimal EVM can be obtained. For example, when the modulation rates of QPSK are 1 Msps, 5 Msps, 10 Msps and 20 Msps, the input RF powers corresponding to the minimal EVM are 8 dBm, 10 dBm, 10 dBm and 12 dBm respectively. The increase of the optimal input RF power with the modulation rate can be explained as follow. The bandwidth taken up by the signal will increase with the modulation rate. Under the condition that the system noise as well as the other factors are

unchanged, the input RF power needs to be increased in order to keep the signal power per unit bandwidth at a relatively high level.

Although the EVM can be optimized with the input RF power, by and large, the EVM still tends to increase with the modulation rate. This can be attributed to higher accumulated noise, as larger bandwidth was taken up by the signal with high modulation rate.

The constellation diagrams of the received signal utilizing the ODSB and the OSSB transmission are shown in Fig. 4.8(a) and Fig. 4.8(b), respectively. The modulation rate of QPSK was 20 Msps. As can be seen, for the OSSB signal transmission, the signal property remained very well after the 6.15km SMF, with the EVM of 8.87% and the SNR (Signal to noise ratio) above 21dB. But the signal deteriorated severely with ODSB transmission, with the EVM of 60.03% and the SNR only 4.33 dB.

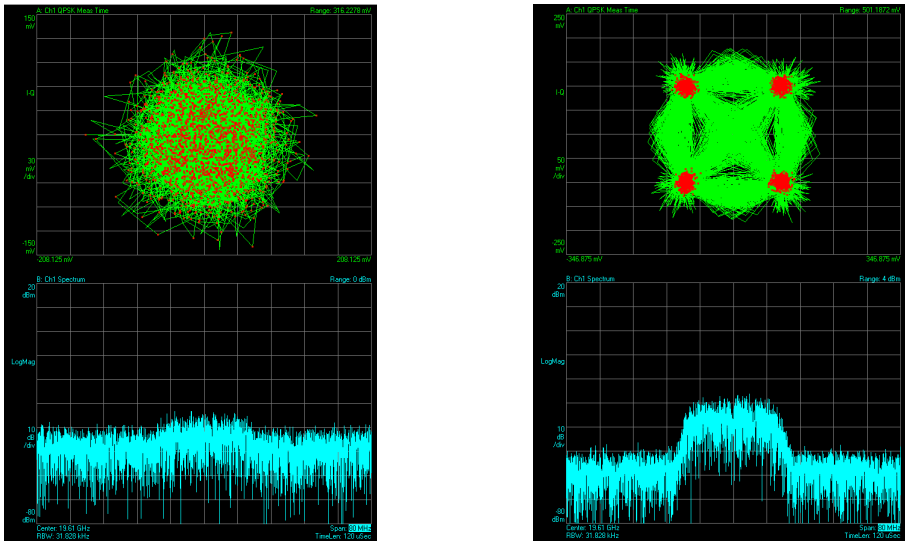

Fig. 4.8 The constellation diagrams of the received signal utilizing (a) the ODSB and (b) the OSSB transmission.

4.5 **Conclusion**

In summary, an integrated waveguide microring resonator based on PSQ-Ls polymer was designed and fabricated by a simple UV-based soft-imprint technology. The quasi OSSB filtering response was achieved effectively by

locating the sideband frequency of microwave modulated optical wave at the resonant frequency of the microring resonator. The chromatic dispersion caused fading effect was suppressed by the integrated waveguide filter with the demonstration of successful transmission of 20 Msps QPSK signal carried by 19.61 GHz microwave over 6.15 km SMF. Methods such as cascading ring resonators or combination with Mach-Zehnder interferometer can be used to further improve the OSSB filtering performance.

4.6 References

[1] J. Capmany, B. Ortega, and D. Pastor, “A tutorial on microwave photonic filters,” J. Lightwave Technol. 24, 201-229 (2006).

[2] R. A. Minasian, “Photonic signal processing of microwave signals,” IEEE Trans. Microwave Theory Tech. 54, 832-846 (2006).

[3] J. Yao, “Microwave photonics,” J. of Lightwave Technol. 27, 314-335 (2009).

[4] A. Seeds, F. Pozzi, C.C, Renaud, M.J. Fice, L. Ponnampalam, D.C. Rogers, L.F. Lealman and R, Gwilliam, “Microwave photonics: opportunities for photonic integration,” 14th European Conference on Integrated Optics, Eindhoven, Netherlands, 123-132 (2008).

[5] M. Y. Chen, X. Lu, H. Subbaraman, and R. T. Chen. “Fully printed phased-array antenna for space communications,” Proc. of SPIE 7318, 731814 (2009).

[6] H. Schippers, J. Verpoorte, P. Jorna, A. Hulzinga, A. Meijerink, C. G. H. Roeloffzen, L. Zhuang , D. A. I. Marpaung, W. van Etten, R. G. Heideman, A. Leinse, A. Borreman, M. Hoekman, M. Wintels, “Broadband conformal phased array with optical beam forming for airborne satellite communication,” IEEE Aerospace Conference, 1-17 (2008).

[7] L. Zhuang, C. G. H. Roeloffzen, A. Meijerink, M. Burla, D. A. I. Marpaung, A. Leinse, M. Hoekman, R. G. Heideman, and W. van Etten, “Novel ring resonator-based integrated photonic beamformer for broadband phased array receive antennas—part II: experimental prototype,” J. Lightwave Technol. 28, 19-31 (2010).

[8] B. Howley, X. Wang, M. Chen, and R. T. Chen, “Reconfigurable delay time polymer planar lightwave circuit for an X-band phased-array antenna demonstration,” J. Lightwave Technol. 25, 883-890 (2007).

[9] C. Chen, Y. Yi, F. Wang, Y. Yan, X. Sun, D. Zhang, “Ultra-long compact optical polymeric array waveguide true-time-delay line devices,” IEEE J. Quantum Electron. 46, 754-761 (2010).

[10] B. Bortnik, Y.-C Hung, H. Tazawa, B.-J Seo, J. Luo, A. K.-Y. Jen, W. H. Steier, H. R. Fetterman, “Electrooptic polymer ring resonator modulation up to 165 GHz,” IEEE J. Sel. Top. Quantum Electron. 13, 104 – 110 (2007).

[11] G.-D Kim and S.-S Lee, “Photonic microwave reconfigurable filter based on a tunable polymeric ring resonator,” Opt. Commun. 278, 303-306 (2007).

[12] U. Gliese, S. Ngrskov, and T. N. Nielsen, “Chromatic dispersion in fiber-optic microwave and millimeter-wave links,” IEEE Trans. Microwave Theory and Tech. 44, 1716-1724 (1996).

[13] G. H. Smith, D. Novak, and Z. Ahmed, “Overcoming chromatic-dispersion effects in fiber-wireless systems incorporating external modulators,” IEEE Trans. Microwave Theory Tech. 45, 1410-1415 (1997).

[14] J. Park, W. V. Sorin and K. Y. Lau, “Elimination of the fibre chromatic dispersion penalty on 1550 nm millimetre-wave optical transmission,” Electron. Lett. 33, 512-513 (1997).

Chapter 5 A label-free optical biosensor built on the polymer platform

5.1 Introduction

Biological and chemical sensors have become more and more important due to their vast application potential in the fields of food safety, environmental monitoring, point-of-care diagnostics, drug discovery and so on. Among different types of sensors, planar integrated photonic biosensors have distinct advantages. Label-free and real-time monitoring of the dynamics of biomolecules' reactions are feasible when an integrated photonic device is used as transducer, avoiding the traditional method of enzyme-linked immunosorbent assay (ELISA), which is labor and time consuming. In addition, these planar photonic biosensors have the capability to be further integrated with other electronic, photonic, biochemical and microfluidic components, thus paving the way towards the realization of "Lab-on-Chip" [1]. One good candidate for this is silicon photonics, which has gained significant progress with vast investment recently. State-of-the-art silicon photonic devices (e.g. microring resonator) have been shown [2], pushing label-free biosensing closer to application level [3]. However, further reducing the cost of these photonic devices would still be desired to make as many users as possible benefit from this technology.

In Chapter 2, polymer has been shown to be an ideal material option for integrated photonic devices among different materials. The cost of the material itself is very low, which makes it attractive where the economic factor needs to be taken into account. The tunable properties of the polymer give the design and fabrication of the photonic devices much more flexibility. It is noted that compared to inorganic materials, biocompatiblity is another important and unique feature of polymers. Moreover, the biochemical surface treatment of the polymer photonic devices can be greatly simplified. Also, it is shown in Chpater 3 that besides the traditional mature semiconductor processing methods, many novel fabrication techniques, nanoimprint lithography for

example, can be applied to process the polymer. The latter method has lots of merits such as high resolution, minimal requirements for complicated equipment, simple fabrication processes involved, and a huge potential for high throughput. Based on the advantages mentioned above, this platform provides us an opportunity to develop an extremely low cost thus disposable label-free optical biosensor.

On the other hand, planar integrated optical biosensors can be designed into different structures. SPR (Surface plasmon resonance) [4-6], M-Z (Mach-zehnder) interferometer [7, 8] and microring structures [9-13] are three types that are usually seen. Although the first two have some merits, their drawbacks are also quite obvious. For example, SPR structure is with very high loss. For biosensing, the measurement results are not straightforward and extra interpretation is needed. M-Z requires relatively longer sensing arms to generate sufficient phase shift, therefore the device's dimension can be a problem. Compared with them, a resonant cavity structure (e.g. a microring resonator) is attractive for biosensing because it effectively increases the interaction length between the evanescent field of the waveguide mode and the target analytes without increasing the physical length of the sensing arm, thus greatly reducing the device's footprint.

In this chapter, a label-free optical biosensor built on a low cost polymer platform will be presented. Several issues during the development process will be discussed. At first, a brief introduction to the sensing scheme will be given, followed by some waveguide design considerations. We choose a microring resonator as the key optical device, which plays the role as transducer, thus a detailed analysis will be given to acquire high performance. With the solution delivering capability provided by the microfluidic channel that is assembled with the device chip, the results for the homogeneous sensing of NaCl solutions under different concentrations are presented. Next, emphasis will be put on the demonstration of biomolecules sensing. The surface of the polymer microring resonator will be functionalized to have the capability to capture targeted analytes. The details of the surface treatment procedures and their characterization will be revealed. Finally, the measurement results with

discussions are given to show the working reliability of our proposed biosensor.

5.2 Theoretical analysis

5.2.1 Sensing scheme: bulk sensing and surface sensing

There are usually two sensing mechanisms for optical biosensors: bulk sensing and surface sensing. Their schemes are shown in Fig. 5.1. In bulk sensing, analytes are homogeneous distributed within the solution. The analyte solution covers the top of the optical device, and acts as the upper cladding for optical waveguides. When there is a weak change in the concentration of the dissolved analytes, the effective refractive index of the waveguide mode will change accordingly, resulting in a change of optical output signals. Therefore the optical device plays the role as a transducer. With bulk sensing, we can readily detect the small changes in the amount of the substitutes such as salt, glucose and so on. But the weakness of this mechanism is that it has no specificity. In other words, any substitute that can change the refractive index of the solution will produce a change in the optical output signal. This problem can be overcome by surface sensing. In this mechanism, the surfaces of the optical device are functionalized with a monolayer of biomolecules. These biomolecules are also called bio-receptors because they provide binding sites for dispersing biomolecules waiting to be analyzed. Only the biomolecules in the solution that have a complementary structure to the immobilized bio-receptors can be captured and fixed onto the surfaces of the optical device to generate signal.

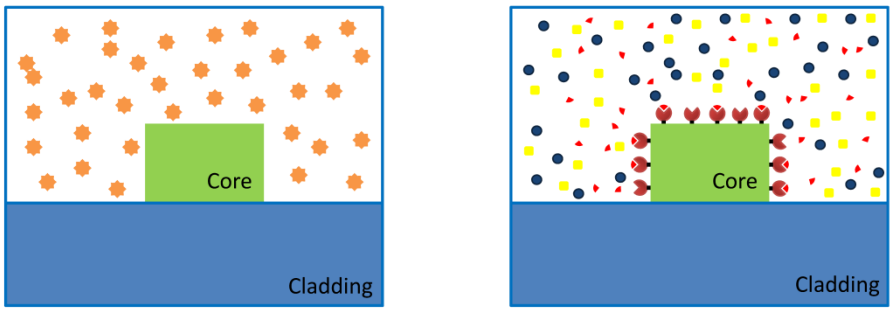

(a) (b)

Fig. 5.1 Two sensing mechanisms for the optical biosensor. (a) Bulk sensing. (b) Surface sensing.

5.2.2 Interrogation schemes of microring resonators

When using a microring resonator as the basic component to construct the optical biosensor, there are two interrogation schemes to transduce the bio/chemical signals into optical signals: monitoring the resonant wavelength shift or the intensity variation at a fixed wavelength [14]. The schematic pictures are shown in Fig. 5.2. The former method provides a relatively large dynamic range and its measurement results are straightforward. However, in the case that the resonant peak is very sharp usually an expensive tunable laser is required. Compared to that, the latter method provides a higher sensitivity. Requirements on the light source and detector are also relaxed. But the problem of this method is that its dynamic range is too small. A strict system stability is required in order to suppress the noise to a low level. Because a certain measurement range is needed for our sensing experiment and, more importantly, because the microring resonator we fabricated for this work has a very narrow spectrum, the wavelength interrogation scheme is chosen in this work.

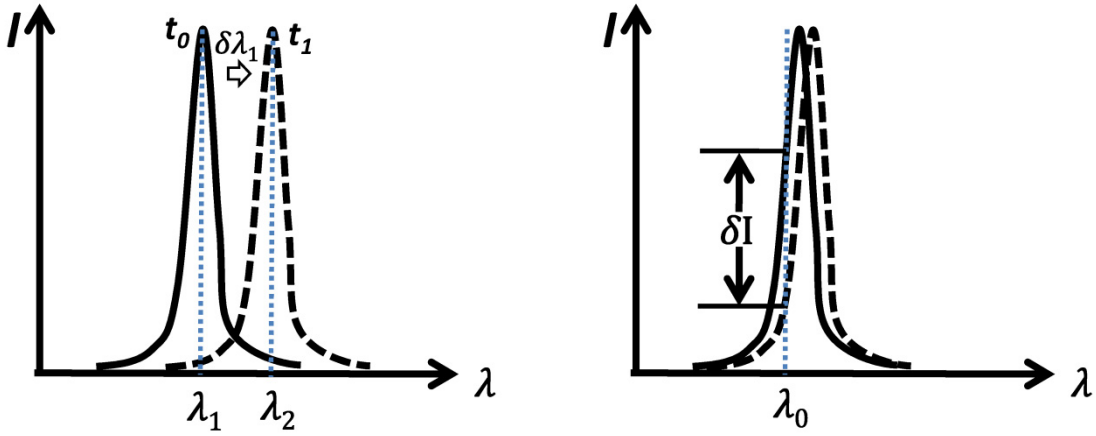

(a) (b)

Fig. 5.2 Two interrogation schemes when the microring resonator is used as optical biosensor.

5.2.3 Optical biosensor's sensitivity and detection limit

There are two important parameters that can reflect the performance of the biosensor. They are sensitivity and detection limit respectively, which will be introduced in this section.

For bulk sensing, the sensitivity *S* is defined as the ratio of the resonant wavelength shift to the refractive index change of the surrounding environment n_c, which is expressed as:

$$S = \frac{\partial \lambda_m}{\partial n_c} = \frac{\partial \lambda_m}{\partial n_{eff}} \frac{\partial n_{eff}}{\partial n_c} \xrightarrow{m\lambda = L n_{eff}} \frac{\lambda_m}{n_{eff}} \frac{\partial n_{eff}}{\partial n_c} \tag{5.1}$$

where λ_m is the resonant wavelength and *m* is its order, n_{eff} is the effective refractive index of the waveguide mode, and *L* is the round trip length. As can be seen, the sensitivity is determined by the factor $\frac{\partial n_{eff}}{\partial n_c}$, of which the physical meaning is quite apparent. It indicates to what extent the changes in the surrounding environment can exert influence on the waveguide mode. Thus the sensitivity improves if the waveguide mode has more interaction with the surrounding environment, which can be achieved by reducing the waveguide dimension or utilizing special structures to delocalize or expand the

waveguide mode. One typical example is the slot waveguide microring resonator made in silicon. The mode property determines the optical field to be mainly concentrated within the slot areas, which are filled with surrounding material. The strong interaction between them allows such biosensor to have very high sensitivity. Similarly, the factor $\frac{\partial n_{eff}}{\partial t}$ plays an important role for sensitivity with surface sensing mechanism, where t is the thickness of the biolayer. In this case it is advantageous if the waveguide structure has a large boundary field at the surface and this field decays quickly away from the surface. Waveguides with such field property strongly feel the biolayer present on their surface. For this reason, a higher waveguide refractive index is preferred.

The detection limit is a physical parameter that reflects what is the smallest change of the amount of analyte that can still be detected by the biosensor. For microring resonator based biosensors utilizing the resonant wavelength shift interrogation scheme, the detection limit is defined as the ratio of the minimal wavelength shift that can be resolved to the sensitivity, which is:

$$D = \frac{\delta\lambda_c}{S} = \frac{\delta\lambda_c}{\frac{\lambda_m}{n_{eff}} \cdot \frac{\partial n_{eff}}{\partial n_c}} = \frac{n_{eff}}{\frac{\lambda_m}{\delta\lambda_c} \cdot \frac{\partial n_{eff}}{\partial n_c}} \tag{5.2}$$

Usually, $\delta\lambda_c$ can be taken as a fraction of the spectral width of the resonant peak, which is defined as the full width at half maximum (FWHM) of the resonance. Its relationship to the Q value of the ring is:

$$\Delta\lambda_{FWHM} = \frac{\lambda_m}{Q} \tag{5.3}$$

Considering equation (5.1), (5.2) and (5.3), the detection limit D is inversely proportional to the Q value and sensitivity S:

$$D \sim \frac{1}{Q \cdot S} \tag{5.4}$$

Thus, in order to obtain a lower detection limit, a higher Q value and sensitivity of the ring resonator are desired, which are also the optimization targets of our design.

5.2.4 Waveguide design considerations

As mentioned in Chapter 3, there are two types of the waveguide structures available for us to build the microring resonator based biosensors: inverted-rib and ridge shaped waveguides. Their schematic pictures are shown in Fig. 5.3. From the point of view for fabrication, the former is easier to obtain than the latter. However, which one of them is suitable for biosensing needs to be carefully judged. Sensitivity can be the first important standard. Thus, sensitivities are calculated for both of them with different waveguide dimensions. The results are shown in Fig. 5.4. In general, the sensitivity for the inverted-rib waveguide microring resonator is several times less than that of the ridge shaped waveguide ring resonator. This can be explained with the waveguide mode property. For inverted-rib waveguide structures, most of the light is confined within the waveguide core, being buried within the lower cladding. Only a small portion of the light is able to penetrate into the upper cladding to interact with the analyte, thus making it less sensitive to the environmental change. In comparison, ridge shaped waveguides have more contact area for the waveguide mode to interact with the surrounding analyte material and thus have higher sensitivity. As can be seen from Fig. 5.4(a), once the height is fixed, adjusting the waveguide width has little influence on the sensitivity of an inverted-rib waveguide microring resonator. Reducing the height would help but this is detrimental for the waveguide mode. From Fig. 5.4(b), reducing the slab height would help improve the sensitivity and its influence on the TM mode is larger than on the TE mode. However, this slab height is limited to around 0.8 μm during actual fabrication because of the viscosity of the core material PSQ-LH, and the spin coating process. So the sensitivity is limited to below 18 nm/RIU even for the most sensitive case, for the TM mode with waveguide height of 1.4 μm. Increasing the height would further reduce this value. From Fig. 5.4(c), for the ridge shaped waveguide microring resonator, either reducing the residual layer thickness or reducing the waveguide width can help improving the sensitivity. The former can be achieved with the “minimal polymer squeezing” method introduced before,

while the latter needs to be further traded off during the microring design to

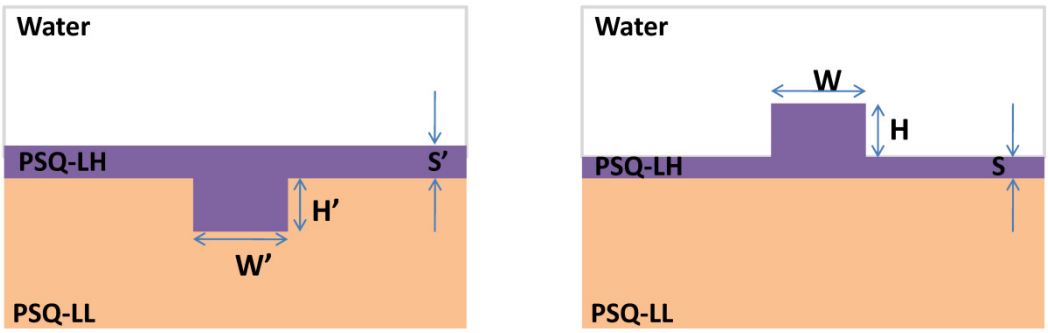

(a) (b)

Fig. 5.3 Schematic pictures of the fabricated polymer waveguides. (a) Inverted-rib structure. (b) Ridge shaped structure.

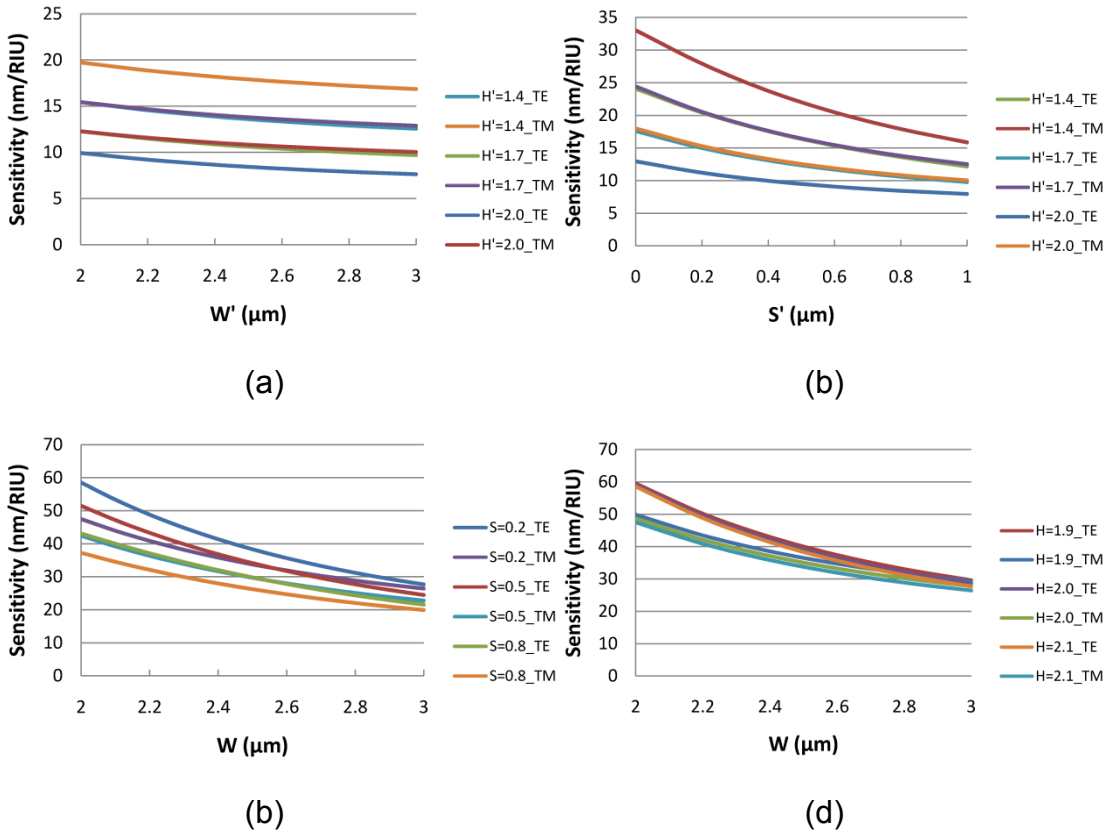

(a) (b)

(b) (d)

Fig. 5.4 The sensitivities of the polymer microring resonators with different waveguide structures and dimensions.

achieve less loss and thus higher performances. At the same time, it is found that once the residual layer is suppressed to a low value (*e.g.* 0.2 μm), a 0.1 μm height variation would have negligible impact on the sensitivity, which indicates that a certain height variation is permitted during fabrication. Generally, the TE mode has a little bit higher sensitivity than the TM mode.

5.2.5 Design consideration for microring resonator

In the next step, the structure of the ring resonator has to be fixed. This is started with the bending loss calculation of ridge shape waveguide of different cross section dimensions at different radius. All the calculations are assumed with water cladding, whose refractive index is 1.3105. The results are shown in Fig. 5.5. As can be seen, although small waveguide width would help increase the sensitivity, it should not be reduced too much in order to void high bending loss, especially under small radius condition. FSR and Q value are together used as judged standards for fixing an appropriate radius value. According to the fundamental ring theories, on one hand, large radius can to some extent increase the Q value, which would help lower the detection limit. On the other hand, the FSR of the ring resonator decreases with larger radius. The FSR should not be too small as a sufficient window is needed to perform the biosensing. This can be predicted by the surface sensing model, which will be illustrated later. For us, waveguide width value of 2.3 μm, height value of 2.1 μm, residual layer with a thickness of 0.2 μm and ring radius of 350 μm can meet the above requirements, which can also be realized with the developed fabrication technology. The fundamental TE mode for the waveguide with above dimensions is shown in Fig. 5.6.

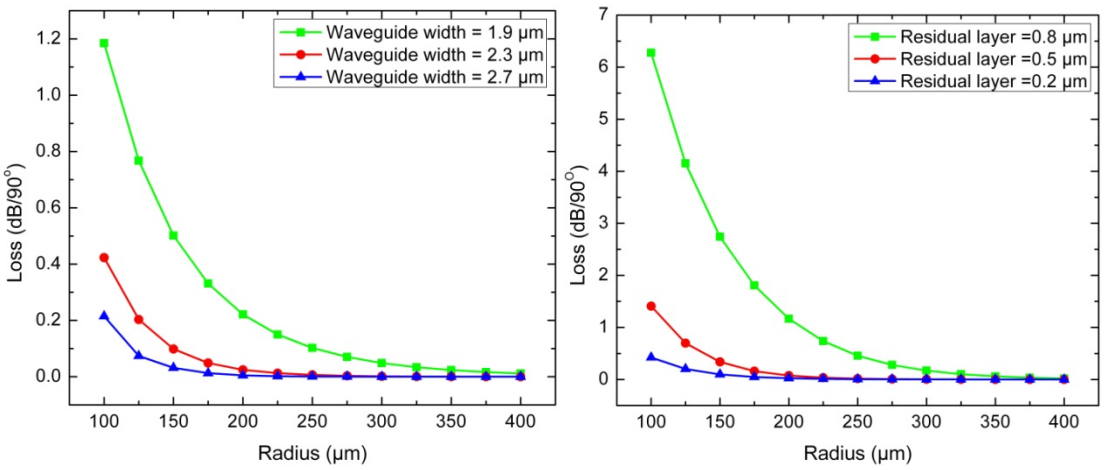

(a) (b)

Fig. 5.5 The bend losses of the polymer ridge shaped waveguide with different dimensions.

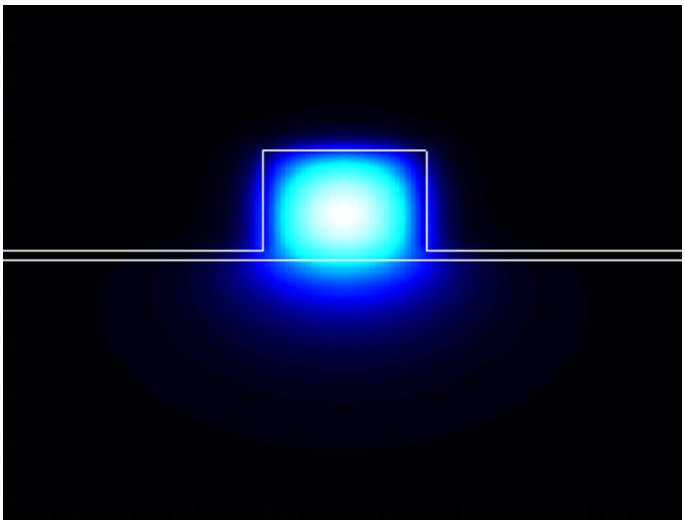

Fig. 5.6 The fundamental TE mode for the polymer ridge shaped waveguide.

Transmission of the ring resonator at the drop port is preferred over that at the through port, as the former provides a much more clean spectrum with “on” and “off” states, while fringes can usually be seen in the transmission spectrum of the through port, resulting in higher noise disturbance. Theoretical analysis has shown that increasing the extinction ratio of the resonance can effectively improve the measurement resolution, thus the sensor performance

[15]. This is achieved by two methods in this work: decreasing the coupling efficiency between the ring and two channel waveguides and reduction of the round trip loss of the ring. The result is shown in Fig. 5.7. As can been seen, with the same coupling efficiency, the lower the round trip loss of the ring, the higher the extinction ratio of the transmission at its drop port. When the round trip loss of the ring resonator is fixed, high extinction ratio can be obtained by allowing the ring to work under low-coupling regime. In fact, the round trip loss of 1.5 dB is extracted from the measurement results. However, compared to air cladding, the coupling efficiency between channel waveguides and ring would increase dramatically when the resonator is working under aqueous sensing environment. Thus coupling length should be controlled appropriately.

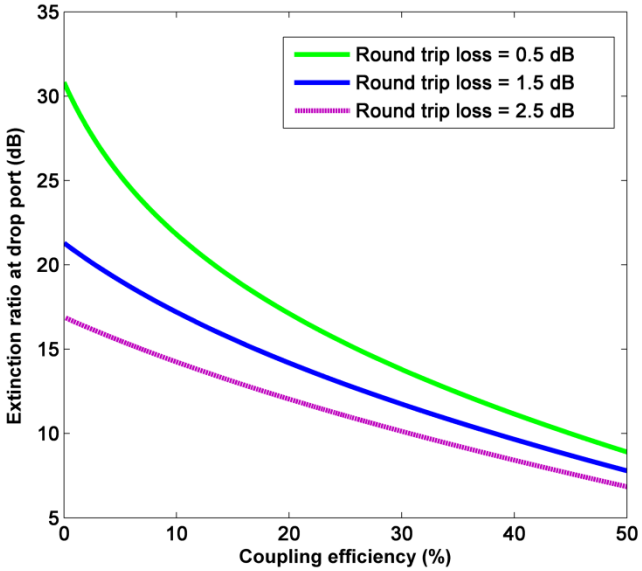

Fig. 5.7 Relationship between the extinction ratio and the coupling efficiency.

Once the material, structure and fabrication technique are made certain, the total loss of the ring resonator is fixed, which include waveguide propagation loss, mode mismatch loss at the junction of straight and bend waveguide and insertion loss of the directional coupler. When it is used for biosensing, additional loss would be attributed to the water absorption, which is as high as 10.9 /cm (~50 dB/cm) at 1550nm wavelength. Broadening of the resonant spectrum of polymer ring resonator from air to water has been observed

during experiments, which is shown in Fig. 5.8. The Q factors of the ring resonator in air and water are 5×10^4 and 2.7×10^4 respectively. Spectrum width with a value of 0.053 nm can still be obtained. The obtained Q values are also among the highest values reported so far for polymer-based microring resonators. It is interesting if the behaviors of polymer ring resonator and SOI microring in water environment are compared. Strong electric field present at the surface of SOI ring, which is due to the extremely high refractive index contrast, is the advantage of using it for biosensing. But the

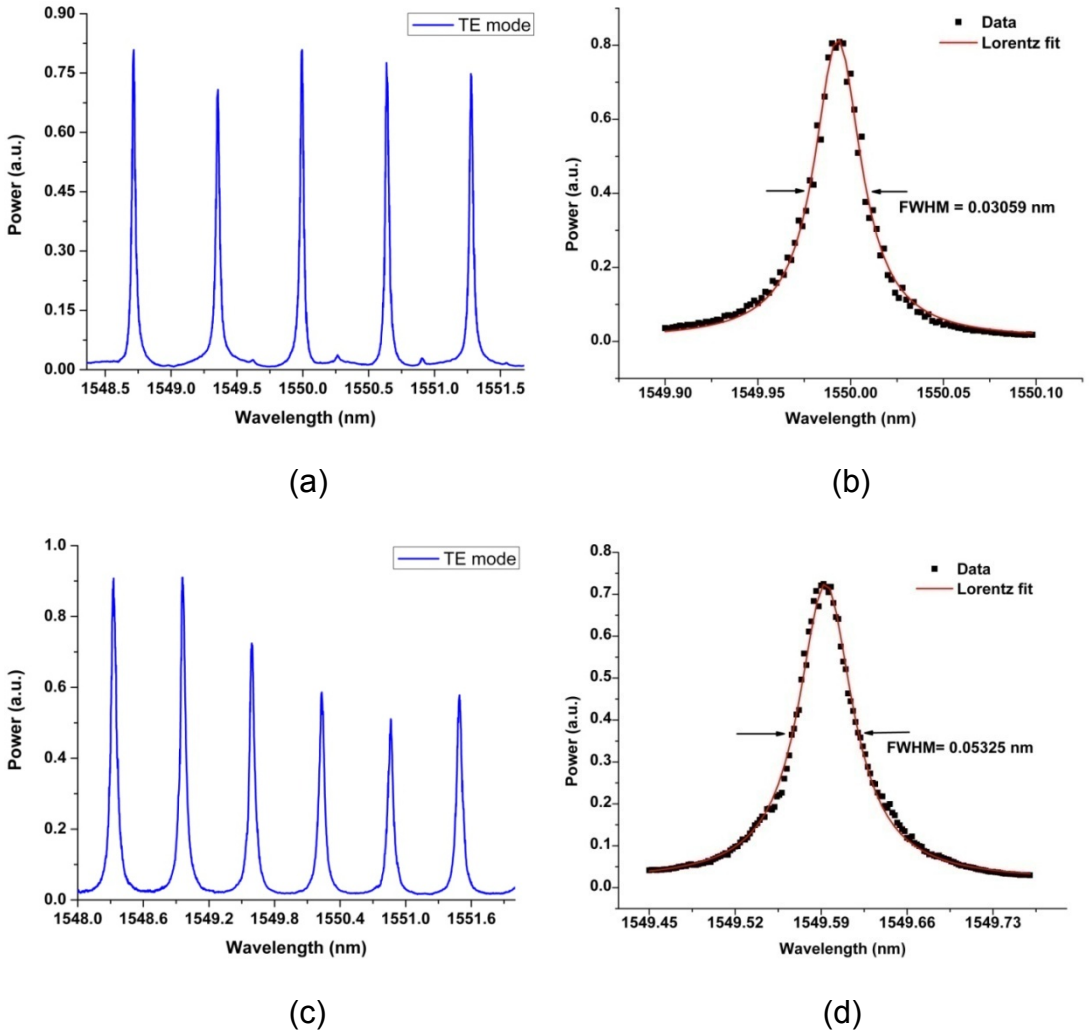

Fig. 5.8 The measuring results of the fabricated ring resonator with, (a) Air as upper cladding, (b) Fitting result of (a), (c) Water as upper cladding, (d) Fitting result for (c).

drawback is that high water absorption loss imposed on silicon microring waveguide degrades the performance of the ring significantly at the same time. For SOI microring working with TE mode, its Q value drops quickly from ~2×10^4 in air to only 5000 in water, with a spectrum width of around 300 pm. Compared with that, low index contrast polymer ring can still provide a sharp peak in water environment, with compromised surface sensing capability though. So actually, there is a trade-off relationship between the resonant peak width and surface sensitivity. From this view, the total performance of the biosensor built on these two platforms can still be comparable.

5.2.6 Surface sensitivity

Based on the optical waveguide model in Fig. 5.3b, an optical surface sensing model can be built to estimate the surface sensitivity of the polymer microring resonator, which is shown in Fig. 5.9. The biomolecular layer is assumed to be a uniform layer with a thickness of t that covers on top of the waveguide surface. As protein is what we actually deal with in our experiment, the refractive index of this layer can be reasonably approximated as 1.45 [16, 17]. With this model, the resonant wavelength shift caused by the molecular interaction for a specific waveguide dimension or the surface sensitivity for different waveguide width can be calculated, which is shown in Fig. 5.10(a) and Fig. 5.10(b). The obtained value here can be compared with the experimental results in section 5.6.2. It can be found that, under the assumption that the thickness of a monolayer human-IgG is typically around 5 nm [18, 19], the experimental wavelength shift is relatively larger than the value predicted here. Considering the long experimental time, it is possible that the binding human-IgG is no longer strictly monolayer. Taking the complex biomolecules morphologies and binding configurations into account would make the case even more complicated.

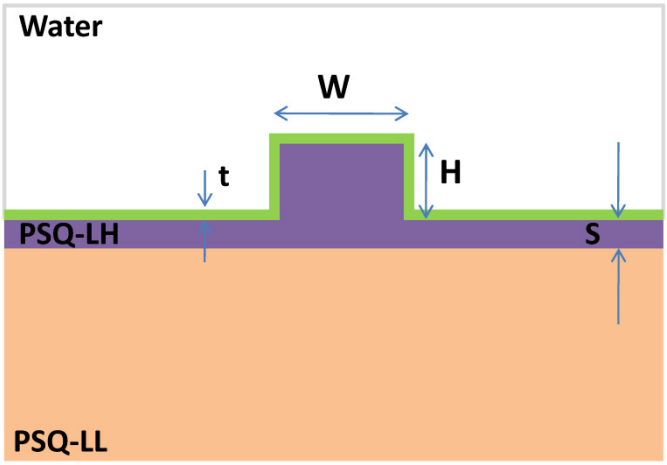

Fig. 5.9 The optical surface sensing model with uniform biolayer covering the waveguide surface.

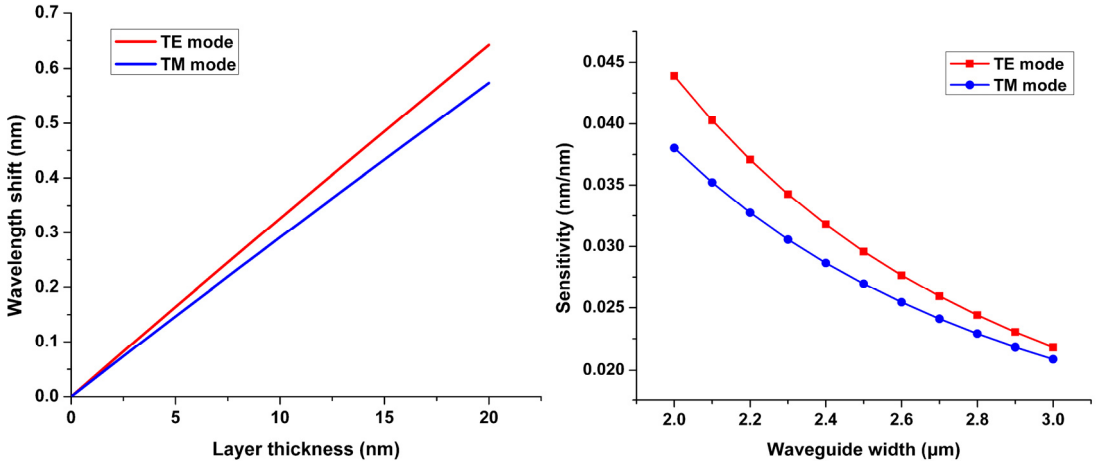

(a) (b)

Fig. 5.10 Simulation for the surface sensitivity. (a) The resonant wavelength shift as a function of the thickness of the biolayer. (b) The surface sensitivity for a uniform biolayer in aqueous solution as a function of the waveguide width. Waveguide height H is 2.1 μm, and residual layer S is 0.2 μm.

5.2.7 Thermal analysis of the fabricated ring resonator

Temperature is one of the challenges that the optical biosensor based on ring resonator must face. Analysis has shown that low Q sensors are typically

limited by amplitude noise and spectral resolution, while temperature induced noise is the main limitation for high Q sensors. In order to see this limitation more clearly, the temperature sensitivity of the fabricated PSQ-Ls polymer microring resonator is characterized. The result is shown in Fig. 5.11. As can be seen, the ring resonator exhibits an temperature dependence as high as 239 pm/˚C. In order to suppress the temperature noise down to a few picometers, which is usually required by this type of biosensor, a temperature stability of ~0.01 ˚C should be satisfied. The requirement on temperature stability will add to the complexity of the whole biosensing system. For polymer microring resonator, this drawback can be overcome by the all-polymer athermal design, which will be shown in section 7.6 of chapter 7.

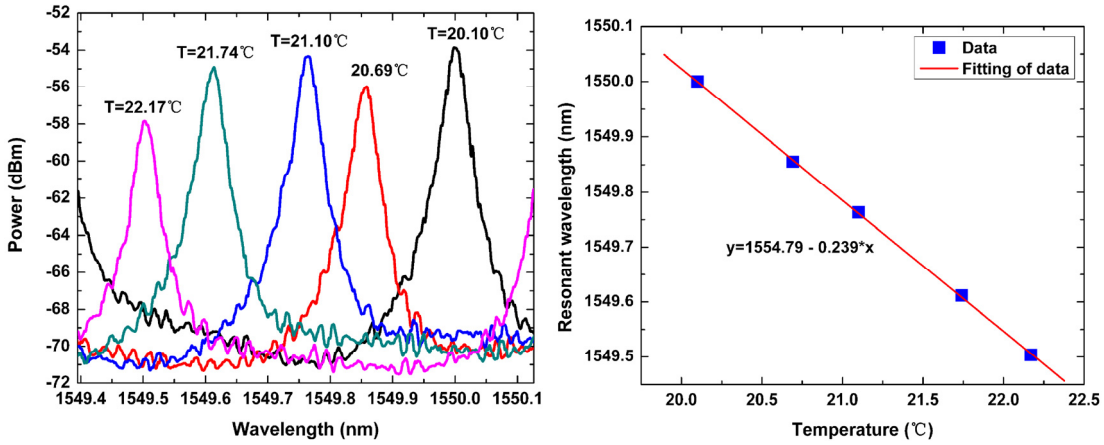

(a) (b)

Fig. 5.11 The temperature sensitivity of the fabricated PSQ-Ls polymer microring resonator. (a) The spectrum with different temperatures. (b) The linear fitting of the resonant wavelengths at different temperatures.

5.3 Surface biological functionalization protocol for polymer microring resonator

In order to endow the fabricated passive microring resonator with the capability of sensing, the surface of the microring needs to be functionalized to have immobilized bioreceptors. Such bioreceptors can fulfill the functions of distinguishing and capturing target analytes, thus they are the other key

component for the optical biosensor besides the transducer itself. Selecting an appropriate coupling protocol according to the sensing mode of biosensor and its transducer's surface characteristic, increasing the immobilization density and homogeneity, decreasing the nonspecific absorption are the main principles of building this biomolecular layer. Its quality has a direct impact on the final performance of the biosensor.

Usually, strategies of bioreceptors' immobilization for biochips involve physical and covalent methods, and the choice of a suitable one is primarily determined by the physicochemical and chemical properties of the interface. Covalent immobilization of bio-receptors on optical biosensors built on inorganic platforms, SOI (Silicon-on-Insulator) for example, have already been demonstrated, where the typical multi-step reactions include surface activation, silanization, target molecule coupling and blocking [20]. This method is not only time and labor consuming, but more importantly, it is a big question whether or not the polymer based optical devices can withstand the multi-step chemical treatments during this process and can still be stable in the measurement environment afterwards.

In this study, we investigate the surface physicochemical property of the optical material PSQ-LH, with which the ring resonator is fabricated. It is found that the entropy driving effect can be effectively taken advantage of to realize protein immobilization due to the hydrophobic property of the chip surface. The protein bioreceptor layer was formed in a self-assembled way through physical absorption. Coating situations for proteins with different molecular weight and surface characterization are compared. The influence of the solution environment on the protein immobilization is discussed. The PA (Staphylococcal protein A) and IgG (human Immunoglobulin G) affinity pair is used for the demonstration of biosensing. The surface of the polymer waveguide is found to have a unique immobilization capability for protein A. The building strategy for the biomolecular layer in this study fully takes advantage of the surface property of the polymer material itself, which greatly simplifies the surface functionalization process of the optical chip, further reducing the cost of the optical biosensor [21, 22].

5.3.1 The estimation of the protein coupling capability for polymer waveguides

The contact angle is the first important parameter for surface characterization, which is a measure of the surface free energy between liquid and solid. Here we use it to prove the entropy driving effect. The static contact angles were measured for samples of bare silicon substrate, polymer PSQ-LH coated silicon substrate and BSA-coated polymer substrate respectively. The results are shown in Fig. 5.12 and Table. 5.1. As can be seen, the polymer PSQ-LH coated surface has obviously a higher hydrophobicity than the bare silicon surface. Protein normally has a hydrophobic core and a partial hydrophobic surface. The protein molecules would exhibit strong tendency to be immobilized on a surface if hydrophobicity of this surface is increased to a certain level. The driving force behind this is the entropy driving effect. BSA is a tool protein which is used a lot in biological technology. It has been shown to have coupling capability with interfaces of many materials, which is also applicable for a PSQ-LH coated surface. The contact angle is dramatically decreased after BSA wrapping, indicating the formation of a hydrated layer. After repeated rinsing with DI water, there is no obvious change of the contact angle value, which primarily proves the stability of the protein on the polymer surface.

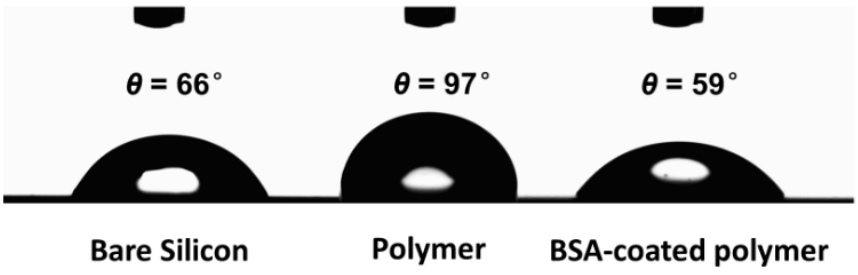

Fig. 5.12 The static contact angle images for bare silicon, polymer and BSA-coated polymer.

Table 5.1 The measurement values in Fig. 5.12.

Sample type	Static contact angle (˚)
Bare silicon substrate	65.5 ± 1.2
PSQ-LH coated silicon substrate	96.8 ± 0.4
BSA-coated polymer substrate	58.55 ± 2.9

5.3.2 Detailed analysis of the protein coupling capability of polymer waveguide surfaces

- *Preparation of Fluorescently Labeled Proteins*

In order to further investigate the coupling capability of the polymer waveguide surface to proteins, three different proteins with typical characteristics were chosen during the experiments, which include BSA (Bovine serum albumin), Ig-G (human Immunoglobulin G) and Lys (lysozyme). Their molecular weights range from 14.4 kDa to 15.0 kDa, and their PI (isoelectric point) from 4.6 to 11.1. All proteins were labeled with FITC (Fluorescein isothiocyanate) at first. The detailed analysis of the fluorescence intensity was performed, which allows a direct and quantitative comparison of the coupling amount between different proteins. Labeling of Bovine serum albumin (BSA), human Immunoglobulin G (IgG) and lysozyme (Lys) with Fluorescein isothiocyanate (FITC) was performed according to the instructions of the FITC manufacturer. Briefly, FITC was dissolved in anhydrous DMSO at 1 mg/mL, and a solution of 2 mg/mL of protein in 0.1 M sodium carbonate buffer, pH 9 was prepared. For each 1 mL of protein solution, 50 µL of FITC solution was added slowly, while gently and continuously stirring the protein solution. The reaction was incubated in the dark for 12 h at 4 ˚C. Afterwards, the excess FITC was removed by gel filtration using Sephadex G-25 column.

The ratio of fluorescein to protein of the product was estimated by measuring the absorbance at 495 nm and 280 nm via a spectrophotometer. The results are shown in Fig. 5.13 and Table. 5.2. The *F/P molar ratio* is defined as the ratio of moles of FITC to moles of protein in the conjugate,

while the *F/P mass ratio* is defined as the ratio of mass of FITC to the mass of protein in the conjugate. They were calculated from the following formulas:

$$Molar\ F/P = \frac{MW}{389} \times \frac{A_{495}E^{0.1\%}}{195[A_{280}-(0.35\times A_{495})]} \quad (5.5)$$

$$Mass\ F/P = \frac{A_{495}E^{0.1\%}}{195[A_{280}-(0.35\times A_{495})]} \quad (5.6)$$

where, *MW* is the molecular weight of the protein; $E^{0.1\%}$ is the absorption at 280 nm of a protein at 1.0 mg/mL; A_{280} and A_{495} are the absorbance of the conjugate sample at 280 nm and 495 nm, respectively.

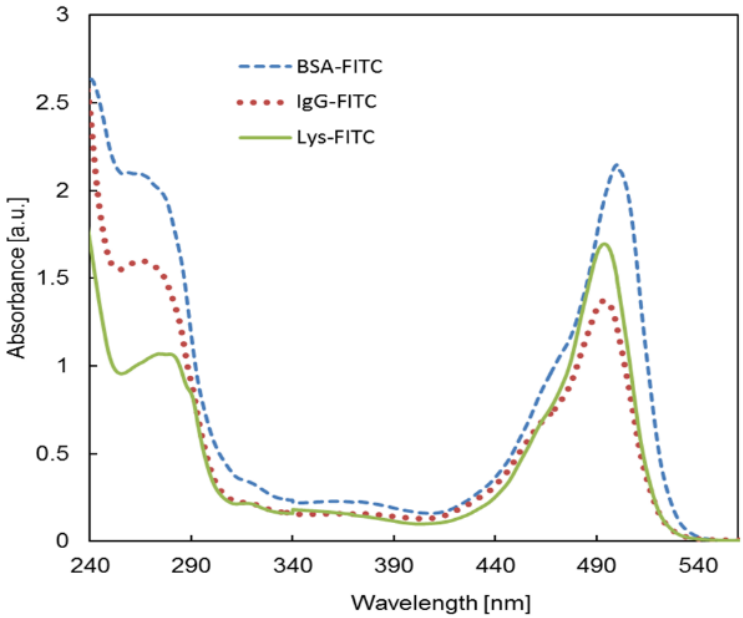

Fig. 5.13 Absorption spectrum of three FITC labeled proteins.

➢ *Protein Coating*

To clean the surface, silicon and polymer slides were immersed in a 5% Tween-20 solution (a commercially available detergent) for 20 minutes, sonicated in DI water for 10 minutes, and rinsed thoroughly with DI water twice. After this, the slides were dried under a stream of nitrogen. The cleaned slides were further used for protein coating. For protein adsorption studies, BSA-FITC, IgG-FITC and Lys-FITC solutions were prepared in PBS (0.01 M, pH 7.4, containing 0.154 M NaCl) at a concentration of 0.5 mg/mL. Adsorption

was performed for 1 hour at 37 ˚C, and another 12 hours at 4 ˚C. Upon completion of adsorption, the slides were thoroughly washed with PBS (0.01 M, pH7.4, containing 0.154 M NaCl) and deionized water separately, and the slides were dried with nitrogen for subsequent analysis.

Table 5.2 Properties of three model proteins and their coupling efficiency with FITC.

Protein	*MW (kDa)*	*IP*	$E^{0.1\%}$	*F/P molar ratio*	*F/P mass ratio (mg/g)*
BSA	66	4.6	0.67	1.00	5.91
IgG	150	8.6	1.40	4.04	10.48
Lys	14.4	11.1	1.49	0.90	24.41

MW: molecular weight; *IP*: isoelectric point; $E^{0.1\%}$: the absorption at 280 nm of a protein at 1.0 mg/mL; *F/P molar ratio*: the ratio of a mole of FITC to a mole of protein in the conjugate; *F/P mass ratio*: the ratio of the mass of FITC to the mass of protein in the conjugate.

- *Detection of Fluorescence Signals*

Fluorescence images were collected using an Olympus IX71 microscope equipped with a 100 W mercury lamp. All pictures were taken under identical lamp illumination and charge-coupled device (CCD) exposure conditions: magnification 100×, exposure time 1/7 s. The fluorescence micrographs were analyzed quantitatively using the software of ImageJ. Each micrograph was transformed into a gray scale image, and its fluorescence intensity was defined as an average gray scale value of a given area based on the statistics of each pixel within the area. The results were expressed in a form of (255-average gray scale)/255. The fluorescence intensity is assumed to be proportional to the amount of adsorbed proteins. However, the fluorescence intensity could not reflect the amount of protein directly when comparing different proteins because of varying FITC coupling ratios on each kind of protein. The term of normalized intensity was defined to reflect the amount of adsorbed proteins directly by considering the F/P mass ratio of each protein

and the effect of fluorescence background of slide material. The obtained imaged and statistic results are shown in Fig. 5.14.

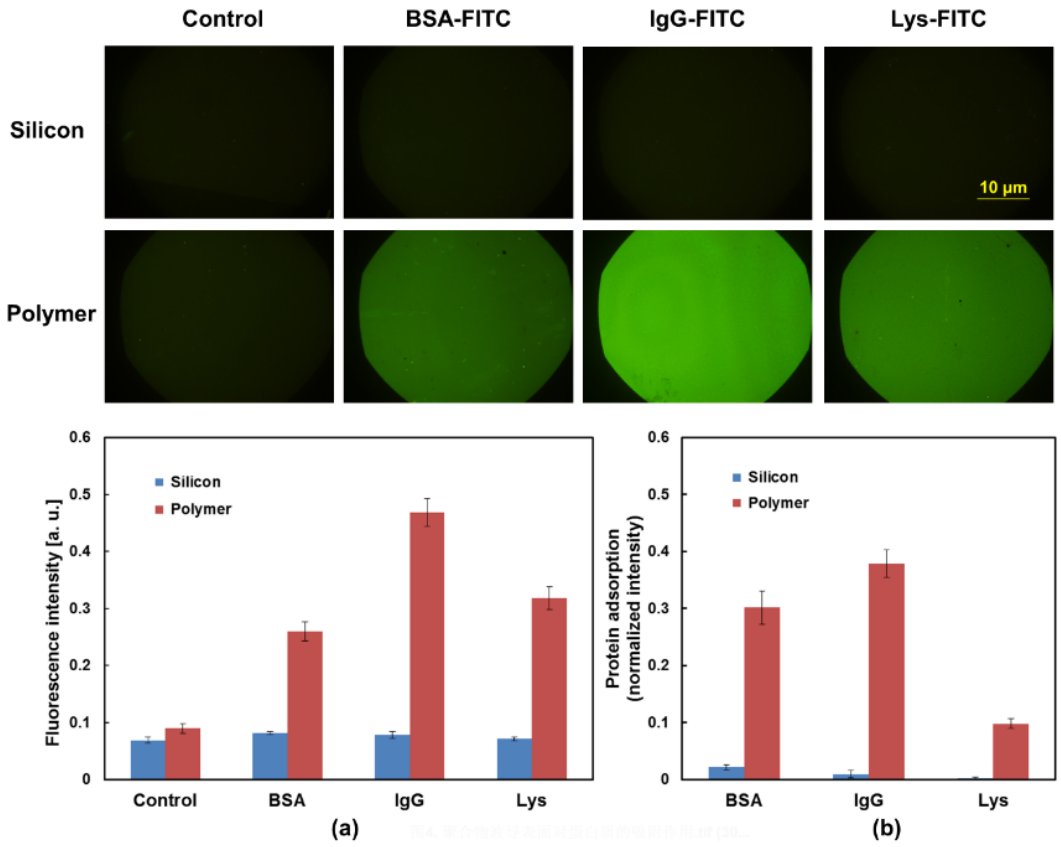

Fig. 5.14 Protein adsorption on the surface of bare silicon slides and polymer slides.

Bare silicon slides (upper row) and polymer slides (lower row) were treated with PBS, BSA-FITC, IgG-FITC and Lys-FITC conjugate solutions (from left to right). All fluorescence micrographs were taken under identical conditions: magnification 100×, exposure time 1/7 s. The fluorescence intensity of each image was analyzed quantitatively (a) and normalized (b) by removing the effect of fluorescence background and considering the individual F/P mass ratio of each protein, which allows a direct comparison of the coupling amount between different proteins.

As can be seen, silicon has almost no absorption for the three kinds of proteins. While the polymer waveguide surface exhibits different extents of

capability to couple the proteins under physiological condition (pH 7.4, 0.154 M NaCl). From the fluorescent images, proteins can be assumed to be homogeneously distributed as there is no distinct fluorescent intensity change within the observation area. Referring to the coupling amount, the waveguide polymer has the highest absorption to IgG, and then to BSA and, Lys. This probably has its origin in the different molecular weights of proteins.

- *The influence of the solution environment on the protein coupling*

We investigated the influence of the solution environment on the protein coupling onto the waveguide polymer surface. The results are shown in Fig. 5.15. Neither the alkalescent solution environment (carbonic acid buffer, pH 10) nor the acid solution environment (citric acid buffer, pH 3.2) has a dramatic impact on the protein coupling. This proves that the electrostatic interaction is not the dominant factor, and thus has no substantial impact during the process of protein immobilization. However, a higher ionic strength can enhance the protein absorption process. This can be seen from the better IgG absorption result, which was achieved after 0.5 M NaCl was added to the PBS of pH 7.4. The incorporation of NaCl will help reduce the hydration effect on the surface of the protein, promoting the preservation of its partial hydrophobic surface. Thus, the hydrophobic coupling pushed by the entropy driving effect is proved here again to play the dominant role in protein coupling onto the polymer waveguide surfaces.

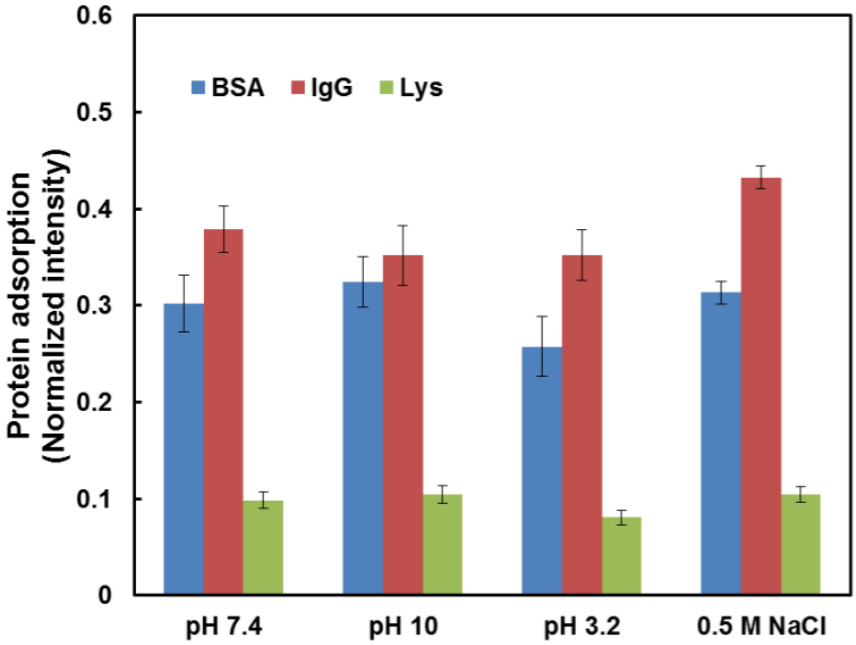

Fig. 5.15 The influence of the solution environment on the protein coupling. (The solutions are 0.02 M PBS (pH 7.4, 0.154 M NaCl), 0.1 M carbonic acid buffer (pH 10), 0.1 M citric acid buffer (pH 3.2), 0.02 M PBS (pH 7.4, 0.5 M NaCl). Proteins are all with concentration of 0.5 mg/mL. Polymer coated silicon samples were incubated with protein solutions for 1 hour at 37 ˚C, then transferred to a refrigerator, incubating for 12 hours at 4 ˚C. Finally, they were rinsed repeatedly with PBS with pH7.4 and DI water, and dried by nitrogen gas finally.)

- *Determination of Protein Adsorption on PA-coated Polymer Slides*

Antibody research is of high importance in life sciences because of its unique capability of identifying and neutralizing foreign objects such as bacteria and viruses. As a first step towards specific antigen-antibody sensing, we demonstrate sensing of surface binding in this work. To this end, the waveguide surface needs to be treated to have receptors with binding sites immobilized on it. In this work, IgG (human Immunoglobulin G) and PA (Staphylococcal protein A) are chosen as an affinity model. High affinity of IgG towards protein A but with moderate dissociation constant (10^{-6} M) makes it a

much more representative model than the widely used biotin-avidin one, whose dissociation constant is as high as 10^{-15} M.

Although protein immobilization onto the surface of the polymer waveguide has been proved to be feasible previously, one critical issue still hasn't been answered. As we know, there exists a possibility that the molecular structure of the proteins can be changed when they are coupled to the polymer surface with their partial hydrophobic surface. If such a conformation change happens on the functional area of the proteins, then the bioactivity of the immobilized bioreceptors will be severely affected.

In order to prove that the immobilized protein bioreceptors still keep the bioactivity, PA-coated polymer slides were prepared with the same approach as mentioned above, except that Protein A was employed as coating molecule. The coated polymer slides were immersed in three different solutions, containing BSA-FITC, IgG-FITC and Lys-FITC to evaluate its adsorption selectivity towards IgG. The solutions of proteins in PBS were prepared at a concentration of 0.5 mg/mL, and each solution was incubated with a PA-coated polymer slide for 10 min at room temperature. Then, the slide was rinsed carefully with PBS and dried with nitrogen for the detection of fluorescence signals. BSA-coated polymers were also prepared and tested for comparison. The experimental results are shown in Fig. 5.16.

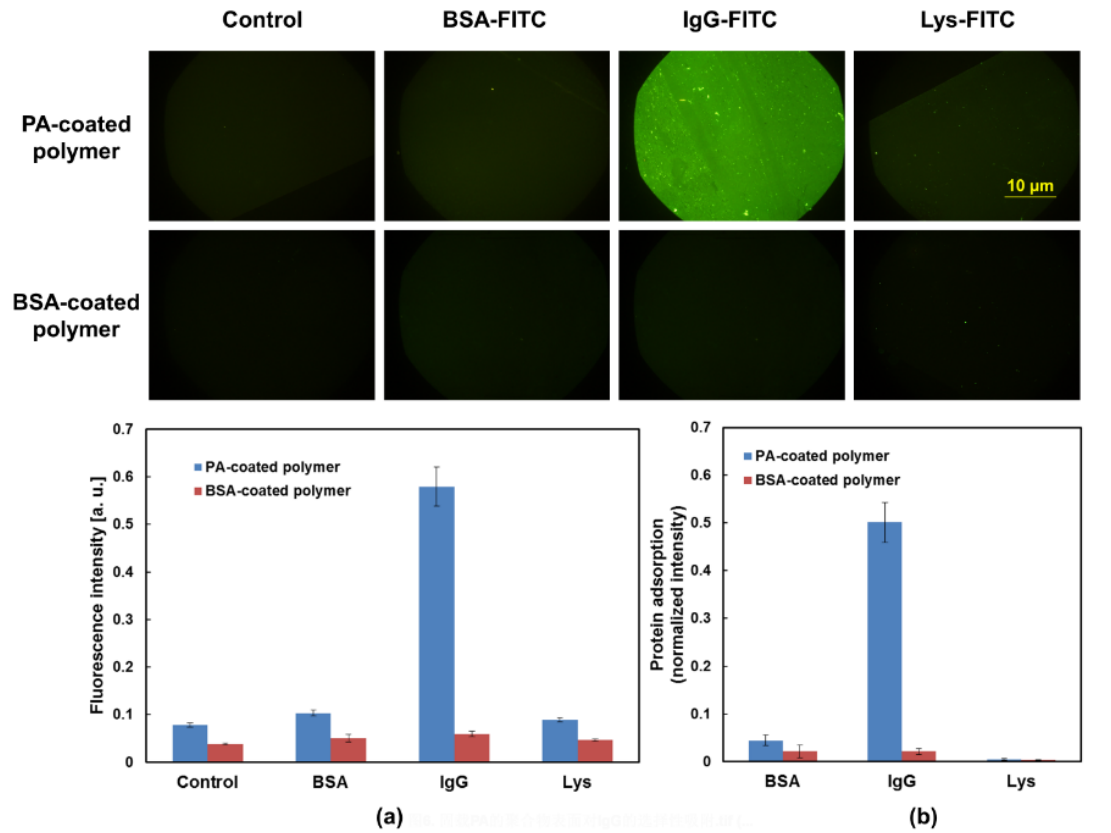

Fig. 5.16 Selective adsorption of IgG on PA-coated polymer surface.

PA-coated polymer slides (upper row) and BSA-coated polymer slides (lower row) were incubated with PBS, BSA-FITC, IgG-FITC and Lys-FITC conjugate solutions (from left to right) for 10 min at room temperature. All fluorescence micrographs were taken under identical conditions: magnification 100×, exposure time 1/7 s. The fluorescence intensity of each image was analyzed quantitatively (a) and normalized (b) by removing the effect of fluorescence background and considering the individual F/P mass ratio of each protein, which allow a direct comparison of the coupling amount between different proteins.

From the experiments, it can be concluded that the hydrophobicity is not so high as to essentially affect the conformation and function of the retained proteins. Under physiological solution conditions (0.01 M PBS, pH7.4, containing 0.154 M NaCl), PA molecules were coated on the surface of polymer slides effectively through an incubation process. The further

characterization with a fluorescence analysis found that the resultant PA-coated chip had a good performance in binding its affinity target, human-IgG, while its binding capacities towards two other proteins, BSA and Lysozyme, were not significant compared to the control that employ BSA as immobilized protein. The results in Fig. 5.16 indicated that the immobilization of PA did not lead to a significant loss of IgG-binding activity. More important, since PA has a relatively small molecular size and a less complex spatial structure, the protein layer had a good coverage on the surface of the polymer. Thus, the surface area that could accommodate other proteins and result in nonselective adsorption was limited. Therefore, surface functionalization through physical immobilization has been proved to be effective enough for the fabricated optical chip. Its good performance on PA coupling makes it a good alternative for antibody oriented immobilization.

- *The conservation of the optical chips coated with protein A*

The stability of the bio-function of optical biosensors is without doubt important during their conservation. In order to evaluate this, several samples were coated with protein A under the same conditions and then kept under room temperature for 7, 30 and 50 days separately. After that, the bioactivity of these samples is judged by incubating them with an IgG solution. The result is shown in Fig. 5.17. It can be seen that there are almost no changes in the coupling capability towards IgG for these samples. Thus, there would be no problem for the functionalized optical biosensors to be kept until utilizing them to immobilize antibodies.

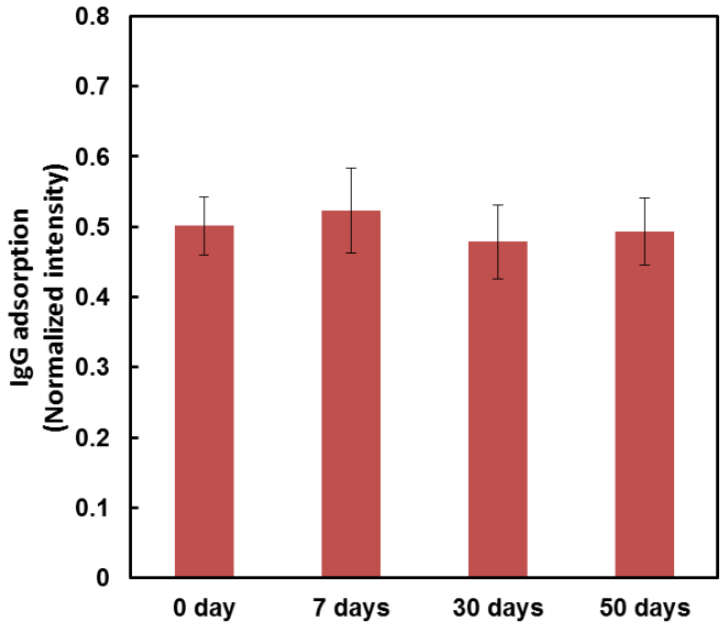

Fig. 5.17 The change of the bio-activity of the prepared PA-coated sample with time.

5.4 Integration of the microfluidic channel with the functionalized optical chip

Once the optical chip is surface functionalized, how to deliver the sample solution to the right point where the transducer is located needs to be considered. Since in our case most of the analytes are distributed within the buffered solution, the microfluidic channel that is capable of manipulating the fluidic flow becomes a good candidate. Easy planar integration with the optical chip is its advantage. However, some special issues during integration have to be paid attention to. Especially, since our optical chips have already been surface functionalized, commonly used processes such as oxygen plasma or thermal heating at high temperature carried directly to the chips should be avoided. Any of them will cause the loss of bioactivity of the bioreceptors immobilized on the chips.

In this work, a room temperature integration technology suitable for bonding a microfluidic channel and a polymer waveguide optical chip is

adapted, which is also known as “stamp-and-stick” [23]. Essentially speaking, it is a glue method. The process is shown in Fig. 5.18. First, the microfluidic channel is obtained from an SU-8 master mold by the casting method. The detailed fabrication process has been introduced in section 3.3.1 of chapter 3, and will thus not be repeated here. Only because the width of the channel is designed to be a little bit larger in order to fit the relatively large ring resonator, its height should be adjusted to prevent the collapse of the channel, which will be explained below. After punching the inlet and outlet holes, the fluidic channel is carefully cleaned. 2 minutes of oxygen plasma treatment will dramatically change its surface property from hydrophobic to hydrophilic. Secondly, this fluidic channel is gently pressed against a silicon substrate which has a thin film of UV curable resin spin coated on it. Since the height of the flow channel is much higher than that of the resin film, after releasing them, the resin will remain only on the supporting parts of the fluidic channel rather than inside it. In the next step, the functionalized optical chip will be brought closer to this flow channel. They are brought in contact with each other after aligning the ring resonator in the center of the flow channel. UV light is illuminated from the top to cure the still wet resin layer. In this way, the fluidic channel and functionalized optical chip are bonded together. Finally, two polytetrafluoroethylene (PTFE) tubes are inserted into the inlet and outlet holes punched earlier to flow the solution.

Two special issues need to be paid attention to during the process. The first is the right choice of the resin. As can be seen from the above process, the resin plays a role as a glue. Thus its UV curing property should be good enough, allowing us to avoid thermal curing, which is detrimental to the biomolecular layer. More importantly, once it is UV cured, it would be ideal that no remaining chemical solvents would still be released from the resin. Such solvents are very harmful as they can also be detected by biosensor. The misreading of the signals by the biosensor is difficult to be interpreted. Besides that, the refractive index of the resin is also very important. With this method, most of the channel waveguides except the ring resonator waveguide will be covered by the resin, which actually acts as the upper cladding of

polymer waveguide. Thus the refractive index of the resin should be well below that of the waveguide core, which is 1.52. After several experiments, we found the properties of a kind of epoxy named OG-134 (Epoxy Techonology, Inc) to meet the above requirements well and considered the epoxy a suitable choice.

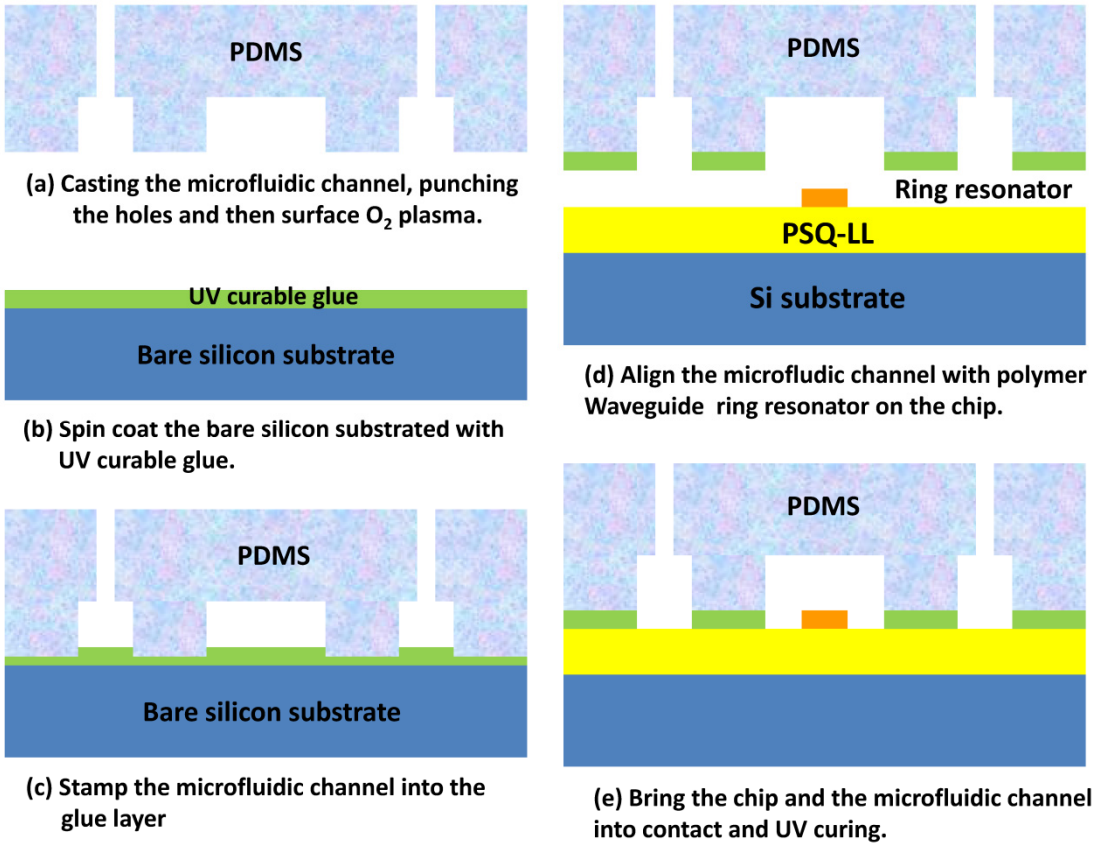

Fig. 5.18 The fabrication process of “stamp-and-stick” for bonding microfluidic channel with polymer waveguide chip.

The second problem is related to the height of the fluidic channel. The width of the fluidic channel cannot be too small since the ring resonator is designed to have relatively large radius. This means that the fluidic channel is working under the regime of low aspect ratio. Even for this, the height of the fluidic channel is still preferred to be larger. Too small height value will cause a jam of the channel. An example is shown in Fig. 5.19(a), in which the channel width is around 2 mm, while its height is 50 μm. As can be seen, the

UV resin jams the flow channel that should be free. The reason is the deformation of the elastic channel during bonding under force. Sagging of the channel in the middle is the main deformation type. The resin squeezed by the supporting parts of the channel tends to be attracted by its sagging part under the capillary force. By experiment, this jam can be effectively prevented when increasing the height of the flow channel above 100 μm, which is achieved by thickening the SU-8 50 master mold. This is shown in Fig. 5.19(b). A typical biosensor assembled with a fluidic channel and connected to a syringe is shown in Fig. 5.20.

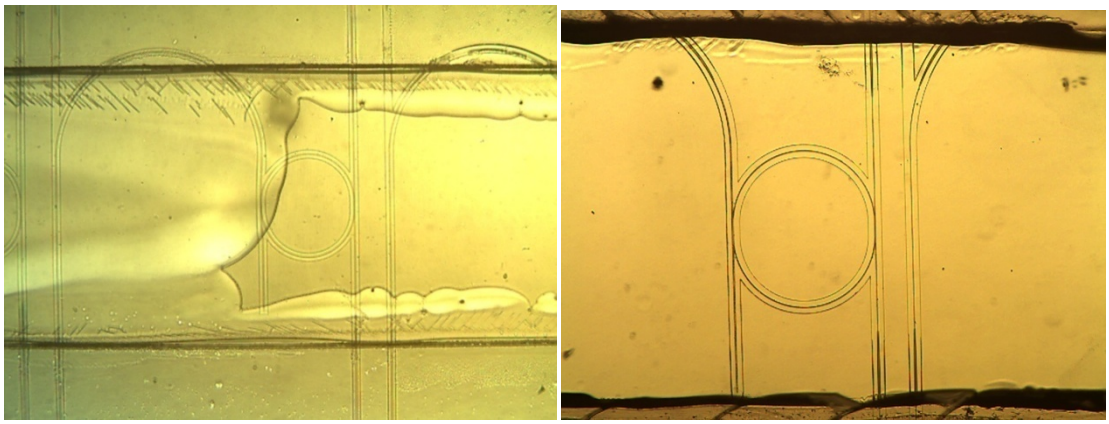

(a) (b)

Fig. 5.19 The fluidic channel aligned with the ring resonator on the chip and sealed with OG-134. (a) Jam of the channel. (b) Free of the channel.

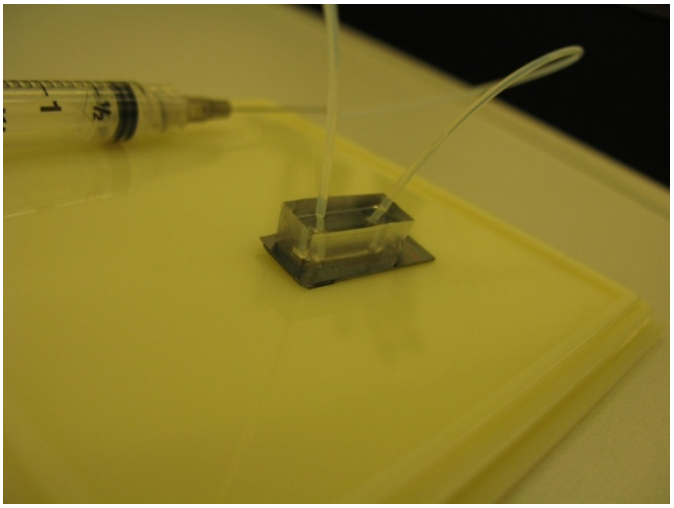

Fig. 5.20 A typical biosensor assembled with fluidic channel and connected to a syringe.

5.5 **Measurement setup**

The built measurement setup is shown in Fig. 5.21. The main construction is the same as that used for passive devices' measurement: the light from a tunable laser is coupled into the input waveguide of the ring resonator via a lensed fiber. The output signal is collected by an objective, and focused onto an infrared CCD camera or photo detector. A polarization controller at the input side and a polarizer at the output side are used to tune the polarization state (this can also be seen in Fig. 3.19 in chapter 3). However, as analyzed in section 5.2.7, the resonant wavelength of the polymer ring resonator has a high temperature dependence (~200 pm/˚C), which is unacceptable for biosensing using wavelength interrogation. Thus a home-made temperature stabilized chunk, utilizing the peltier effect is built and mounted onto the sample stage. With a commercial temperature controller (LDX-3200 Series, ILX Lightwave, Inc.), the temperature fluctuation can be suppressed down to 0.01-0.02 ˚C. Temperature induced noise within the range of 2-4 pm can merely meet the system requirement, which is close to the practical measurement value of 3 pm. The liquid in the syringe is injected into the fluidic channel PTFE microtube with a syringe pump, of which the flow rate can be adjusted.

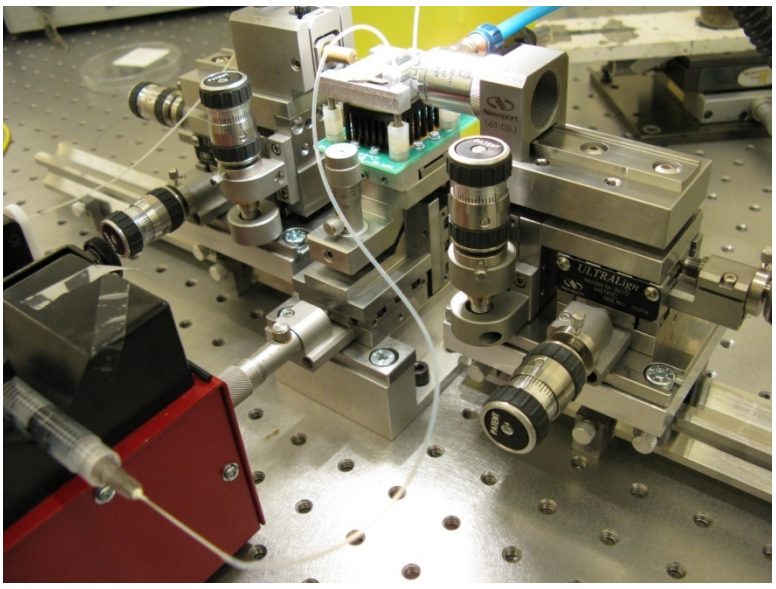

Fig. 5.21 The built setup for biosensing measurement.

5.6 **Sensing results**

5.6.1 Bulk sensing result

To demonstrate bulk sensing, a NaCl solution is chosen as the analyte to flow over the ring resonator through the fluidics channel, which serves as upper cladding of the ring resonator. The refractive index of this upper cladding is modified by the NaCl, which in turn changes the effective refractive index of the guided mode of the ring resonator and thus its resonant wavelength. The measurement result is shown in Fig. 5.22, where the correspondence between NaCl concentratons and refractive index changes is derived using the equation proposed in [24]. As expected, a higher NaCl concentration causes larger refractive index change thus resulting in larger resonant wavelength shift. The good linearity of the relationship also proves the stability of this kind of polymer during working in a NaCl solution. Around 50 nm/RIU sensitivity is obtained, slightly less than the 70 nm/RIU sensitivity achieved in [9] with a silicon microring resonator. This is due to the low refractive index of the polymer itself, which can be improved with novel nanoporous polymers as reported in [25]. However, because of the small width of the resonance achieved in Fig. 7(d), a refractive index change down to10^{-5} can still be detectable considering the 3σ noise level of around 3 pm [26].

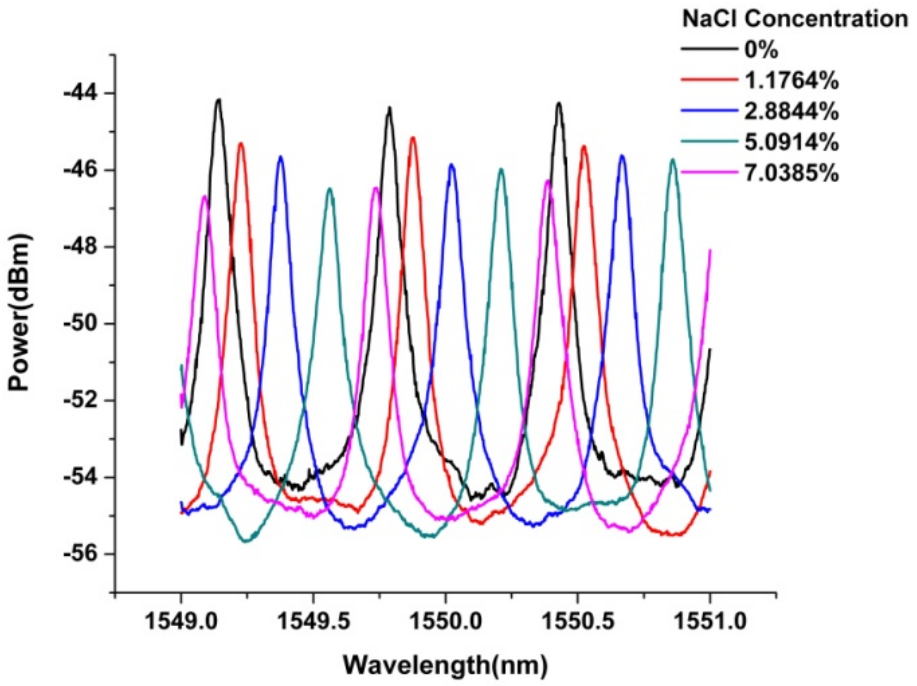

(a)

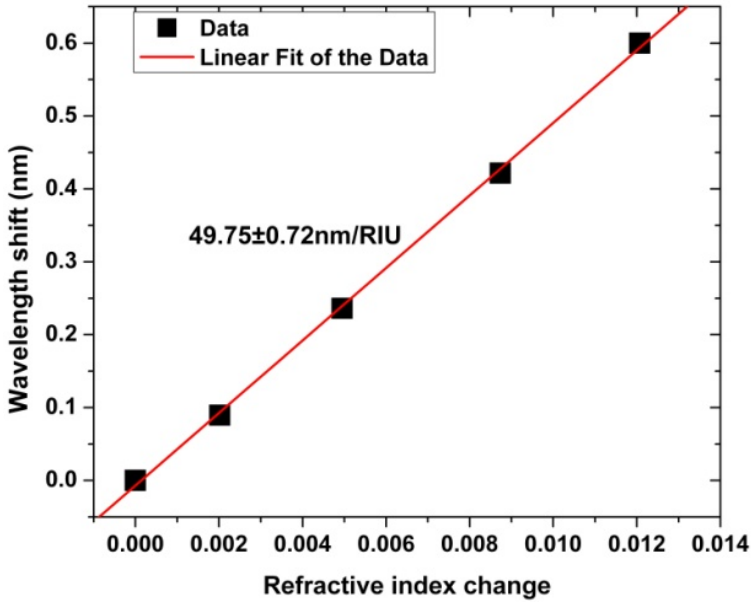

(b)

Fig. 5.22 The spectral shift of the microring resonances when flowed with NaCl solutions with different concentrations. (a) Change of the spectrum at the drop port. (b) Resonant peak positions and their linear fit.

5.6.2 Surface sensing results

DI (deionized) water, 0.01×PBS (Phosphate Buffer Solution), Human-IgG with a concentration of 50 μg/mL and 0.01×PBS are pumped into the fluidics channel consecutively, all with the flow speed of 10 μL/min. The resonant peak position, which is determined by the Lorentz fitting, is recorded as a function of the time during the process. The measurement result is shown in Fig. 5.23. As can be seen from that, the proposed polymer based optical biosensor is stable in the measurement environments, with almost zero wavelength shift in DI water in the first phase and only around 10 pm wavelength shift in PBS in the second phase. This is probably due to the ion incorporation on the functionalized surface of the polymer waveguide. It is a small enough value if compared with the dramatic wavelength shift in the third phase, where the nearly 230 pm change is caused by the affinity of human-IgG to the protein A molecules that are immobilized on the chip surface as bio-receptors. No obvious reverse wavelength shift is observed in the last phase of PBS rinsing, which indicates the strong binding strength between the protein A and human-IgG. It is also a proof that coating of protein A to the chip surface is successful. Finally, the biosensors working under different concentrations of Human-IgG solutions are tested. As can be seen in Fig. 5.24, the optical biosensors exhibit different dynamic responsivities towards the antibody concentrations. So far, the human-IgG with concentration down to 5 μg/mL can be easily detected as the signal is still significantly above the noise level. Detection with even lower antibody concentration can be expected.

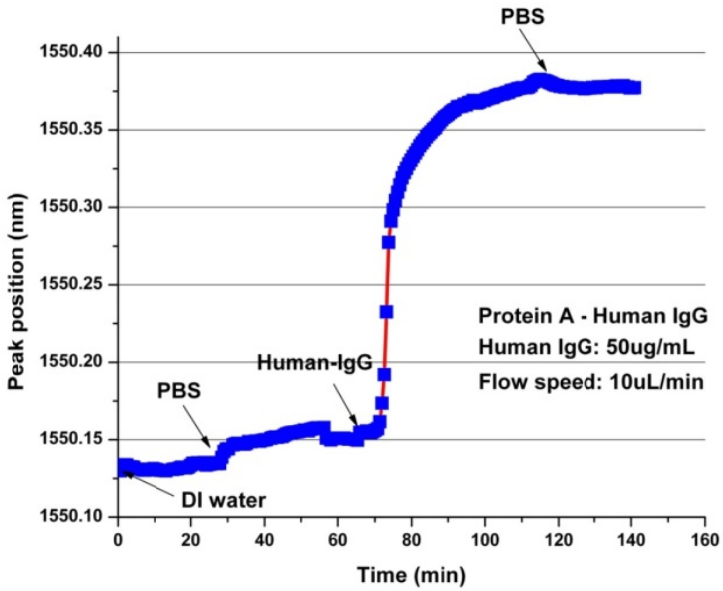

Fig. 5.23 The entire monitoring process for the surface sensing with protein A as bioreceptors immobilized on the chip surface.

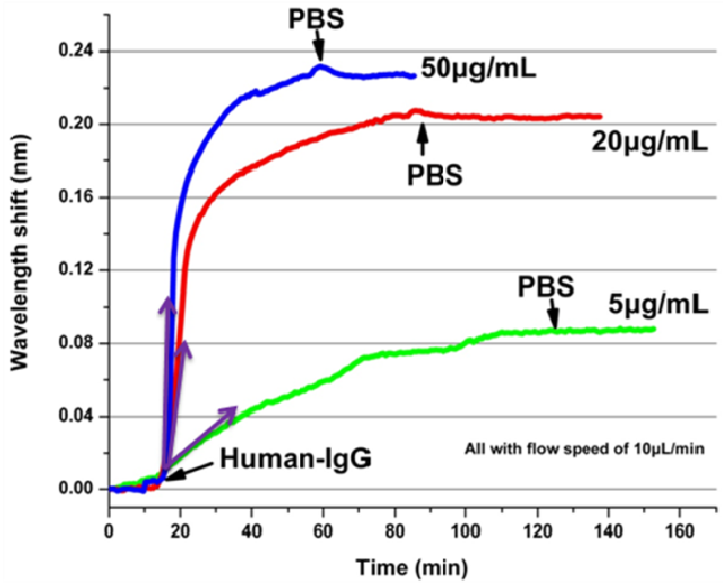

Fig. 5.24 The responsivities of the optical biosensors towards different antibody's concentrations.

5.6.3 Non-specific binding

The non-specific binding is another important aspect for the label-free optical biosensor. For the real measuring environment, besides the target analytes, usually there would exist several other types of biomolecules at the same time. The anchor of these non-specific biomolecules onto the surface of the biosensor can also result in an optical output signal. The interference of this signal with the useful signal produced by the specific binding is harmful for the reliability of the biosensing system because it can lead to signal misreading, especially when the useful signal is weak. In order to test our polymer-based optical biosensor's response towards the non-targeted biomolecules, BSA is chosen and brought into contact with the protein A coated optical biosensor through the fluidic channel, after the biosensor reached stability in the PBS. The measurement result is shown in Fig. 5.25. As can be seen, there is a resonant wavelength shift of around 40 pm caused by the non-specific binding of the BSA molecules, where the saturation is reached after 40 minutes with the injection of the BSA solution. The concentration of the BSA in PBS for the test is 50 μg/mL. Besides that, there is no apparent signal change after the PBS flow over again the optical biosensor, which indicates that the BSA molecules get absorbed onto the surface of biosensor and cannot be washed away by the PBS. Although the resonant wavelength shift of 40 pm caused by the BSA with a concentration of 50 μg/mL is still smaller than that of 90 pm by specific binding of the human-IgG with a concentration of 5 μg/mL (see Fig. 5.24), it has to be admitted that currently our biosensor's response towards the non-specific binding is still not sufficiently low and further improvement is needed. In fact, after the surface functionalization of the optical chip with protein A, BSA can be used as an efficient blocking protein to take up the residual binding sites, which can reduce the non-specific binding of the unwanted proteins during the subsequent surface sensing experiment.

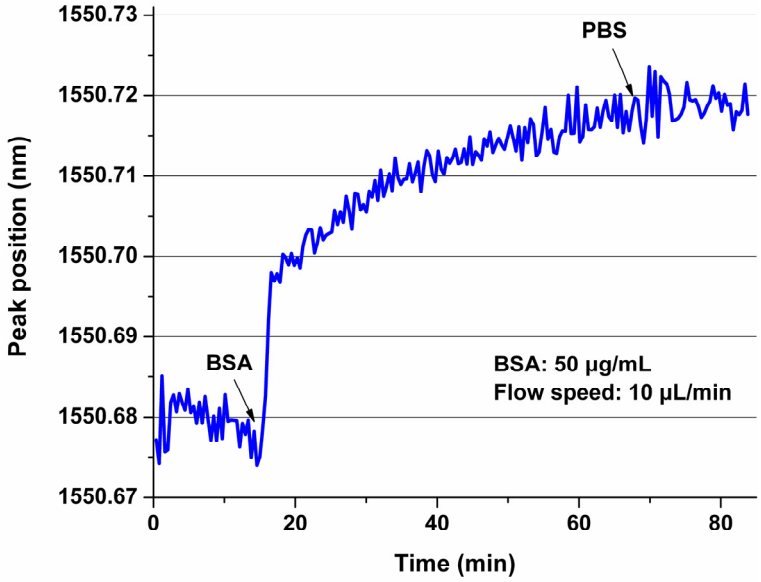

Fig. 5.25 The response of the optical biosensor functionalized with protein A towards the non-specific BSA molecules.

5.7 **Conclusion**

Based on a the developed simple UV-based soft imprint technique, ring resonators with very high Q value were obtained with one step imprinting, using the novel polysiloxane liquid optical material PSQ-Ls, which were then used as optical biosensor. The bulk sensing experiment with NaCl solutions shows such a ring resonator has a sensitivity of 49.75 nm/RIU. After the investigation of the physicochemical and chemical properties of the interface, a simple but efficient method to immobilize the bio-receptors onto the surface of the optical chip, which is protein A in our case, was developed. Surface biosensing was demonstrated with protein A's affinity pair, human-IgG. The biosensor's response towards the non-specific binding of the biomolecules was also tested. Our study confirms the possibility that polymer based optical biosensors with surface functionality can perform well in an aqueous environment. Considering the constituents that are included within this work, ranging from material, fabrication technique to surface functionalization method, a very low cost optical biosensor built on a polymer platform is

promising, which would find vast applications in the fields of environmental monitoring, food safety, and diagnostic applications.

5.8 References

[1] X. Fan, I. M. White, S. I. Shopoua, H. Zhu, J. D. Suter, and Y. Sun, “Sensitive optical biosensors for unlabeled targets: A review,” Anal. Chim. Acta. 620, 8–26 (2008).

[2] W. Bogaerts, P. De Heyn, T. Van Vaerenbergh, K. De Vos, S. Selvaraja, T. Claes, P. Dumon, P. Bienstman, D. Van Thourhout, and R. Baets, “Silicon microring resonators,” Laser Photon. Rev. 6, 47–73 (2012).

[3] M. Iqbal, M. A. Gleeson, B. Spaugh, F. Tybor, W. G. Gunn, M. Hochberg, T. Baehr-Jones, R. C. Bailey, and L. C. Gunn, “Label-free biosensor arrays based on silicon ring resonators and high-speed optical scanning instrumentation,” IEEE J. Sel. Top. Quantum Electron. 16, 654–661 (2010).

[4] P.P.P. Debackere, S. Scheerlinck, P. Bienstman, R. Baets, “Surface plasmon interferometer in silicon-on-insulator: novel concept for an integrated biosensor,” Opt. Express 14, 7063-7072 (2006).

[5] K. Quang Le, P. Bienstman, “Enhanced Sensitivity of Silicon-On-Insulator Surface Plasmon Interferometer with Additional Silicon Layer,” IEEE Photon. J. 3, 538-545 (2011).

[6] A. Abbas, M. J. Linman, and Q. Cheng, "Sensitivity Comparison of Surface Plasmon Resonance and Plasmon-Waveguide Resonance Biosensors" Sens. Actuators B, Chem. 156, 169-175 (2011).

[7] M. I. Lapsley, I.-K. Chiang, Y. B. Zheng, X. Ding, X. Mao, and T. J. Huang, "A single-layer, planar, optofluidic Mach-Zehnder interferometer for label-free detection," Lab Chip 11, 1795-1800 (2011).

[8] R. Bruck, E. Melnik, P. Muellner, R. Hainberger, and M. Lämmerhofer, "Integrated polymer-based Mach-Zehnder interferometer label-free streptavidin biosensor compatible with injection molding," Biosens. Bioelectron. 26, 3832-3837 (2011).

[9] K. De Vos, I. Bartolozzi, E. Schacht, P. Bienstman, and R. Baets, “Silicon-on-insulator microring resonator for sensitive and label-free biosensing,” Opt. Express 15, 7610–7615 (2007).

[10] J. B. Wright, I. Brener, K. R. Westlake, D. W. Branch, M. J. Shaw, and G. A. Vawter, “A platform for multiplexed sensing of biomolecules using high-Q microring resonator arrays with differential readout and integrated microfluidics,” Proc. SPIE 7605, 76050C1-11 (2010).

[11] T. Claes, W. Bogaerts, and P. Bienstman, “Experimental characterization of a silicon photonic biosensor consisting of two cascaded ring resonators based on the Vernier-effect and introduction of a curve fitting method for an improved detection limit,” Opt. Express 18, 22747-22761 (2010).

[12] A. Ramachandran, S. Wang, J. Clarke, S. J. Ja, D. Goad, L. Wald, E. M. Flood, E. Knobbe, J. V. Hryniewicz, S. T. Chu, D. Gill, W. Chen, O. King, and B. E. Little, “A universal biosensing platform based on optical micro-ring resonators,” Biosens. Bioelectron. 23, 939–944 (2008).

[13] A. Yalcin, K. C. Popat, J. C. Aldridge, T. A. Desai, J. Hryniewicz, N. Chbouki, B. E. Little, O. King, V. Van, S. Chu, D. Gill, M. Anthes-Washburn, M. S. Unlu, and B. B. Goldberg, “Optical sensing of biomolecules using microring resonators,” IEEE J. Sel. Topics Quantum Electron. 12, 148–155 (2006).

[14] C. Y. Chao, W. Fung, and L. J. Guo, "Polymer Microring Resonators for Biochemical Sensing Applications," IEEE J. Sel. Toptics Quantum Electron. 12, 134-142 (2006).

[15] Katrien De Vos, PhD thesis, “Label-Free Silicon Photonics Biosensor Platform with Microring Resonators,” Ghent university, Ghent, Belgium (2010).

[16] E. Ozkumur, A. Yalcin, M. Cretich, C. A. Lopez, D. A. Bergstein, B. B. Goldberg, M. Chiari, and M. S. Unlu, “Quantification of DNA and protein adsorption by optical phase shift,” Biosens. Bioelectron. 25 167-172 (2009).

[17] P. I. Nikitin, B. G. Gorshkov, E. P. Nikitin, and T. I. Ksenevich, “Picoscope, a new label-free biosensor,” Sens. Actuators B, Chem. 111, 500–504 (2005).

[18] Z.-H. Wang and G. Jin, "Covalent immobilization of proteins for the biosensor based on imaging ellipsometry," J. Immunol. Methods 285, 237-243 (2004).

[19] Z. Wang and G. Jin, "Feasibility of protein A for the oriented immobilization of immunoglobulin on silicon surface for a biosensor with imaging ellipsometry," J. Biochem. Biophys. Methods 57, 203-211 (2003).

[20] K. De Vos, J. Girones, S. Popelka, E. Schacht, R. Baets, and P. Bienstman, “SOI optical microring resonator with poly(ethyleneglycol) polymer brush for label-free biosensor applications,” Biosens. Bioelectron. 24, 2528-2533 (2009).

[21] S. L. Hirsh, M. M. Bilek, N. J. Nosworthy, A. Kondyurin, C. G. dos Remedios, and D. R. McKenzie, “A comparison of covalent immobilization and physical adsorption of a cellulase enzyme mixture,” Langmuir 26, 14380-14388 (2010).

[22] F. Rusmini, Z. Zhong, and J. Feijen, “Protein immobilization strategies for protein biochips,” Biomacromol. 8, 1775-1789 (2007).

[23] S. Satyanarayana, R. N. Karnik, and A. Majumdar, “Stamp-and-stick room-temperature bonding technique for microdevices,” IEEE J. Microelectromech. Syst. 14, 392–399 (2005).

[24] H. Su and X. G. Huang, “Fresnel-reflection-based fiber sensor for on-line measurement of solute concentration in solutions,” Sens. Actuators B, Chem. 126, 579–582 (2007).

[25] M. Mancuso, J. M. Goddard, and D. Erickson, “Nanoporous polymer ring resonators for biosensing,” Opt. Express 20, 245–255 (2012).

[26] I. M. White and X. Fan, “On the performance quantification of resonant refractive index sensors,” Opt. Express 16, 1020–1028 (2008).

Chapter 6 A polymer-based surface grating coupler

6.1 Introduction

Coupling light into or out of the integrated optical waveguides remains to be a big challenge, which is faced by both inorganic and organic waveguides. The traditional route of edge coupling using optical fiber is one of the choices, which however, suffers from several disadvantages such as high requirement for good waveguide facets decided by polishing process, poor tolerance on the alignment, susceptibility to mechanical vibrations and so on.

Recently, surface grating couplers fabricated directly on the access waveguides represent another alternative for light coupling [1, 2]. This component avoids many of the disadvantages brought by edge coupling mentioned above. Moreover, they have a small footprint, which can be freely placed anywhere on the entire chip surface. Such feature greatly facilitates the layout design of the photonic circuit and the device testing. It is highly desirable if the low-cost and disposable photonic device such as optical biosensors can be assembled with these surface grating couplers. As currently most integrated optical biosensors still rely on off-chip light sources and detectors, this assembling would at least provide two benefits. First, biosensors with different functionalized surfaces accommodated on the same chip can be accessed at the same time, thus making multiplexed sensing possible. Second, the simplified read-out system provided by these surface grating couplers would allow the nonprofessional users out of the laboratory to use these optical biosensors more conveniently.

So far, nearly all of the research has been carried out in material platforms which offer high refractive index contrast. SOI (silicon-on-insulator) is a quite successful example in this respect. However, a similar protocol is difficult to be implemented in the polymer material platform because of the low refractive index contrast, which is usually between several hundredths and several thousandths [3, 4]. This shortage limits the application of photonic

biosensors based on polymer for multiplexed sensing, despite of the many benefits they can offer. For the limited work for polymer grating coupler, usually only the upward power diffracted out from the polymer waveguide through the surface grating coupler is shown [5]. How much power can be coupled with the optical fiber, especially single-mode fiber, is still unknown.

In this chapter, we propose a grating coupler built on the polymer platform. The coupling efficiency is enhanced by embedding a thin Si_3N_4 layer between the waveguide core and under cladding layer. Around -19.8 dB insertion loss of SMF to SMF is obtained for a straight waveguide with grating couplers at each end, which can be reduced to -17.3 dB if the output light is collected by MMF. The result indicates that the proposed grating coupler has a coupling efficiency of around 12% between SMF and polymer waveguide. The 3 dB bandwidth of the transmission spectrum is 32 nm centered at 1550 nm. For fabrication, rather than through expensive CMOS fabrication, the device is fabricated through the simple UV-based soft imprint technique.

6.2 **Basic working principle of the surface grating coupler**

The Bragg condition is the most basic equation that is used to analyze the periodic structure. It describes the relation of the wave-vectors of the incident and diffracted waves. For a uniform grating along the z-axis, such relationship is expressed as:

$$\boldsymbol{k}_z = \boldsymbol{k}_{in,z} + m\boldsymbol{K} \tag{6.1}$$

$$|\boldsymbol{K}| = \frac{2\pi}{\Lambda} \tag{6.2}$$

where Λ is the period of the grating, m is an integer representing the diffraction order. $\boldsymbol{k}_z$ and $\boldsymbol{k}_{in,z}$ are the wave vectors of the diffracted wave and incident wave respectively. Equation 7.1 and 7.2 can be used to predict at which direction the diffraction can happen. If there is no grating structure present at the interface between two materials, the Bragg condition transforms to the well known Snell's law.

For a waveguide surface grating coupler, the diffracted wave will be coupled into the guided modes of the waveguide. Thus, the diffracted wave vector is replaced by the propagation constant of the guided mode. The Bragg condition is rewritten as:

$$\boldsymbol{\beta} = \boldsymbol{k}_{in} \sin\theta + m\boldsymbol{K} \tag{6.3}$$

where $|\boldsymbol{\beta}| = \frac{2\pi}{\lambda} \cdot n_{eff}$ is the propagation constant of the guided mode in the waveguide grating, with n_{eff} the effective index of this guided mode. $|\boldsymbol{k}_{in}| = \frac{2\pi}{\lambda} \cdot n_{in}$ is the modulus of the incident wave vector, with n_{in} the refractive index of the incident media, and λ the wavelength [6].

6.3 Grating structure, simulation tools and simulation results

6.3.1 Proposed structure of polymer surface grating coupler

As mentioned before, the fundamental reason why the surface grating couplers cannot obtain a high coupling efficiency is the low refractive index of the polymer. The perturbation from the grating structures on the polymer waveguide surface has a limited influence on the waveguide mode, such that most of the light transmits directly through the waveguide instead of being diffracted out of the plane. The upward radiated power can only be increased on the condition that this perturbation is strengthened. At the same time, the field profile must also be optimized in order to increase the coupling to the fiber.

The proposed structure is depicted in Fig. 6.1. The grating pattern is fabricated on the under cladding layer, which sits on top of the Si substrate. A high refractive index layer, Si_3N_4 in our case, is selectively deposited on the grating and then embedded between the under cladding and waveguide core layer. The excess part of the Si_3N_4 layer is removed from the waveguide to prevent additional loss.

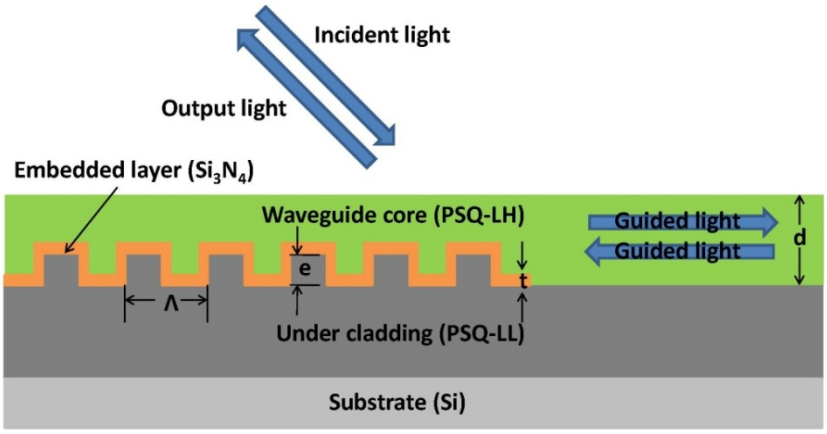

Fig. 6.1 The proposed polymer based surface grating coupler.

6.3.2 Simulation tools

The simulation is carried out with the combination of CAMFR [7] and FDTD (Finite-difference-time-domain) [8]. CAMFR is a simulation tool utilizing the eigenmode expansion method. The structure is divided into several sections and the eigenmodes of each section treated as a slab waveguide are calculated. Versatility is CAMFR's advantage. Optimization of the periodic structure can be implemented with less time and computational resource. Compared with that, the FDTD method discretizes the calculation domain with small grids. The derivatives in Maxwell's equations are transformed to finite differences in this algorithm. Fine grids are required in order to get accurate results, which however, also take up more computational time and resources.

For our application, the PML (Perfectly matched layer) condition is used as the boundary condition for both CAMFR and FDTD, which can effectively decrease or avoid the reflection at the boundaries of the calculation domain. Different transmission directions are used for these two tools. For CAMFR, the waveguide modes are excited, followed by the calculation of the electric field diffracted by the surface grating coupler. The coupling efficiency can be obtained by the overlap of this field with the fiber mode, which is a Gaussian field. In FDTD, a Gaussian field with a beam diameter of 10.4 μm is created as the incident field to the grating coupler. A detector is placed at the end of the waveguide to monitor the power of the transmitted waveguide modes,

which are coupled in by the grating coupler. A pulse source can be easily used in combination with FFT (Fast Fourier transform) to obtain the coupling spectrum of the grating coupler.

6.3.3 Simulation results

Parameters such as thickness of waveguide core *d*, thickness of the deposited Si_3N_4 layer *t*, grating height *e* and so on are optimized to obtain suitable coupling angle, higher upward power, ideal diffracted field profile and thus higher coupling efficiency with the fiber. Some optimization results are shown in Fig. 6.2. Due to the lithography resolution of the contact mask aligner, the grating period is defined as Λ =1.7 μm. Small variances on the waveguide core thickness d and deposited Si_3N_4 layer thickness *t* are taken into account, which are possible to be brought by the fabrication error. Optimal grating height is found to be between 0.6 μm and 0.7 μm, with ideal deposited Si_3N_4 layer thickness of around 0.22 μm. ~30% of the coupling efficiency can be achieved. There is around 5% difference on the coupling efficiency due to the 0.1 μm variation of the waveguide core thickness. It should be noted that the best coupling angles will also change in accordance with the grating parameters. This can be attributed to the changing of the effective refractive index of the grating waveguide during the optimization process.

The influence of the filling factor and grating number on the coupling efficiency of the grating coupler is also investigated. The results are shown in Fig. 6.3. It can be seen that 0.5 filling factor can give higher coupling efficiency, which allows easy design and fabrication as well. The coupling efficiency increases with the number of grating, but would saturate for the number more than 20. Further increasing the grating number would have little effect on the coupling efficiency. Grating number of 20 is also adopted for our design and fabrication.

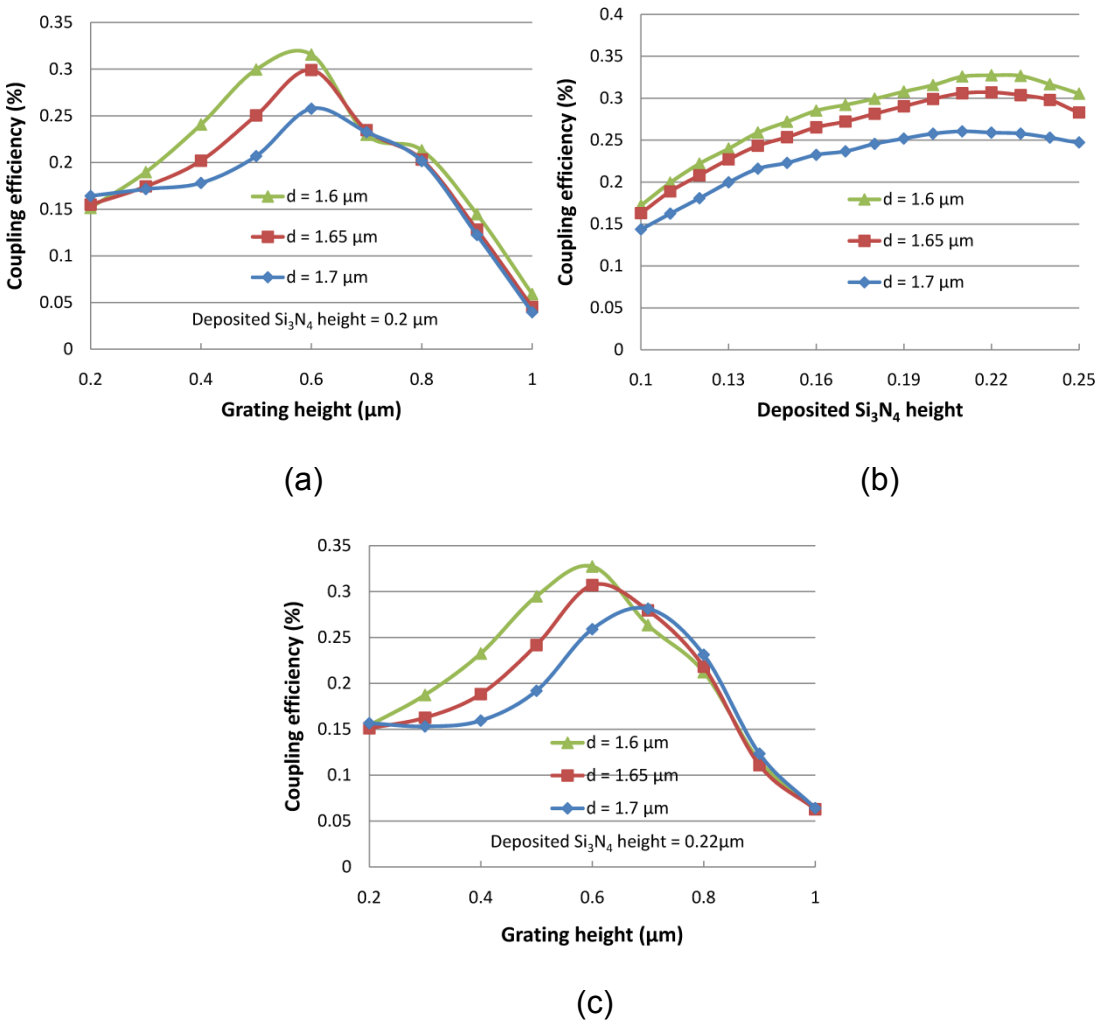

Fig. 6.2 Optimization of the grating structure (grating height, deposited Si_3N_4 height and waveguide height) using CAMFR.

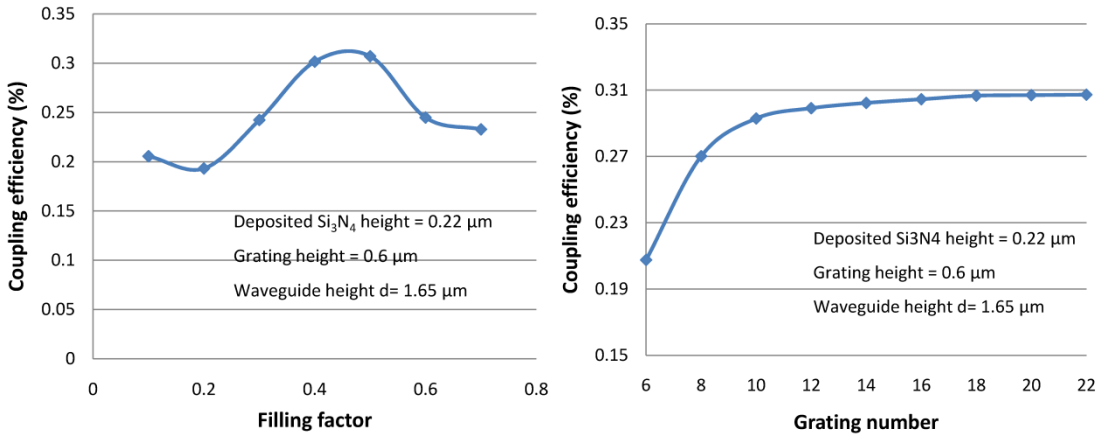

Fig. 6.3 Optimization of the filling factor and grating number using CAMFR.

The electric field plots with and without the embedded high index Si_3N_4 layer are shown in Fig. 6.4. The used parameters are as follows: thickness of waveguide core *d*=1.7 μm, grating height *e*=0.7 μm, thickness of Si_3N_4 layer *t*=0.2 μm, grating period Λ =1.7 μm. It can be clearly seen that after adding the Si_3N_4 layer, the perturbation of the surface grating on the waveguide mode is strongly enhanced, resulting in more upward power with diffraction angle around 43˚. Besides that, the near-field electric field starts exhibiting a quasi-Gaussian profile, which is more easily fitted to the standard Gaussian field profile of the optical fiber to have higher coupling efficiency. This is shown in Fig. 6.5. However, it should be noted here that the final coupling efficiency with the fiber is determined not only by the diffracted field profile itself, but also by the upward power. The optimal parameters for these two cases don't correspond with each other. A comprehensive consideration should be given to achieve higher coupling efficiency.

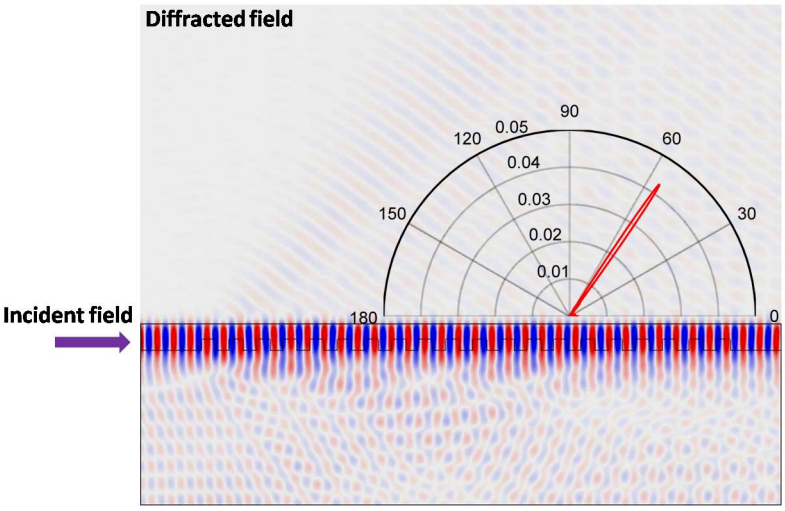

(a)

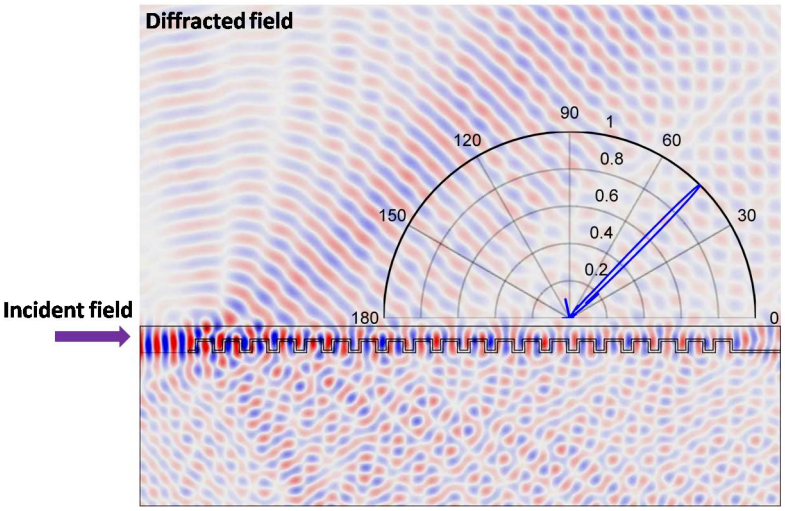

(b)

Fig. 6.4 The electric field plot without (a) and with (b) the embedded high index Si_3N_4 layer.

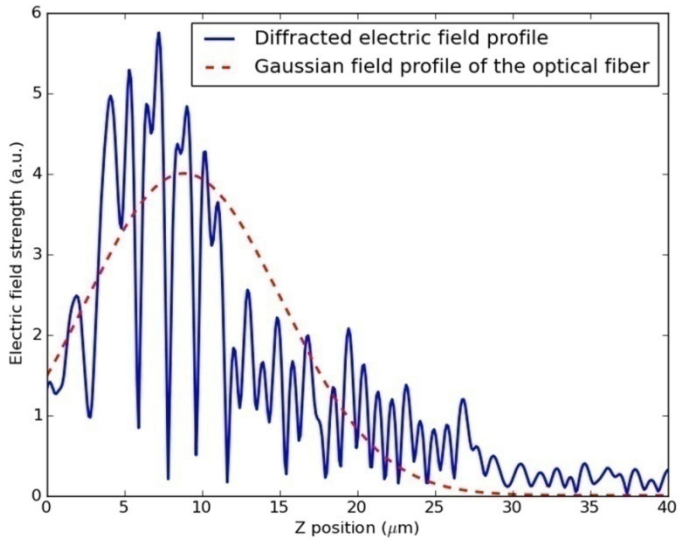

Fig. 6.5 The near field electric field profile of the proposed grating structure simulated by CAMFR.

The spectral response of the grating with the optimized structure is shown in Fig. 6.6. It shows a maximum coupling efficiency with the single-mode fiber of around 19%. Another benefit brought by this structure is polarization

selectivity. The TM mode light cannot be coupled into or out of the polymer waveguide as effectively as the TE mode light, and only has an efficiency of less than 6%.

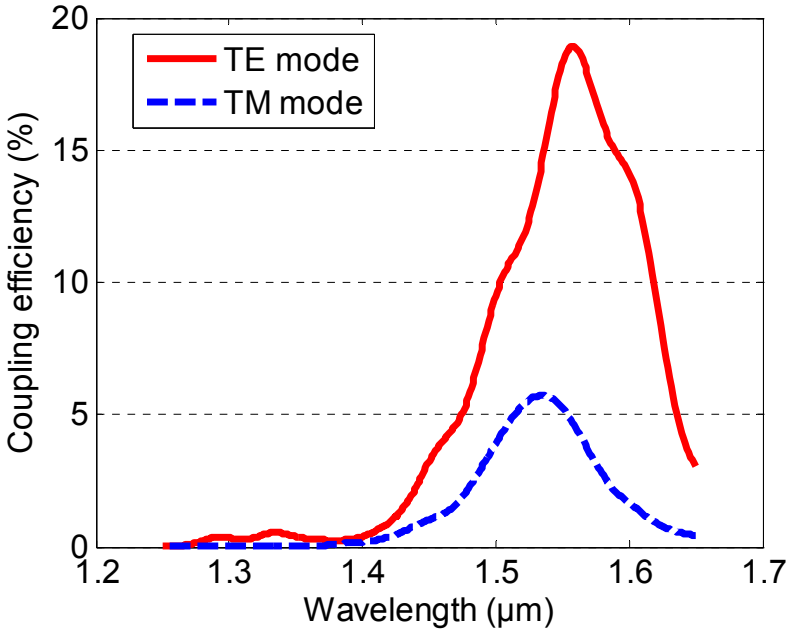

Fig. 6.6 The spectrum response of the proposed grating structure simulated by FDTD.

6.4 **Fabrication processes**

Still, the developed UV-based soft imprint technique in this thesis is used to realize the structure proposed above, rather than resorting to others. PSQ-LH with high refractive index (n=1.52) and PSQ-LL with low refractive index (n=1.45), are used as the waveguide core and cladding respectively. The fabrication process is shown in Fig. 6.7. Briefly, it starts with the fabrication of the patterned mold. The polydimethylsiloxane (PDMS) soft mold is replicated from a master mold on which the grating and waveguide patterns are defined by the contact lithography. The obtained soft mold is then pressed against the under cladding layer which is spin-coated on the silicon wafer. After 3 minutes UV light curing with an intensity of around 2000 mJ/cm^2, the soft mold is peeled from the substrate, leaving the grating and waveguide patterns on the

under cladding layer. This layer is fully cured by 2 hours of 180 ˚C thermal curing. In order to realize the selective Si_3N_4 embedded structure, first the previously obtained sample is deposited with Si_3N_4 through PECVD (Plasma-enhanced chemical vapor deposition). This step needs to be carefully optimized because our polymer cannot resist too high temperature (above 200 ˚C) during deposition. However using too low temperature is detrimental to this dielectric layer, especially since its refractive index drops dramatically, which would degrade the performance of the grating. The detailed characterization process for Si_3N_4 layer deposition is shown in Fig 6.8, where the film thickness and refractive index value are measured by ellipsometer. As can be seen, the deposition rate also drops with the temperature, which is due to the density formation change.

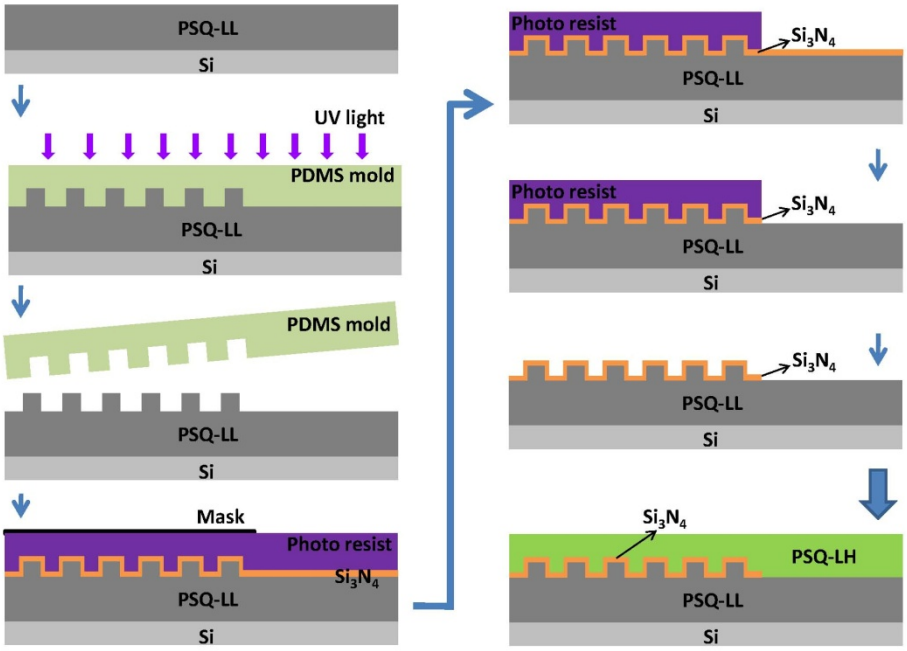

Fig. 6.7 The fabricating process of UV soft imprint lithography combined with wet etching to realize the proposed structure.

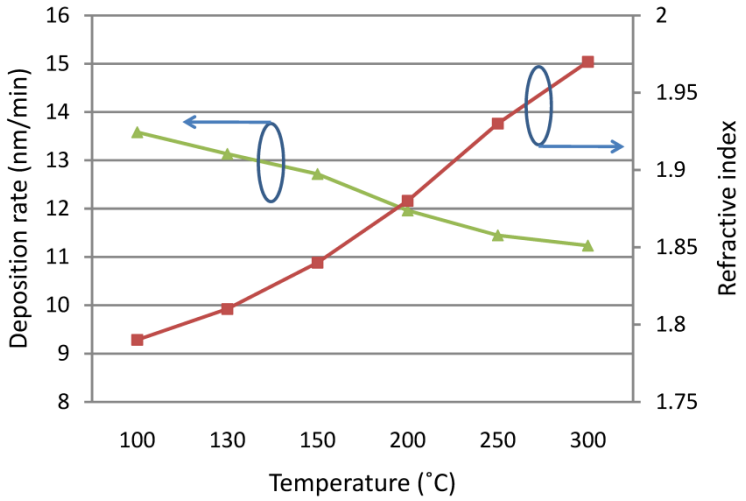

Fig. 6.8 The characterization process for the Si_3N_4 layer deposition.

By experimenting, the deposition temperature was chosen to be 150 ˚C, at which the deposition rate and refractive index are found to be 12.72 nm/min and 1.84 respectively. Targeted 200 nm layer thickness was achieved with a deposition time of around 17 min. Rather than dry etching, a simple wet etching method with a HF solution was used to completely remove the Si_3N_4 layer from the waveguide region, leaving only the grating area covered by the Si_3N_4. After the spin coating and curing of the core layer PSQ-LH, the proposed surface grating coupler structure was realized. The microscope and SEM images of the fabricated device are shown in Fig. 6.9(a) and Fig. 6.9(b).

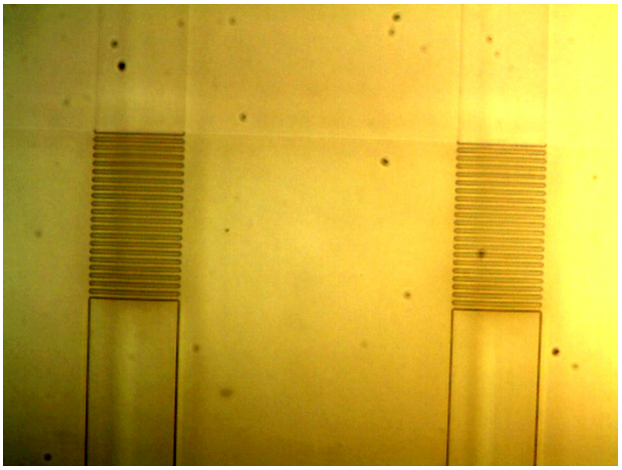

(a)

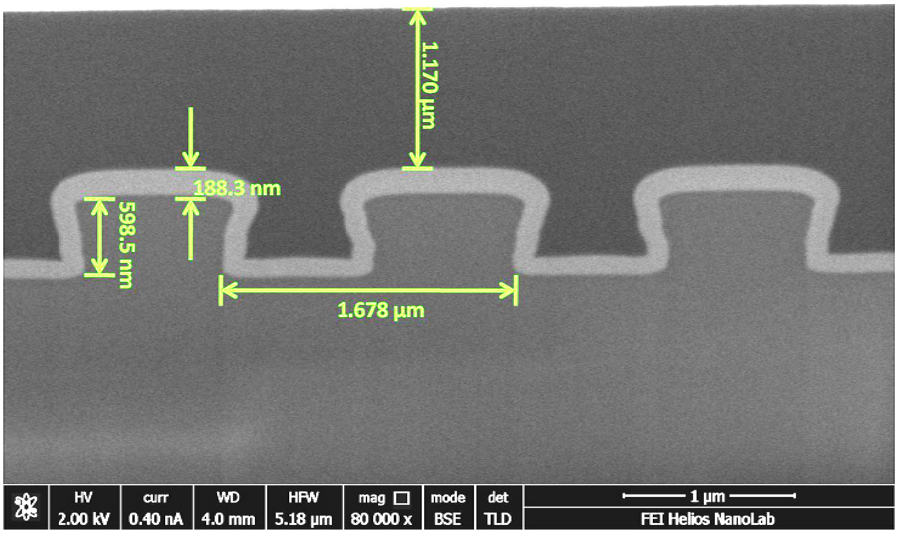

(b)

Fig. 6.9 The microscope (a) and SEM (b) picture of the fabricated surface grating coupler with Si_3N_4 layer embedded between the core and under cladding layer.

6.5 **Measurement results**

The straight waveguide with a surface grating coupler at each end is measured with a vertical setup. On this setup, a cleaved single-mode fiber connected to a tunable laser through the polarization controller was used to launch the light. The light diffracted by the surface grating coupler at the

output was collected by either a SMF or an MMF, which was connected to an optical power meter. The input and output fibers are mounted on high-precision 3-axis translation stages, on which they can be tuned between 36˚ and 45˚ with respect to the vertical direction using a rotation arm. The sample is mounted on a vacuum chuck on a two-axis stage. Both the tunable laser and power meter are controlled by a computer. The measurements result is shown in Fig. 6.10. The optimal coupling angle was found to be 40˚. At this angle, around -19.8 dB SMF to SMF insertion loss is obtained. We measured the straight waveguide loss with a similar inverted-rib structure through Fabry-Perot resonance method before and it was found to be 1.7 dB/cm [9]. In this case the length of the straight and tapered waveguides connecting the two surface grating couplers is 5 mm, resulting in an estimated transmission loss of 0.85 dB. The pure link loss is measured to be 0.42 dB at 1550 nm wavelength. Thus the coupling efficiency for each surface grating coupler can be determined to be -9.27 dB (nearly 12%) conservatively. There are another two factors we still have not taken into account because they are currently difficult to predict. One is the junction loss from the grating coupler to the waveguide and the other is the surface reflection loss. Considering this, the actual coupling efficiency can be even higher. The 3 dB bandwidth is 32 nm centered at 1550 nm. MMF was also used to receive the output power. Because of the large aperture of the MMF, the total SMF to MMF insertion loss was reduced by 2.5 dB, which is -17.3 dB.

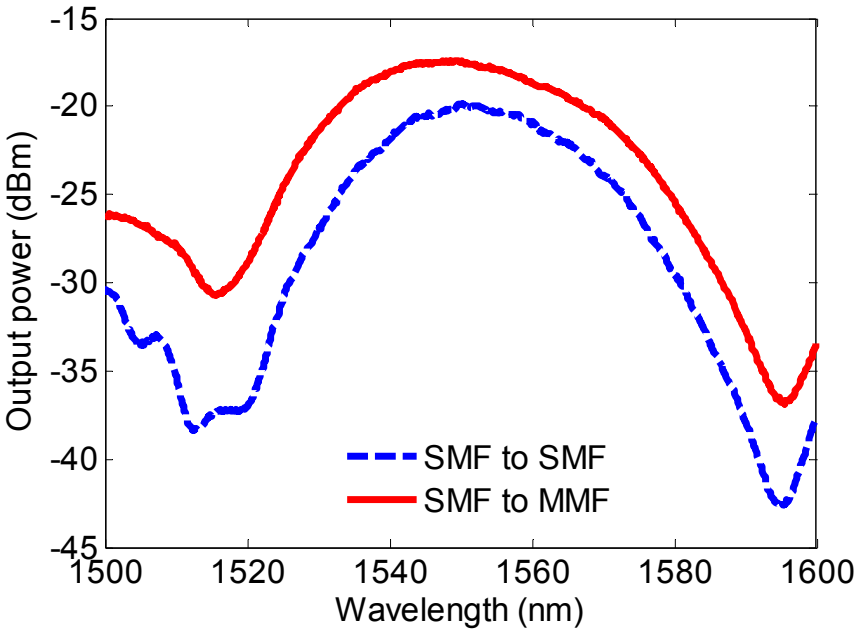

Fig. 6.10 The measured fiber to fiber transmission spectrum of the straight waveguide with a grating coupler at each end.

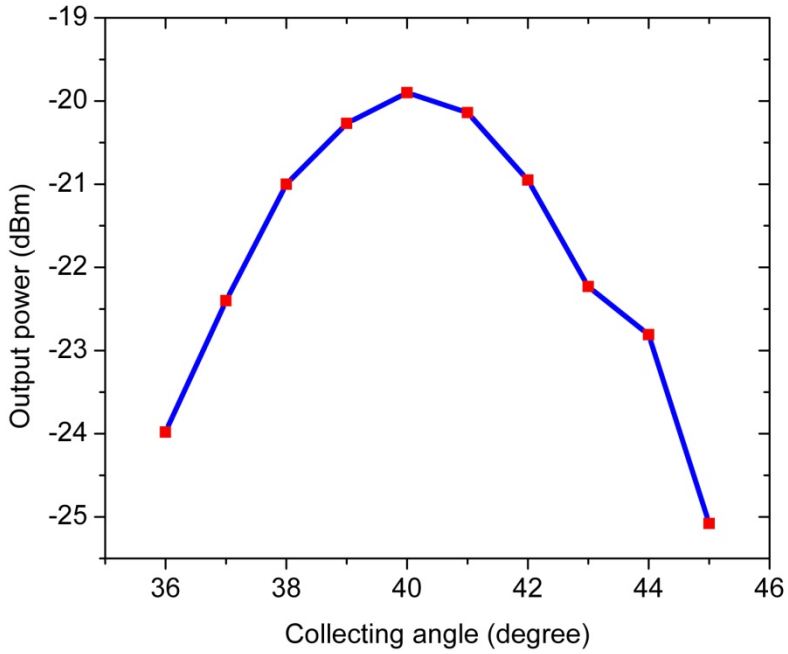

Fig. 6.11 The change of the maximum output power with the angle of the SMF at the output end.

In order to find out how the energy is distributed within the first order of the proposed surface grating coupler, we carefully tune the angle of the output SMF while keeping that of the input SMF at 40˚. The measured result is shown in Fig. 6.11. The 3dB angle bandwidth is around 7˚. This result confirms that the first order is the main order of such grating coupler. The small energy distributed angle also shows the possibility of imaging the output light onto an infrared camera in the far field.

Although the feasibility of coupling between fiber and polymer waveguide has been demonstrated for the first time, it has to be admitted that so far its coupling efficiency is still not as high as that predicted by the simulations, which can be attributed to several possible factors during fabrication. The first important one is the highly accurate control of the under cladding thickness. Currently this cannot be achieved with a simple spin coating process. Many studies have shown that the coupling efficiency of a surface grating coupler would fluctuate severely with this buffer layer thickness. The downward propagating wave created by the grating would be reflected by the interface of the under cladding and the silicon substrate. The constructive or destructive interference between the reflected wave and the direct upward wave by the grating determines the final coupling efficiency. To deal with this problem we increase the thickness of the under cladding layer as much as possible (above 8μm). Although it can mitigate the fluctuation to some extent, the most ideally optimized coupling efficiency cannot be achieved. The second important reason can be caused by the lower refractive index of the Si_3N_4, which has close relationship with the deposition temperature during fabrication. With 150 ˚C deposition temperature, the refractive index of Si_3N_4 was measured to be 1.84, rather than the expected 2.0, which degrades the performance of the grating coupler. As the enhancement mechanism has been proven apparently within this work, further efforts can be made on the following aspects:

- Optimize the fabrication process to increase the refractive index of this enhancement layer. Replacing Si_3N_4 with other materials possessing higher refractive index such as TiO_2 can be a solution [10].

- Effectively suppress the scattering loss at the abrupt transition from the polymer waveguide to the Si_3N_4 deposited grating. Appropriate changing the filling factor of the first tooth of the grating at this transition point can be a possible solution [11].
- Improve the mold quality to obtain a grating profile more close to the rectangular shape.

6.6 **Conclusion**

In this chapter, a surface grating coupler based on a polymer platform is proposed. A high refractive index layer of Si_3N_4 is embedded between the under cladding and waveguide layer to obtain good directionality and higher coupling efficiency with the fiber. Rather than expensive CMOS fabrication, the device is fabricated through a simple UV-based soft imprint technique utilizing self-developed low loss polymer material. With a single-mode fiber, the coupling efficiency is around 12%. The 3 dB bandwidth centered at 1550 nm is 32 nm. The proposed structure would be very attractive in applications that require out-of-plane coupling or multiple routes signal processing.

6.7 References

[1] D. Taillaert, P. Bienstman, and R. Baets, “Compact efficient broadband grating coupler silicon-on-insulator waveguides,” Opt. Lett. 29, 2749-2851 (2004).

[2] G. Roelkens, D. Thourhout, and R.l Baets, "High efficiency Silicon-on-Insulator grating coupler based on a poly-Silicon overlay," Opt. Express 14, 11622-11630 (2006).

[3] R.Waldhäusl, B. Schnabel, P. Dannberg, E.-B. Kley, A. Bräuer and W. Karthe, “Efficient coupling into polymer waveguides by gratings,” Appl. Opt. 36, 9383–9390 (1997).

[4] Roman Bruck and Rainer Hainberger, "Efficient coupling of narrow beams into polyimide waveguides by means of grating couplers with high-index coating," Appl. Opt. 49, 1972-1978 (2010).

[5] M. E. Pollard, S. J. Pearce, R. Chen, S. Oo, and M. D. B. Charlton, “Polymer waveguide grating couplers for low-cost nanoimprinted integrated optics,” Proc. SPIE 8264, 826418-1~8 (2012).

[6] D. Taillaert, “Grating Couplers as Interface between Optical Fibres and Nanophotonic Waveguides”, PhD thesis, Ghent University, Ghent, Belgium (2004).

[7] CAMFR, http://camfr.sourceforge.net

[8] K. S. Yee, “Numerical solution of initial boundary value problems involving Maxwell's equations in isotropic media,” IEEE Trans. Antennas Propagat. 14, 302-307 (1966).

[9] J. Teng, Yan, H., Li, L., M. Zhao, Zhang, H., G. Morthier, “Simple ultraviolet-based soft-lithography process for fabrication of low-loss polymer polysiloxanes-based waveguides,” IET Optoelectron. 5, 265-269 (2011).

[10] T. Alasaarela, T. Saastamoinen, J. Hiltunen, A. Säynätjoki, A. Tervonen, P. Stenberg, M. Kuittinen, and S. Honkanen, “Atomic layer deposited titanium

dioxide and its application in resonant waveguide grating," Appl. Opt. 49, 4321-4325 (2010).

[11] D. Vermeulen, S. Selvaraja, P. Verheyen, G. Lepage, W. Bogaerts, P. Absil, D. Van Thourhout, G. Roelkens, "high-efficiency fiber-to-chip grating couplers realized using an advanced CMOS-compatible silicon-on-insulator platform," Opt. Express 18, 18278-18283 (2010)

Chapter 7 Athermal arrayed waveguide gratings in SOI

7.1 Introduction

In recent years, silicon photonics has received more and more attention as it represents another ideal platform for realizing compact and multifunctional photonic integrated circuits. One of its distinct advantages is that it provides extremely high refractive index contrast, which enables the densities of integration in the order of one million photonic devices in an area of one square centimeter. This is not possible in the polymer platform. Besides that, its compatibility with the industrial waferscale CMOS (Complementary Metal Oxide Semiconductor) fabrication technology is another advantage, allowing a drastic cost reduction of photonic devices without compromising performances. As a key passive photonic component, Arrayed Waveguide Gratings (AWGs) are of great use in all-optical networks as (de-)multiplexers and wavelength routers and as part of more complex photonic switches, sources or receivers. Although AWGs have conventionally been fabricated in low-index-contrast glass technology like silica, the desire for high-density photonic integration has led to an increasing interest in ultrasmall AWGs based on the silicon photonic wire waveguides with high index contrast [1-3].

However, the large thermo-optic (TO) coefficient of silicon ($dn/dT=1.8\times10^{-4}$ /°C) makes these SOI-based AWGs strongly temperature dependent, such that an external heater or cooler has to be employed to stabilize the chip temperature. These elements would not only take extra space but also consume additional power, counteracting the benefits brought by SOI technology. Athermal glass-based or InP-based AWGs have been demonstrated for several years, where the methods adopted for removing the temperature dependence include cutting silica AWGs at one of their slab waveguides into two pieces and then connecting them by a metal plate [4], inserting of a resin-filled groove into the arrayed waveguides or one slab waveguide [5-7] and so on [8, 9]. However, there has still not yet been an

experimental demonstration of athermal SOI AWGs so far. The methods mentioned above cannot simply be applied to SOI AWGs, mainly due to their extremely small size and layout complication. Furthermore, the optical path length differences need to be strictly controlled between several tens of arrayed waveguides in order to obtain good characteristics for SOI AWGs. The arrayed waveguides suffer from a high sensitivity to phase noise resulting from the high index contrast, which is even worse if modifications are to be made to them. That is the reason why the characteristics of SOI AWGs are still not comparable to those of their glass-based or InP-based counterparts. Other passive photonic components in SOI with relatively simpler structure, such as ring resonators or Mach-Zehnder interferometers, have been made athermal through a number of methods [10-14], but temperature independent AWGs have so far only been shown to be possible using simulations [15, 16]. The slot waveguides proposed in [15, 16] would also pose a challenge for fabrication.

In the first part of this chapter, the first experimental demonstration of athermal 1×8 AWGs in SOI wire technology with a channel spacing of 400 GHz will be presented. First, the working principle of AWGs will be introduced together with the thermal effect. Then several approaches will be overviewed to judge the possibility and feasibility of achieving athermalization for SOI AWGs, followed by the detailed theoretical analysis and design consideration. Two rounds of CMOS pilot line fabrication were carried out to obtain AWGs with good performance. Finally, measurement results together with necessary discussions will be given. In the second part of this chapter, an all-polymer waveguide structure will be proposed. The aim of this design is to eliminate the temperature induced noise within the biosensing system. The design considerations and simulation results will be given.

7.2 Working principle of AWG and its thermal effect

7.2.1 AWG's working principle

Fig. 7.1 shows the schematic picture of an AWG. It consists of several parts, which include input waveguides, input star-coupler, arrayed waveguides,

output star-coupler and output waveguides. The working principle is described below. After propagating through the input waveguide, light containing several different wavelengths enters into the input star-coupler and then diverges. When this diverging light spreads to the end of the input star-coupler, it will be coupled into the arrayed waveguides. Arrayed waveguides are a series of waveguides which are placed side-by-side to each other but with an adjacent length difference of ΔL. Due to this, the light coupled into each one of these arrayed waveguides will undergo a different phase shift. For one specific wavelength (central wavelength), the light beams reaching the output star-coupler from all of the arrayed waveguides have the same phase. The result of interference is that the light of this wavelength will focus at the center of the output circle plane (focal plane) of the output star-coupler. For wavelengths deviating from the central wavelength, the light beams reaching the output star-coupler from arrayed waveguides have different amounts of phase change because of the wavelength dependent propagation constant and length difference, causing the focal point of the light at this wavelength to move along the focal plane at the end of the output star-coupler. This principle is more clear if we describe it with the following equation:

$$n_s d sin\theta_0 + n_c \Delta L = m\lambda \tag{7.1}$$

where θ_0 is the diffraction angle, n_s and n_c are the effective refractive index of the star-coupler and the arrayed waveguide separately, *d* is the distance between the arrayed waveguides, ΔL is the length difference between two adjacent arrayed waveguides, m is an integer and λ is the wavelength [17]. It can be seen that there is a one-to-one relationship between λ and θ_0, where the “grating” meaning comes from. Such device can either be used to extract or combine different wavelengths, and thus is a very good in-plane integrated wavelength division (de)multiplexer.

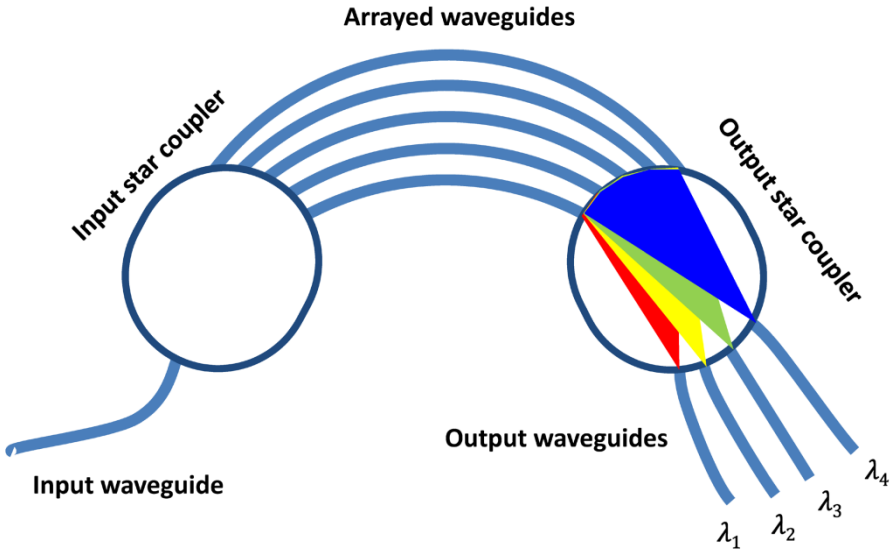

Fig. 7.1 Schematic picture of an arrayed waveguide grating.

7.2.2 AWG's thermal effect

Thermal effect means that the channel wavelengths of the AWG are not temperature independent. The fundamental reason is that the effective refractive index of the arrayed waveguides is not only wavelength dependent, but also temperature dependent, which can be expressed as $n_c = n_c(\lambda, T)$, T representing the temperature. The phase difference in the arrayed waveguides resulting from the temperature dependent propagation constant and length difference will cause a shift of the focal point at a specific wavelength along the focal plane at the end of the output star-coupler. The consequence is that the wavelengths entering into the output waveguides would change with temperature. By assuming $\theta_0 = 0$ and differentiating equation 7.1 with T on both sides, the temperature dependence of the channels' wavelengths of the AWG can be obtained as:

$$\frac{d\lambda_c}{dT} = \frac{\lambda_c}{n_c}\left(n_c\alpha + \frac{dn_c}{dT}\right) \tag{7.2}$$

here $\alpha = \frac{1}{\Delta L}\frac{d\Delta L}{dT}$ is the thermal expansion coefficient (TEC) of the substrate, and $\frac{dn_c}{dT}$ is the effective thermal optical coefficient. Considering the thermal

optical coefficient of Si is 1.8×10^{-4} /°C, normal SOI AWGs would exhibit a high temperature dependence, which is several tens of picometer per degree.

7.3 Approaches to realize athermalization of AWG

A lot of efforts have been paid to realize this aim. The materials with which the AWGs are fabricated range from Si, SiO_2 to InP, SiN_x and so on. So far, the most successful achievements were obtained with silica-based AWGs. In general, there are three main approaches, which include mechanical compensation with a metal, waveguide optical length compensation and athermal waveguide.

7.3.1 Mechanical compensation with metal

As mentioned before, the focal point of the light with wavelength λ at the focal plane of the output star-coupler would be different from that with wavelength $\lambda+\Delta\lambda$. The lateral position shift dx can be described as

$$dx = \frac{mn_g f}{n_s n_c d}\Delta\lambda \tag{7.3}$$

where $n_g = n_{eff} - \lambda \cdot \frac{dn_{eff}}{d\lambda}$ is the group refractive index of the arrayed waveguides, f is the focal length of the output star-coupler. The schematic picture is shown in Fig. 7.2. The linear relationship between dx and $\Delta\lambda$ implies that if we want to compensate the temperature dependence of wavelength λ, we can shift the output waveguide position by dx in correspondence with the wavelength change $\Delta\lambda$ caused by temperature variation.

This method was successfully used by Furukawa Electric company to achieve athermal AWG based on silica. As shown in Fig. 7.2, the AWG was cut at the star-coupler into two pieces and then connected by copper plate, whose length was carefully calculated. The small adjustment of the output waveguide position dx with temperature was realized by the thermal expansion or contraction of the copper plate, causing the small cut piece to slide.

7.3.2 Waveguide optical length compensation

How to remove the temperature dependence of the optical length difference between adjacent arrayed waveguides is the key for realizing athermalization of AWG. But this is impossible if arrayed waveguides are with only one certain material because $\frac{d(\Delta L \cdot n_c)}{dT} \neq 0$. However, if we divide the arrayed waveguides into two parts of which the materials are different, this can be made possible on the condition that they can cancel out each other, which is expressed as:

$$\frac{d(\Delta L \cdot n_c)}{dT} = \frac{d(\Delta L_1 \cdot n_{c1})}{dT} + \frac{d(\Delta L_2 \cdot n_{c2})}{dT} = 0 \tag{7.4}$$

This principle was realized by NTT photonics lab with a sophisticated triangular groove inserted structure, which is shown in Fig. 7.3. Silicon resin was chosen as the second material besides the silica. Due to the large disproportion of temperature dependent optical length change between silica and silicon resin, the inserted groove can be very short to have impact on the circuit layout.

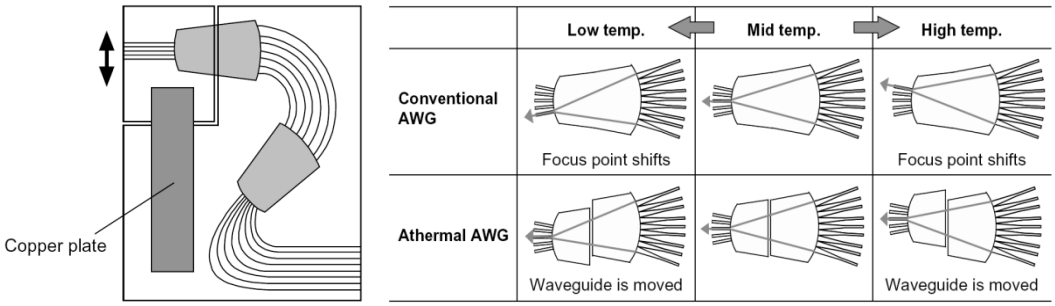

Fig. 7.2 The scheme of the athermal silica AWG realized with metal plate [4].

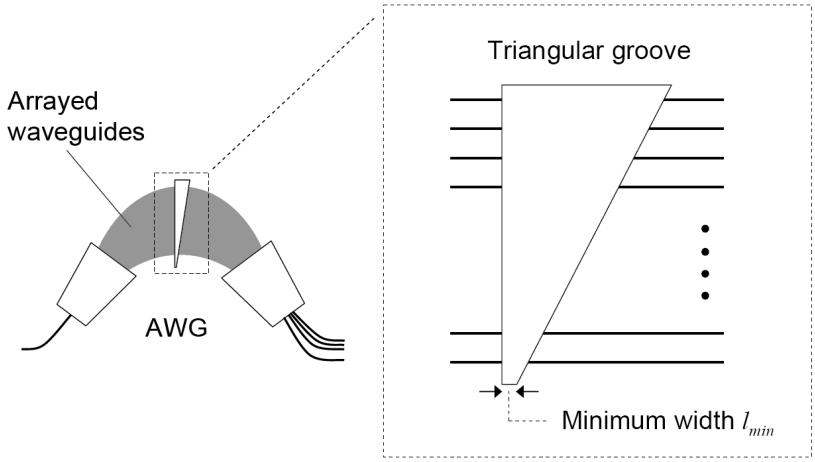

Fig. 7.3 The scheme of the athermal silica AWG realized with the resin filling groove [5].

7.3.3 Athermal waveguide method

It is straightforward that if each one of the arrayed waveguides itself is temperature independent, there would be no phase relationship changes between arrayed waveguides, in which case the AWG is athermal automatically. This principle can be expressed with the following two equal conditions:

$$n_c\alpha + \frac{dn_c}{dT} = 0 \leftrightarrow n_c\frac{d\Delta L}{dT} + \Delta L\frac{dn_c}{dT} = 0 \tag{7.5}$$

Obviously, the substrate's thermal expansion is used to cancel out the temperature dependent refractive index change. TiO_2-doped silica waveguides have such property and athermal AWG based on it functions well.

Although the first two approaches discussed above have some merits, either stringent fabrication control on critical part's dimension (e.g. length of metal plate or groove size) is required, or extra diffraction loss will be induced (silicon resin-filled groove). The third method is also material-specific. Moreover, they are very difficult to be implemented on SOI AWGs mainly because of their extremely small size and layout complication. At the first sight, the task of achieving athermal SOI AWGs is tough. But inspired by the successful demonstration of athermal microrings and M-Z interferometers in

our group, athermal waveguide approaches should have a chance to help us reach the goal.

7.4 Feasibility analysis of athermal SOI AWGs and CMOS fabrication

7.4.1 Athermal SOI waveguide

Since 2007, it become clear that athermal SOI components could be made by compensating the large positive TO coefficient of silicon by using a cladding with negative TO coefficient, where polymer can be an ideal option. For the case of silicon wire waveguides, an additional problem is that for the usual waveguide dimensions and TE-like polarization, most of the light is confined to the silicon and only a fraction can penetrate into the cladding with opposite TO coefficient. To arrive at athermal components, it is therefore typically necessary to reduce the dimensions of the silicon wire to allow more light to penetrate into the polymer. Besides that, the polymer functioning as cladding for compensation should meet the requirements of high negative TO coefficient and high thermal stability. By using equation 7.2, the $\frac{d\lambda_c}{dT}$ behaviour of the TE mode for different widths of the arrayed waveguides is calculated and the result is shown in Fig. 7.4a. The effective index of the SOI waveguide is calculated using FIMMWAVE (@ PhotonDesign Ltd). The height of 220 nm is in accordance with the value of the standard SOI wafer we use for fabrication in our group. The main parameters used are as follows: refractive index of Si, 3.4757; TO coefficient of Si, 1.8×10^{-4} /°C; refractive index of SiO_2, 1.444; TO coefficient of SiO_2, 1×10^{-5}/°C; α, 2.6×10^{-6} /°C [18]; Refractive index of polymer, 1.515; TO coefficient of polymer, -2.4×10^{-4} /°C [19]. It is noted that practical SOI waveguides fabricated in a CMOS foundry exhibit a trapezoidal shape and therefore waveguides with an 80 degree sidewall angle have been simulated and compared to ideal rectangular waveguides [20]. The width value of the bottom edge of the trapezoidal SOI waveguides is adopted for the simulation and the following experiments. From the simulation, both kinds of SOI waveguides evolve from under-compensated to over-compensated with

decreasing waveguide width. The ideal widths for these two kinds of arrayed SOI waveguides (and thus for AWGs) to be temperature independent lie around 305 nm and 340 nm for the rectangular and trapezoidal waveguides respectively. The optical modes at these two critical width values are shown in Fig. 7.4b and Fig. 7.4c. Because the trapezoidal waveguide model is closer to the shape of the fabricated waveguide, it gives better agreement with experiments than the rectangular waveguide model (See experimental results section).

7.4.2 Layout design considerations

In principle, reducing the dimensions of the silicon wire waveguides has a negative effect on the performance of the AWGs. Typically, the delay lines are broadened to reduce propagation loss and phase noise [3]. In our case, the phase noise in the waveguide arms would increase when they are narrowed, which would result in higher crosstalk between channels. The insertion loss would also increase with the narrowing of these waveguides. This should be taken into account when designing the layout. For this reason, polymer used in the thermal compensation is required to have high thermal-optical coefficient to prevent having to further reduce the waveguide dimensions. Fortunately, our developed material PSQ-LH meets this requirement. A waveguide width above 305 nm is adequate, which helps release the stress left for later fabrication. In addition, from the experiment, we found that the combination of a proper layout design and polymer overlay treatment can greatly eliminate the disadvantages brought by using narrowed arrayed waveguides.

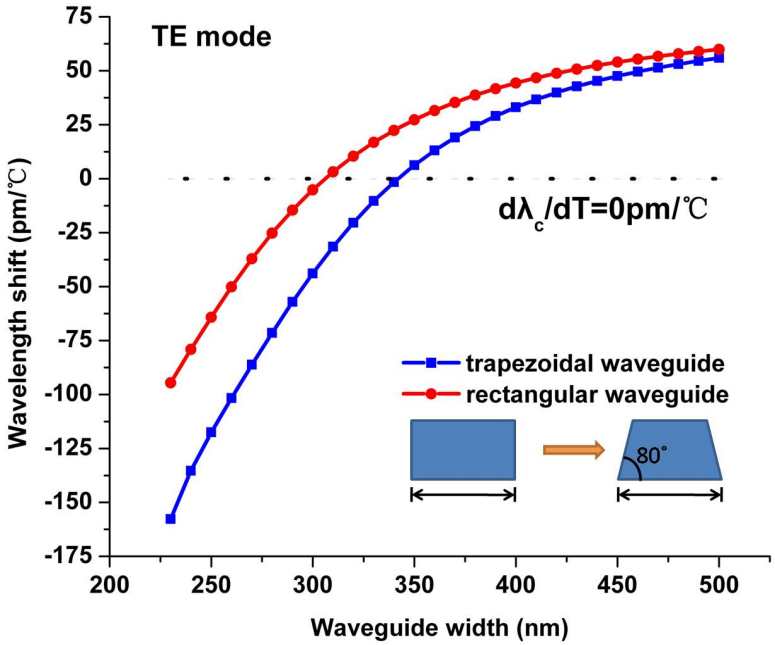

(a)

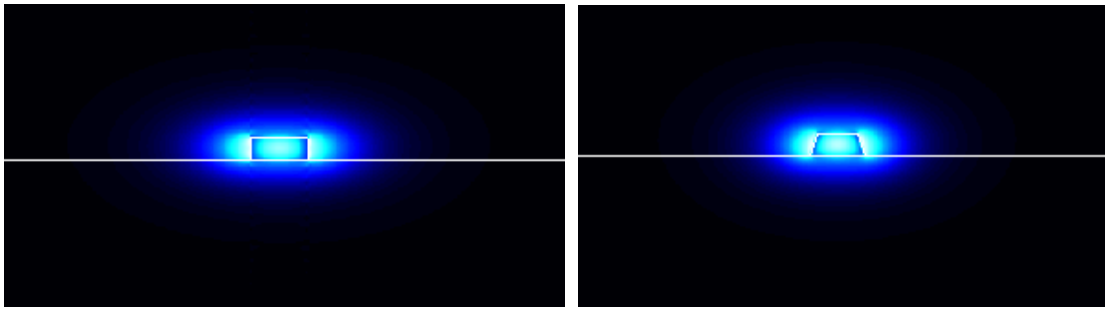

(b) (c)

Fig. 7.4 Simulation for the AWGs. (a) The temperature dependence of AWGs' central wavelength with waveguide widths for rectangular (red) and trapezoidal (blue) shape SOI waveguides. The optical modes at two critical width values for (b) rectangular and (c) trapezoidal shape SOI waveguides.

Our layout design is based on the normal waveguide dimensions (450 nm×220 nm) for the access waveguides to the star couplers and the bend waveguides in the AWGs. The narrowed waveguides are inserted for the straight waveguide arms only. The same rules for designing normal SOI AWGs are implemented on arranging these narrowed waveguides. The schematic picture is shown in Fig. 7.5. Compared with our early design [21],

such layout with straight arrayed waveguides structures folded by two 90˚ broad bend waveguides is much more flexible. It makes sharp bends and close spacing of the arms possible [1], thus the footprint of the devices is greatly reduced. In addition, compared to bended arrayed waveguides, the phase differences between the arrayed waveguides in this layout are much more controllable, which helps to reduce the crosstalk.

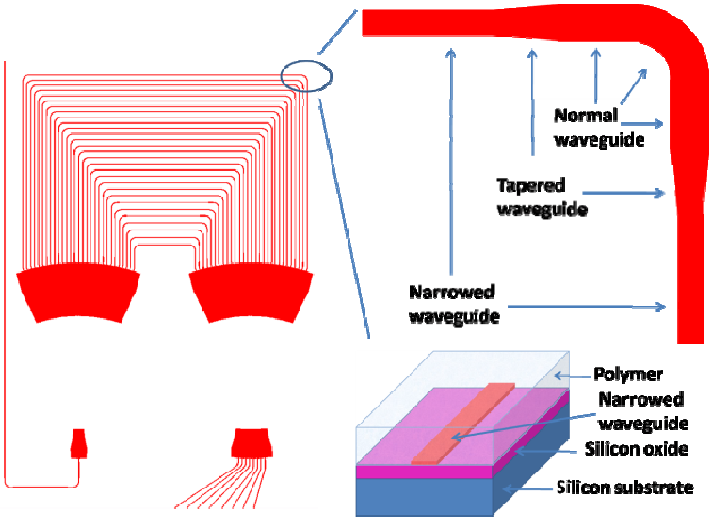

Fig. 7.5 Schematic picture of the proposed AWGs inserted with narrowed arrayed waveguides

7.4.3 CMOS fabrication

The standard SOI wafer with a silicon layer of 220 nm and an oxide layer of 2 μm is used for this work. The SOI waveguides are fabricated by 193 nm deep-UV lithography and Inductively Coupled Plasma - Reactive Ion Etching (ICP-RIE) in a standard CMOS fabrication process [22]. The CMOS compatible fabrication processes offer the advantages of high resolution as well as high throughput. By varying the exposure dose over the whole SOI wafer for the patterning of the waveguides, narrowed waveguides with width values ranging from 330 nm to 390 nm were obtained. The double-etch technique was adopted for the star couplers' area to reduce reflections [3].

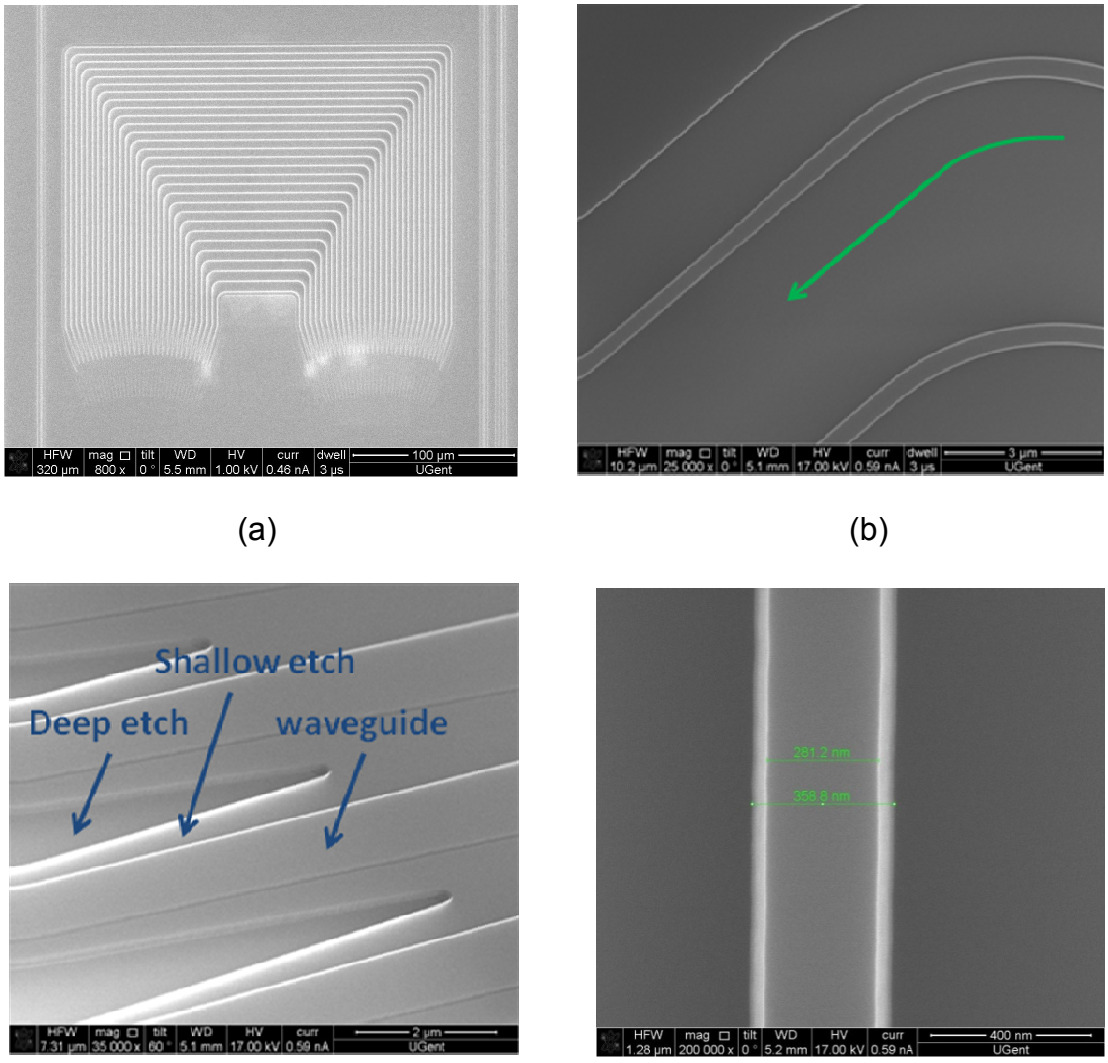

(a) (b)

(c) (d)

Fig. 7.6 The SEM pictures of the critical parts of the AWGs. (a) the whole image. (b) The transition from broad bend waveguide to narrowed arrayed waveguide through a linearly tapered waveguide. (c) The trapezoidal waveguide fabricated by CMOS technique. (d) The star couplers' area fabricated by double-etch technique.

Surface grating couplers, which selectively pick up the TE mode from the optical fiber, are also fabricated at the end of the input and output waveguides [23]. The SEM pictures of the critical parts of the AWGs mentioned above are shown in Fig. 7.6. After cleaning, Polymer PSQ-LH with a large TO coefficient

of -2.4×10^{-4} /˚C as well as low loss at 1550 nm and high thermal stability below 200 ˚C [19], is chosen as the cladding material and spin-coated on top of the fabricated SOI chips, with a layer thickness of around 2 μm.

7.5 Measurement results and discussion

7.5.1 Measurement setup

The measurement setup is shown in Fig. 7.7. For the AWG measurements, a super luminescent light emitting diode is used as the light source. The light coming out of it was launched into the input waveguide of the AWG with a single mode fiber through the fabricated surface grating couplers. Similarly, the transmitted light of each output channel is collected by another single mode fiber that is connected to an optical spectrum analyzer (Agilent 86140B) and then recorded. The minimal allowed resolution (0.06 nm) of the optical spectrum analyzer is used. In order to measure the AWG's spectra under different temperatures, the samples were mounted on a heating plate whose temperature could be controlled accurately.

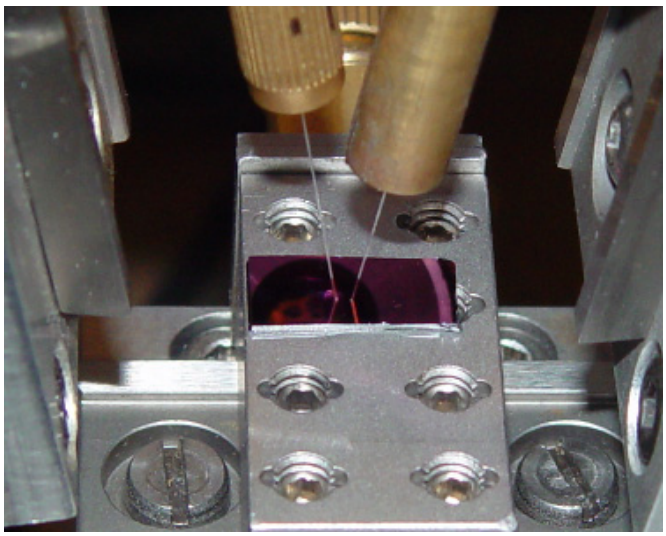

Fig. 7.7 The vertical setup for the measurement of AWG with surface grating coupler.

7.5.2 Measurement results

The temperature dependence of the peak wavelength for one of the central channels (channel 4) with different waveguide widths, before and after the polymer overlay, is shown in Fig. 7.8. In general, the SOI AWGs have an average wavelength temperature dependence above 65 pm/˚C before the polymer overlay (Fig. 7.8a). Although in theory these slope values of wavelength shift per degree should increase monotonically with waveguide width due to the higher optical confinement, they are too high and too close to each other to be resolved by our current measurement system, which is affected by the measurement environmental stability, the temperature control accuracy of the heating plate, the resolution of the optical spectrum analyzer, the adopted fitting method and so on. However, the high temperature dependence of the channel peak wavelength can be suppressed with polymer overlay. In Fig. 7.8b, the AWGs with different narrowed arrayed waveguide widths exhibit obviously different temperature dependent behaviour. The lowest temperature dependence was obtained for a waveguide width of 358.8 nm, where the temperature dependence of the filter peak wavelength was successfully reduced from above 65.4 pm/˚C to -1.5 pm/˚C, i.e. more than one order of magnitude lower than that of the normal SOI AWGs. This obtained width value also matches well with the previous simulation results based on a trapezoidal waveguide model, in which the optimal value is 340 nm. It also explains the reason why there was a gap between the 350 nm experimental value and the 306 nm simulated value in our previous demonstration of athermal SOI ring resonators [13].

The comparison of the full spectrum of the proposed AWG at 25 ˚C and 75 ˚C with and without polymer cladding is shown in Fig. 7.9. It can be seen that normal SOI AWG (without polymer cladding) have around 3.3 nm total spectrum shift with 50 ˚C temperature change, a shift which already exceeds the designed channel spacing of 400 GHz. In contrast, the total spectrum shift of the proposed AWG with polymer overlay is greatly reduced to only around 0.2 nm in this large temperature range, while keeping the good filtering property at the same time.

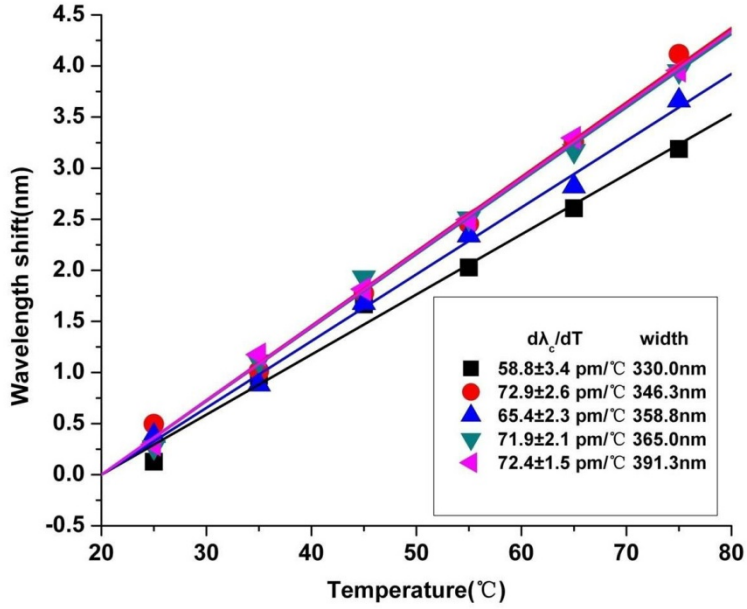

(a)

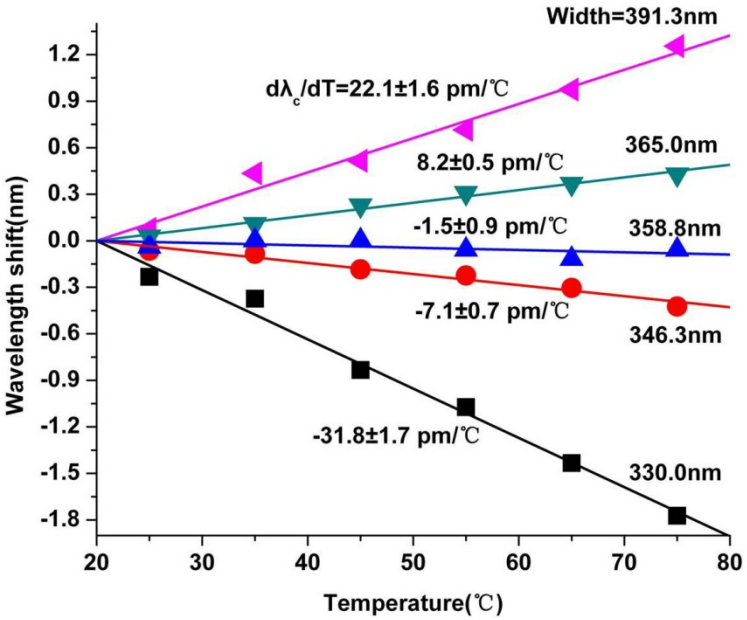

(b)

Fig. 7.8 Temperature dependence of the peak wavelength of channel 4 before polymer overlay (a) and after polymer overlay (b) for different waveguide widths.

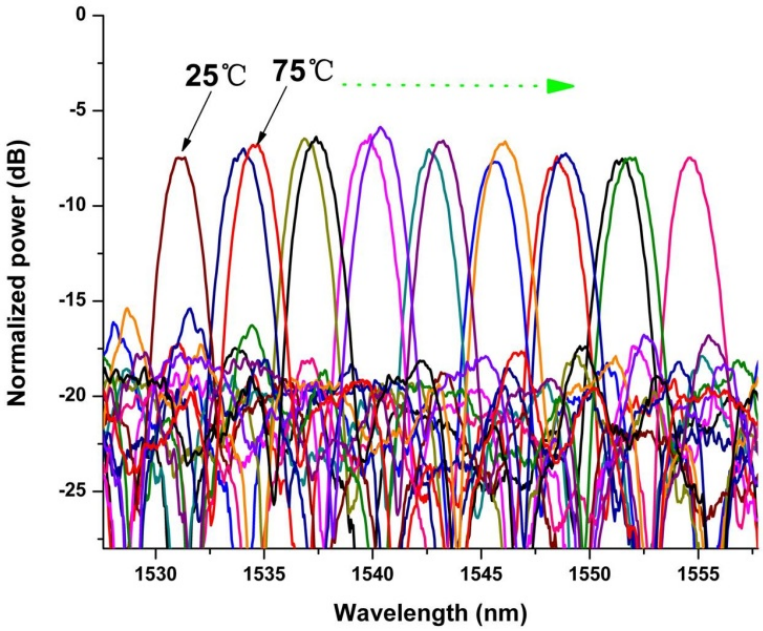

(a)

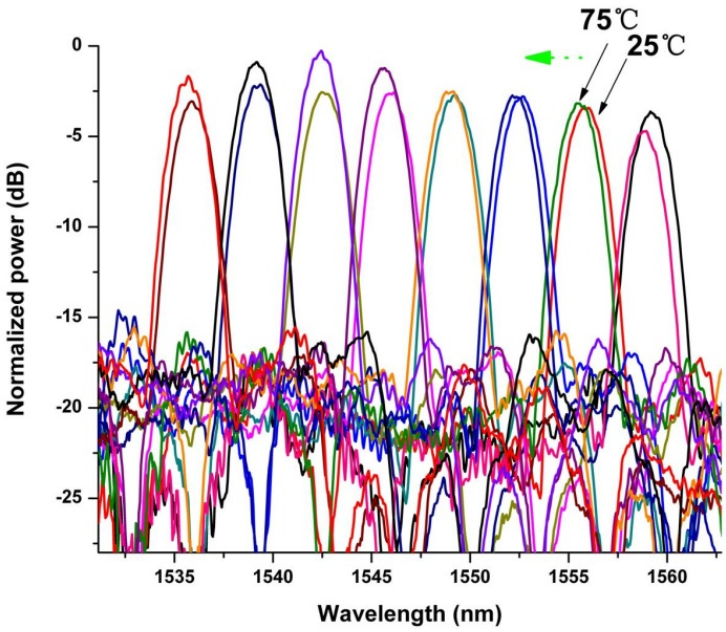

(b)

Fig. 7.9 The full spectrum of the proposed AWGs at 25˚C and 75˚C without (a) and with (b) polymer cladding.

It can also be seen from Fig. 7.9 that the AWG's characteristics are also improved significantly after the polymer overlay. For the central channel 5, the

insertion loss is reduced from 6.6 dB to 2.6 dB. The loss value of the AWG is extracted by normalizing the input to output port transmission of the AWG to that of a simple photonic wire. The reduced insertion loss can be explained by reduced scattering losses of the narrowed arrayed waveguides because the refractive index contrast is reduced by polymer deposition. The crosstalk is reduced from -11 dB to less than -15 dB, as a result of smaller phase errors. The nonuniformities between central and edge channels are around 0.7 dB. Some necessary discussions will be given below.

7.5.3 Discussion

As we know, stochastic nm-scaled width variation is inevitable during fabrication. The variation of the effective index of the arrayed waveguides with their width plays the most significant role in inducing phased errors, which can be expressed as $\frac{\partial n_c}{\partial w}$, where n_c is the effective index and w is the waveguide width. And it becomes worse with the decreasing of waveguide width [24]. This is illustrated in Fig. 7.10, As can be seen, In narrower waveguides, the effective index of the fundamental mode changes much more with the waveguide width, which is the same for waveguide either with air cladding or with polymer cladding. However, for 350 nm width, simulation of the waveguide mode shows that this value can be reduced by around 45% with polymer cladding, thus resulting in lower crosstalk, which also meets with the experimental results. The junction loss between the arrayed waveguides and the two star couplers might also be lower.

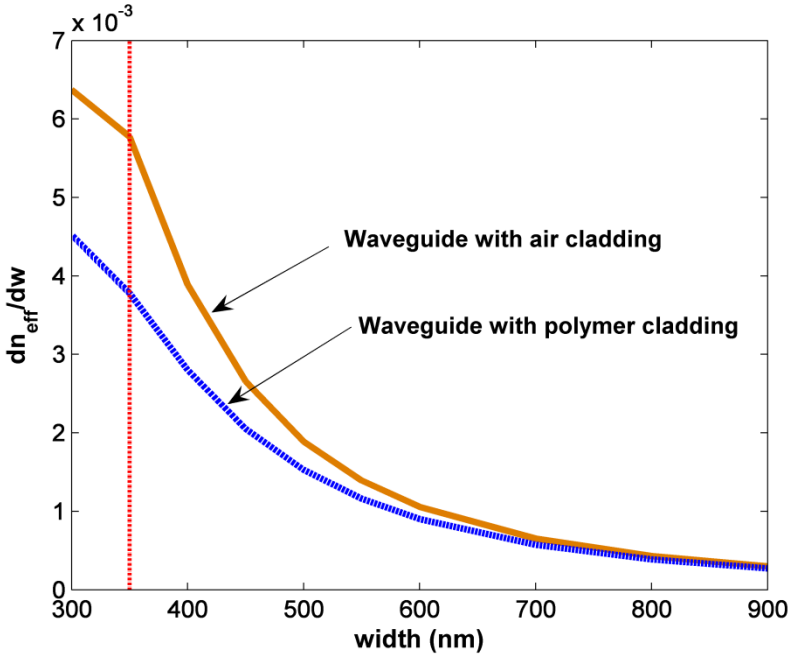

Fig. 7.10 The variation of the effective index of the arrayed waveguides with their width.

Although athermalization of silicon AWGs with characteristics at an average level has been successfully realized in this paper, the characteristics of the AWGs are still below those of silica AWGs or of optimized silicon AWGs and further improvements are still required and expected. This requires more advanced fabrication techniques which can significantly reduce the phase errors.

Silicon AWGs working in the TM mode regime can also be a solution. The TM mode of a silicon wire waveguide is less confined than the TE mode, which means that the waveguide can be compensated more easily by overlaying a polymer. Thus broad arrayed waveguides can be used instead of narrowed ones. Moreover, there is no discontinuity of the electrical field at the vertical sidewalls, where the waveguide roughness and width variation are unavoidable due to the fabrication. This would reduce the propagation loss and phase noise dramatically. Based on these arguments, the characteristics of athermal silicon AWGs are expected to be improved. However, special attention must be paid during the design to prevent mode conversions

between TM and TE modes and other challenges. So far, to our knowledge no working TM-mode AWG devices have been demonstrated. The other potential challenge is post-trimming of this athermal device. High intensity UV light trimming or electron beam induced compaction and strain trimming could be the possible solutions. [14, 25]

7.6 Design of all-polymer athermal ring resonator for optical biosensing

7.6.1 Important issue for biosensing: temperature

Considering the importance of the ring resonator for biosensing applications, a strategy to eliminate its temperature dependence is discussed in this section. So far, microring resonators fabricated in different kinds of materials can be seen, silicon and polymer are two typically important ones. Unfortunately, as mentioned before, both of these two materials have high thermo-optical coefficient (TOC). For example, the TOC of silicon is as high as 1.8×10^{-4} /°C, while that of polymer normally in the same scale with silicon but with negative value. The high material TOC makes these mcroring resonators very sensitive to their surrounding environmental temperature change. These temperature induced noises will be superimposed onto the sensing signals when performing biosensing, which lowers the signal to noise ratio (SNR) of the measuring system. This will be even more harmful when the sensing signals are small.

There are several approaches to circumvent this problem. The straightforward one is to incorporate a temperature stabilization subsystem to mitigate the temperature influence on the microring resonators, which is adopted in chapter 5. But this method requires extra space and energy. The other usual approach is introducing another reference microring placed close to the one performing the sensing function. With this method, the reference microring should be isolated well from the sensing analytes with a cladding layer and it must be guaranteed that both the reference and sensing ring have the same feeling towards the temperature change. All of these require extra

fabrication step and good dimensional control. It would be very ideal if the sensing ring resonator itself is temperature insensitive, which is found to be possible by the following analysis.

7.6.2 Removal of the temperature dependence of polymer ring resonator

The resonant condition of ring resonator can be expressed as:

$$n_{eff}L = m\lambda_R \tag{7.6}$$

where n_{eff} is the effective refractive index of the guided ring mode, L is the perimeter of the ring, λ_R is the resonant wavelength and $m = (1,2,3 \dots)$ is the resonant series. By differentiating the equation 7.6 with respect to temperature T, the temperature dependent wavelength shift slope of the ring can be derived as:

$$\frac{d\lambda_R}{dT} = \frac{\lambda_R}{n_{eff}}\left(\frac{dn_{eff}}{dT} + n_{eff}\alpha_{sub}\right) \tag{7.7}$$

where $\frac{dn_{eff}}{dT}$ is the TOC of waveguide, and $\alpha_{sub} = \frac{1}{L}\frac{dL}{dT}$ is the thermal expansion coefficient (TEC) of the substrate. This equation indicates that temperature dependent resonant wavelength can be removed by properly selecting the substrate and waveguide material to satisfy the following condition:

$$\frac{dn_{eff}}{dT} + n_{eff}\alpha_{sub} = 0 \tag{7.8}$$

In fact, the above discussion is the same as that for SOI AWGs in section 7.2.1 and 7.3.3. The reason is that both kinds of devices are working with the phase matching principle. Just for the convenience of discussion, they are rewritten here. Through transforming the equation 7.7, and integrating with respect to dT from T_0 to T, the resonant wavelength shift is obtained as:

$$\Delta\lambda_R = \lambda_R - \lambda_{R0} = \frac{\lambda_{R0}}{n_{eff0}}\left\{n_{eff}exp[\alpha_{sub}(T - T_0)] - n_{eff0}\right\} \tag{7.9}$$

where λ_{R0} and n_{eff0} are the resonant wavelength and the effective refractive index at T_0, respectively.

Because the silicon only has a TEC of 2.63×10^{-6} /°C, it can hardly exert influence on the total thermal effect of the device when the ring resonator is fabricated on silicon substrate. The negative effective TOC of polymer waveguide mode which is in the same level with its material TOC (~10^{-4} /°C) plays the dominant role. However, one advantage of fabricating the polymer waveguide devices using imprinting method is that the substrate is not only limited to silicon. Others such as PCB board, ceramic or polymer can also be used as substrate, which gives one more freedom for the device's design. Thus if the TEC of the substrate can meet the condition of $\alpha_{sub} = -\frac{1}{n_{eff}}\frac{dn_{eff}}{dT}$, which is derived from equation 7.8, the temperature dependence of the polymer ring resonator can be removed. Z. Zhang and N. Keil et al have studied thoroughly the TEC of different polymer material which is within the range of 0.5~3.9×10^{-4} /°C, depending on the component of polymer precursor. Thus athermalization of the polymer ring resonator has the hope to be realized with this all-polymer structure.

7.6.3 Simulation results

Simulation is carried out based on the structure of the ring resonator used for biosensing in chapter 5. The parameters are as follows: the refractive index of waveguide core is n_{core}=1.52 with TOC of -2.4×10^{-4} /°C. The refractive index of under cladding is $n_{cladding}$=1.45 with TOC of -2.2×10^{-4} /°C. The water upper cladding is with the index n_{water}=1.3105. The TOC of the water is -1.0×10^{-4} /°C. The waveguide width is W=2.3 μm. The waveguide height is H=2.1 μm with a slab layer which has thickness of S=0.2 μm; the radius of the bend waveguide is R=350 μm; the straight waveguide length of the coupling region is L=70 μm and the distance between the two straight waveguides is Gap=1.0 μm. Figure 7.11 shows the resonant wavelength shift versus temperature with the TEC of the substrate near 1.617 × 10^{-4} /°C. It can be seen that the temperature sensitivity of a ring resonator with an all-polymer structure is substantially suppressed compared with that using silicon substrate. For example, as the

TEC of the substrate is 1.6191×10^{-4} /˚C, the resonant wavelength shift is suppressed within the scope of -8 pm ~ 4 pm with a temperature ranging from 10 ˚C to 60 ˚C. In the vicinity of the normal temperature for us to perform biosensing, 20 ˚C for example, it is even smaller. The temperature independent condition is satisfied essentially. Moreover, it also shows that near this temperature, we have relatively large freedom on choosing the substrate with proper TEC. Besides that, we estimate the influence of a fabrication error on this temperature dependent value, which is shown in Figure 7.12. Near 20 ˚C, ±0.1 μm width variation of the waveguide almost has no influence on the temperature dependent wavelength shift, thus it means that our proposed structure has large tolerance on the fabrication error. Compared with the biosensing signal obtained in chapter 5, this temperature induced noise can be neglected. The above results indicate that we can perform biosensing with the fabricated device itself without resorting to other temperature stability subsystem or reference ring.

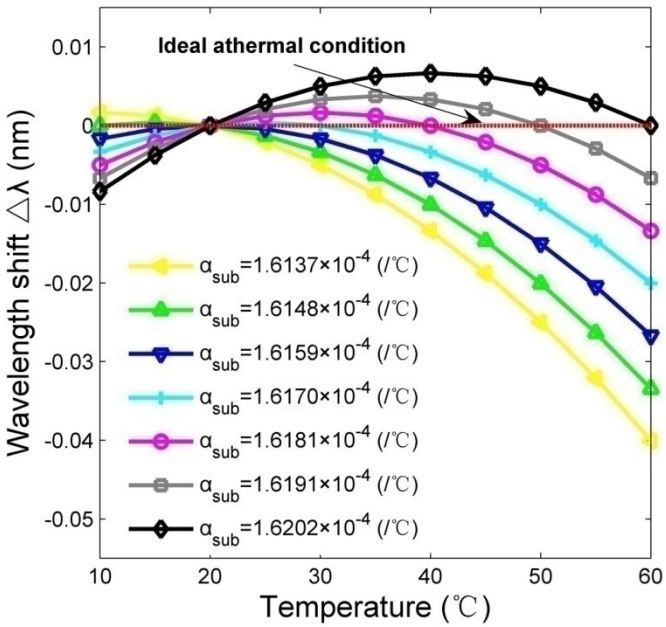

Fig. 7.11 The resonant wavelength shift versus temperature with TECs of the substrate.

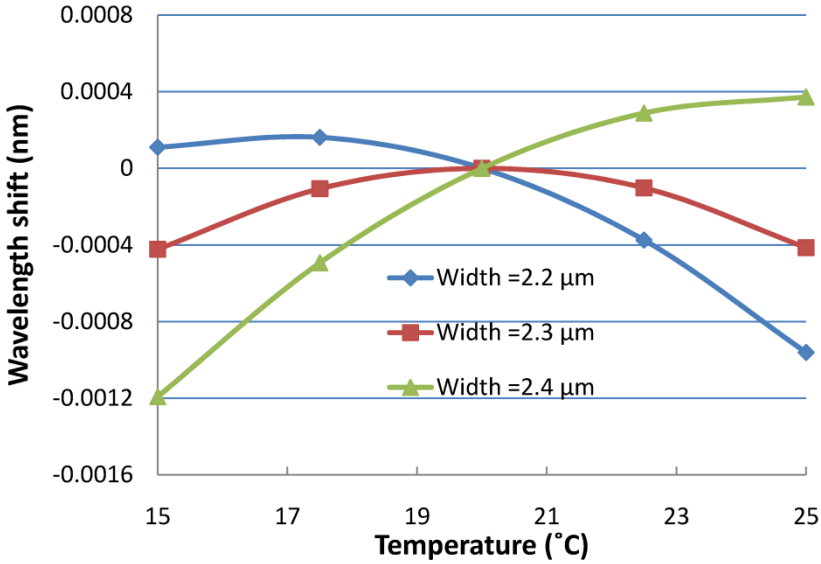

Fig. 7.12 The estimation of the influence of fabrication error on this temperature dependence.

7.7 **Conclusion**

In summary, a compact athermal SOI-based 1×8 AWG with 400 GHz channel spacing is demonstrated for the first time. The total size of the device is 350×250 μm^2. By insertion of the straight narrowed arrayed waveguides and overlay polymer layer, the wavelength temperature dependence of the AWG is successfully reduced to only -1.5 pm/˚C. Good characteristics of the AWG such as low insertion loss and crosstalk are also obtained at the same time. So far, several key optical components, which include MZI, microring resonator and AWG, have been made athermal by us. These optical components will play an important role in future high-level electric-photonic integration systems and the optical telecommunication networks. Besides that, an all-polymer structure was proposed for the label-free biosensor with ring resonator structure, which, if realized, can essentially remove the temperature induced noise during the biosensing measurement.

7.8 References

[1] W. Bogaerts, P. Dumon, D. Van Thourhout, D. Taillaert, P. Jaenen, J. Wouters, S. Beckx, V. Wiaux, and R. Baets, “Compact wavelength-selective functions in silicon-on-insulator photonic wires,” IEEE J. Sel. Top. Quantum Electron. 12, 1394–1401 (2006).

[2] P. Dumon,W. Bogaerts, D. Van Thourhout, D. Taillaert, and R. Baets, “Compact wavelength router based on a silicon-oninsulator arrayed waveguide grating pigtailed to a fiber array,” Opt. Express 14, 664–669 (2006).

[3] W. Bogaerts, S. Selvaraja, P. Dumon, J. Brouckaert, K. De Vos, D. Van Thourhout, and R. Baets, “Silicon-on-insulator spectral filters fabricated with CMOS technology,” IEEE J. Sel. Top. Quantum Electron. 16, 33–44 (2010).

[4] T. Saito, K. Nara, and K. Tanaka, “Temperature-Insensitive (Athermal) AWG Modules,” Furukawa Rev. 24, 29-33 (2003).

[5] S. Kamei, "Recent progress on athermal AWG wavelength multiplexer," Proceedings of SPIE 6014, 60140H1-60140H-9 (2005).

[6] S. Kamei, T. Shibata, and Y. Inoue, “Compensation for second-order temperature dependence in athermal arrayedwaveguide grating realizing wide temperature range operation,” Photon. Technol. Lett. 21, 1695–1697 (2009).

[7] K. Maru and Y. Abe, “Low-loss, flat-passband and athermal arrayed-waveguide grating multi/demultiplexer,” Opt. Express 15, 18351–18356 (2007).

[8] K. Eun-Seok, K. Woo-Soo, K. Duk-Jun, and B. Byeong-Soo, “Reducing the thermal dependence of silica-based arrayed waveguide grating using inorganic-organic hybrid materials,” IEEE Photon. Technol. Lett. 16, 2625–2627 (2004).

[9] H. Tanobe, Y. Kondo, Y. Kadota, K. Okamoto, and Y. Yoshikuni, “ Temperature insensitive arrayed waveguide gratings on InP substrates,” IEEE Photon. Technol. Lett. 10, 235–237 (1998).

[10] Y. Kokubun, S. Yoneda, and S. Matsuura, “Temperatureindependent optical filter at 1.55 mm wavelength using a silica-based athermal waveguide,” Electron. Lett. 34, 367–369 (1998).

[11] J.-M. Lee, D.-J. Kim, H. Ahn, S.-H. Park, and G. Kim, “Temperature dependence of silicon nanophotonic ring resonator with a polymeric overlayer,” J. Lightwave Technol. 25, 2236–2243 (2007).

[12] J.-M. Lee, D.-J. Kim, G.-H. Kim, O.-K. Kwon, K.-J. Kim, and G. Kim, “Controlling temperature dependence of silicon waveguide using slot structure,” Opt. Express 16, 1645–1652 (2008).

[13] J. Teng, P. Dumon,W. Bogaerts, H. Zhang, X. Jian, X. Han, M. Zhao, G. Morthier, and R. Baets, “Athermal silicon-oninsulator ring resonators by overlaying a polymer cladding on narrowed waveguides,” Opt. Express 17, 14627–14633 (2009).

[14] L. Zhou, K. Okamoto, and S. J. B. Yoo, “Athermalizing and trimming of slotted silicon microring resonators with UVsensitive PMMA upper-cladding,” Photon. Technol. Lett. 21, 1175–1177 (2009).

[15] X. Wang, S. Xiao,W. Zheng, F.Wang, Y. Li, Y. Hao, X. Jiang, M. Wang, and J. Yang, “Athermal silicon arrayed waveguide grating with polymer-filled slot structure,” Opt. Commun. 282, 2841–2844 (2009).

[16] H. Huang, S.-T. Ho, D. Huang, Y. Tu, and W. Liu, “Design of temperature-independent arrayed waveguide gratings based on the combination of multiple types of waveguide,” Appl. Opt. 49, 3025–3034 (2010).

[17] M. K. Smit and C. van Dam, “PHASAR-based WDM-devices: principles, design and applications, “IEEE J. Sel. Top. Quantum Electron. 2, 236–250 (1996).

[18] Y. Kokubun, S. Yoneda, and H. Tanaka, “Temperature independent narrowband optical filter at 1.31 μm wavelength by an athermal waveguide,” Electron. Lett. 32, 1998–2000 (1996).

[19] H. B. Zhang, J. Wang, L. Li, Y. Song, M. Zhao, X. Jian, and J. Wouters, “Synthesis of liquid polysilisiquioxane resins and properties of cured films,” Thin Solid Films 517, 857–862 (2008).

[20] S. Selvaraja,W. Bogaerts, and D. Van Thourhout, “Loss reduction in silicon nanophotonic waveguide micro-bends through etch profile improvement,” Opt. Commun. 284, 2141–2144 (2011).

[21] P. Dumon, W. Bogaerts, D. Van Thourhout, D. Taillaert, V. Wiaux, S. Beckx, J. Wouters, and R. Baets, “Wavelength selective components in SOI photonic wires fabricated with deep UV lithography,” in Proceedings of the First IEEE International Conference on Group IV Photonics (IEEE, 2004), pp. 28–30.

[22] S. Selvaraja, P. Jaenen, W. Bogaerts, P. Dumon, D. Van Thourhout, and R. Baets, “Fabrication of photonic wire and crystal circuits in silicon-on-insulator using 193 nm optical lithography,” J. Lightwave Technol. 27, 4076–4083 (2009).

[23] D. Vermeulen, S. Selvaraja, P. Verheyen, G. Lepage, W. Bogaerts, P. Absil, D. Van Thourhout, and G. Roelkens, “ High-efficiency fiber-to-chip grating couplers realized using an advanced CMOS-compatible silicon-on-insulator platform,” Opt. Express 18, 18278–18283 (2010).

[24] P. Dumon,W. Bogaerts, D. Van Thourhout, G. Morthier, and R. Baets, “Compact arrayed waveguide grating devices in siliconon-insulator,” Proceedings of the IEEE/LEOS Symposium Benelux Chapter (IEEE, 2005), pp. 105–108.

[25] J. Schrauwen, D. Van Thourhout, and R. Baets, “Trimming of silicon ring resonator by electron beam induced compaction and strain,” Opt. Express 16, 3738–3743 (2008).

Chapter 8 Conclusion and perspective

8.1 Conclusion

The aim of this PhD was to develop an ideal platform, on which the different kinds of integrated photonic devices with high performance can be fabricated in a fast and efficient way with the cheap polymer material. Based on that, several applications on optical communication and optical sensing are found for these devices obtained from this platform.

As the foundation for the work, an innovative polysiloxane polymer material named PSQ-Ls was developed. The material exhibits good optical properties (e.g. low optical loss, low birefringence, high thermo-optical coefficient and so on) and thermal stability (e.g. high degradation temperature). Being UV curable and solvent-free are unique features for this material. These material characterizations indicate that PSQ-Ls can be a good candidate for the fabrication of polymer waveguides and devices.

Different fabrication processes were explored to find an appropriate way to process the developed polymer PSQ-Ls into waveguides and devices. Conventional lithography and dry etching method was considered to be unsuitable because of the complicated fabrication process. A simple UV-based soft imprint technique compatible with polymer PSQ-Ls was developed. Critical issues such as roughness and residual layer were solved and discussed in detail. Different kinds of polymer-based optical devices, which include straight waveguide, splitter, microring notch filter, racetrack microring resonator and MZI-based tunable ring resonator, were fabricated in this fast and efficient way. Their good performances were shown by lots of measurements and characterization, some of which are highly desired for our subsequent applications, for example, the low loss of optical waveguide, the high extinction ratio of the notch filter, the high Q value of the microring resonator, and so on.

Several applications on optical communication and optical sensing were achieved with these fabricated devices. In chapter 4, optical single sideband

(OSSB) filtering response was realized by using the microring notch filter with high extinction ratio as a narrowband microwave photonic filters. By this, the chromatic dispersion induced fading effect was suppressed effectively, which allows the microwave modulated optical signal to be transmitted over long distance fiber link and the microwave signal can still be received with high quality. Optical label-free biosensing was realized with the polymer microring resonator with high Q value. The sensing mechanism, interrogation methods and the design consideration for this kind of device were discussed. Special attention was paid to the performance of the microring working in aqueous environment. A simple but efficient surface functionalizaiton protocol was developed for the polymer microring resonator, of which the detailed characterizations and comparisons were presented in chapter 5. Both bulk sensing and surface sensing were realized with the solution delivering capability provided by the fluidic channel, which was assembled on the chip of polymer microring resonators. For bulk sensing, sensitivity of around 50nm/RIU was achieved with NaCl solution. For surface sensing, the resonant wavelength shift of 230 pm was observed when the binding of the targeted analyte and the bioreceptors we immobilized previously happened on the surface of the polymer microring resonator. The aim of this work is to incorporate the advantages of the polymer material itself, the imprint technology and surface functionalization protocol together, to develop a low-cost, disposable polymer label-free biosensor. In chapter 6, we investigated a new coupling mechanism for polymer waveguide, surface coupling. Although silicon surface grating couplers with different kinds of structures have been intensively studied in the past few years, very limited work was done on polymer. The main challenge lies in the low refractive index of the polymer itself. In order to circumvent this problem, we proposed a structure, in which a thin layer of Si_3N_4 with high refractive index was embedded between the waveguide core and under cladding. By doing this, the coupling between the polymer waveguide and the single-mode fiber was demonstrated for the first time, with a coupling efficiency of around 12%. Compared with the edge coupling route usually adopted for the polymer waveguide, the surface

coupling regime is more flexible with relaxed alignment tolerance, which would be of great use for the further development of multiplexed biosensing with polymer-based photonic devices. Finally, the temperature problem was considered and discussed in chapter 7. Special attention was paid to realize athermalization for one of the most important WDM components, arrayed waveguide grating (AWG). Taking advantage of proper design, state-of-the-art CMOS fabrication technique and high thermo-optical coefficient of the PSQ-Ls polymer, the temperature dependence of the AWG was reduced to only -1.5 pm/˚C, while maintaining the good filtering property of the device. So far, several key optical components, which include MZI, microring resonator and AWG, have been made athermal. These optical components will play an important role in future high-level electric-photonic integration system. Besides that, an all-polymer structure was proposed for the biosensor with ring resonator structure, which, if realized, can essentially remove the temperature induced noise during the biosensing measurement.

8.2 **Perspective**

Some ideas have risen during the research, together with some unsolved problems, which will be left for the future work. And they will be discussed in this section.

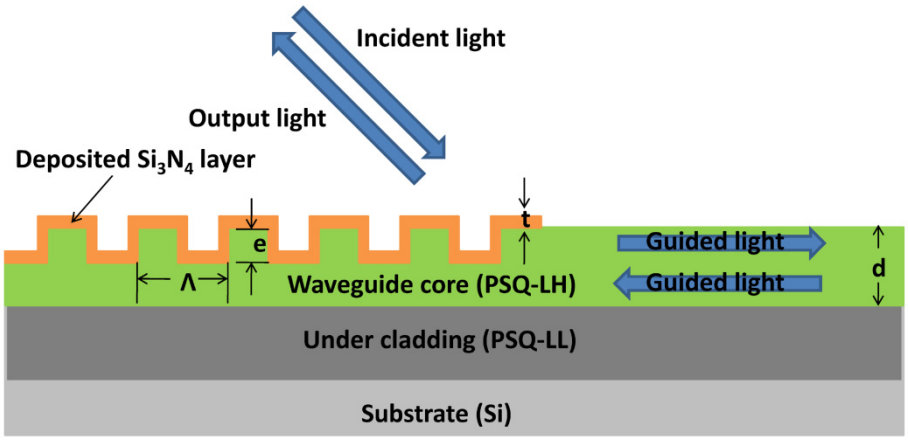

Fig. 8.1 The proposed grating structure for the ridge shaped polymer waveguide.

Although the label-free biosensing has been shown to be promising with the benefits from material, fabrication, surface functionalization, the capability of multiplexed sensing has not been shown. One important reason is so far we still haven't managed to integrate the polymer surface grating coupler with the core element, polymer ring resonator, as currently they are with different waveguide structures. The port waveguides for the polymer ring resonator is with ridge shaped structure, while polymer grating coupler is based on inverted-rib structure. In order to integrate them, we proposed an alternative structure different from the one given in Fig. 6.1 of section 6.3 in chapter 6, which is shown in Fig. 8.1 below. The most critical point to realize this structure here is the fabrication of the master mold, but with two different depth values for the waveguide and for the grating. This cannot be realized with the master mold fabrication technique introduced in section 3.3.1 of chapter 3, where lithography and developing can only achieve one depth needed for the waveguides. To realize that, we need to resort to some advanced fabrication technique, FIB (focused-ion-beam) for example, to create grating structures on the SU-8 master mold after the patterns for the polymer waveguides are defined. FIB itself is a slow fabrication process but with high accuracy. But once the master mold is obtained, large quantities, or let's say, arrays of polymer ring resonators with grating couplers on their port waveguides can be patterned with one step imprinting. Thus the advantages of the developed imprint technology are not compromised. However, the master mold fabrication technique using FIB needs to be well optimized, on which lots of efforts were paid. Near the end of this thesis, some inspiring results were obtained, with the results shown in Fig. 8.2. Based on that, the further integration of the polymer surface grating coupler with polymer microring resonator can be promising.

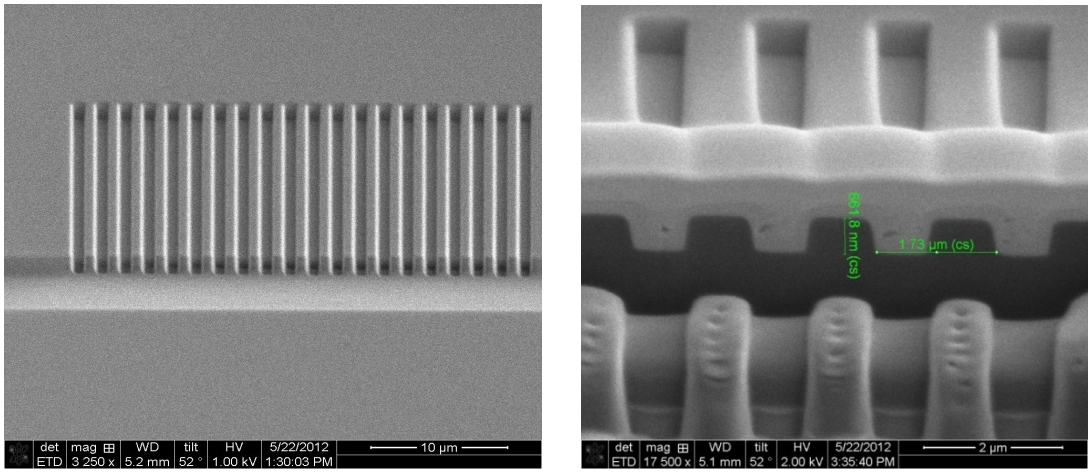

Fig. 8.2 The grating structure fabricated by FIB on the SU-8 master mold.

Polymer-based photonic biosensor has the potential to work with shorter wavelength. Currently the biosensing in this work is still performed with the infrared wavelength around 1550 nm. The sources and the detectors are typically quite expensive. A switch toward a shorter wavelength (*e.g.* visible wavelength) would enable the use of cheap and ubiquitous red lasers, CCD chips and barcode readers, thus greatly reduce the cost of the whole system. Moreover, since the water absorption of the light in visible wavelength is considerably lower than that in the infrared, the performance of the polymer microring resonator in the aqueous environment has the hope to be further improved. During the research, the polymer PSQ-Ls was found to be quite transparent at the shorter wavelength. The absorption measurement is shown in Fig. 8.3. And we have successfully fabricated the polymer microring resonator with the UV-based soft imprint process developed in chatper 3. The dimensions of the PSQ-Ls waveguide have been scaled down, allowing single mode operation of the device in the visible wavelength. The SEM pictures are shown in Fig. 8.4. Efforts were paid for the measurements of these devices, but no further results are available so far. One possible problem can be the low coupling efficiency between the ring and straight waveguide, as currently our gap resolution is limited to 0.8 µm by the contact lithography during the master mold fabrication, which is too large for the visible wavelength. But this

can be overcome because now the master mold fabrication technique has become very mature.

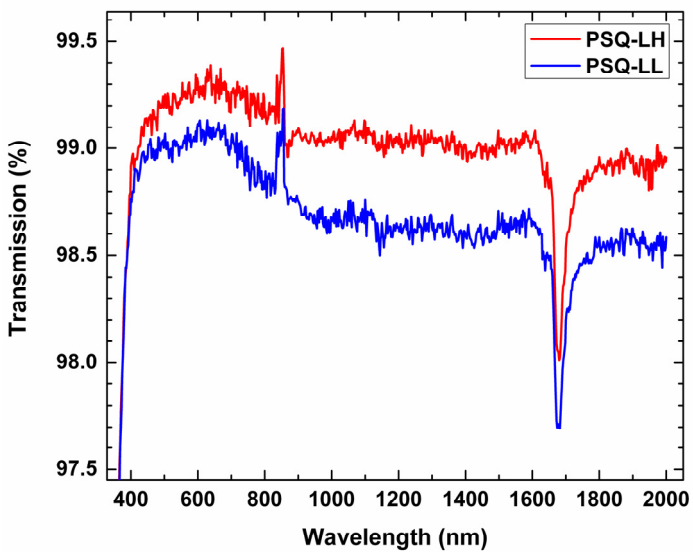

Fig. 8.3 The transmission spectrum of the polymer PSQ-Ls from wavelength of 400nm to 2000nm.

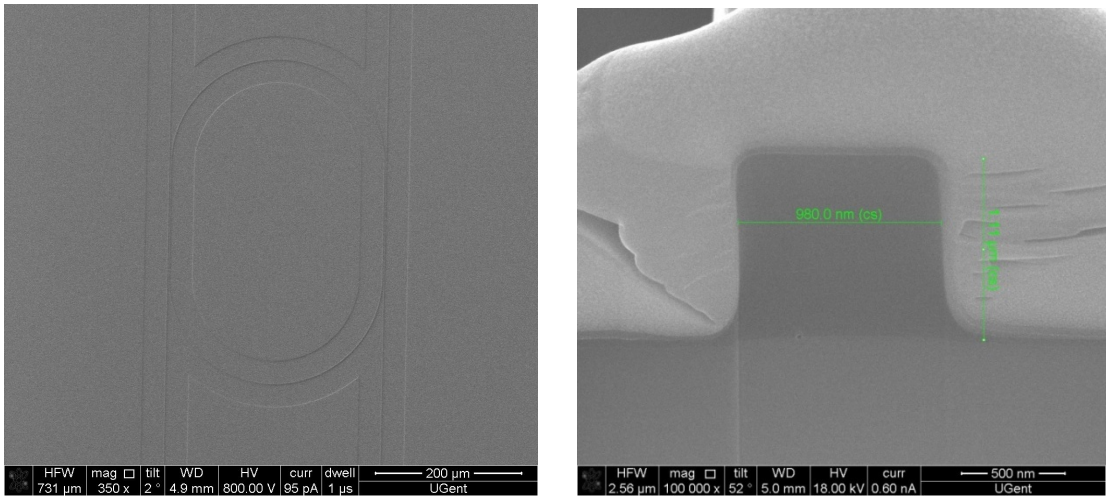

(a) (b)

Fig. 8.4 SEM pictures of the polymer microring resonator with single mold waveguide dimensions for the visible wavelength. (a) Top view. (b) Cross section.

A temperature insensitive biosensor is of high value without doubt. Although the all-polymer structure has been proposed in chapter 7, fabrication of such device is not straightforward. The curing temperature is still too high, thus the polymer substrate must withstand the temperature above 200 ˚C. It is desired if the curing temperature can be reduced in the future. The thermal expansion coefficient of the polymer substrate and the PSQ-Ls must mach to prevent the cracking of the film during curing because of the built up internal stress. Probably silicon will still be used as the hard substrate to support the polymer substrate during the processing. Thus a solution must be found to separate the polymer substrate and the silicon.

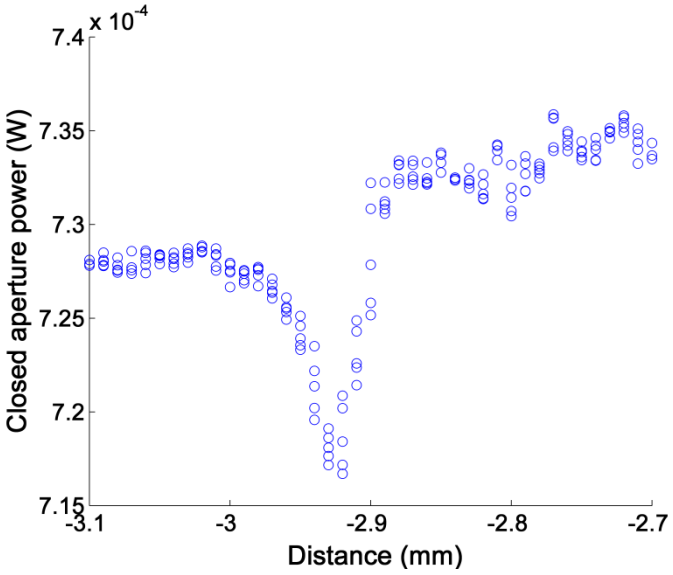

Fig. 8.5 Z-scan measurement of the dye doped polymer film.

Since the imprinting technique developed within this thesis is a non-chemical reaction method, essentially the optical waveguides are fabricated simply by molding the polymer. The whole process would not cause the changing of the properties of the polymer. Thus it is attractive to use this method to fabricate optical waveguide in nonlinear polymers. Within this thesis, we also attempted to dope the passive polymer waveguide core material with some dyes. Preliminary nonlinear phenomenon was observed with the slab waveguide films by the Z-scan method, which is shown in

Fig. 8.5. But further research is needed, especially for the dye doped polymer material, to make it mature for actual applications.

Appendix A List of figures

Appendix B List of tables